UNIVERSITY OF THE
WITWATERSRAND,
JOHANNESBURG

Modification of boron nitride nanostructures induced by medium energy ion irradiation

This is a thesis that has been submitted to meet the requirements

for obtaining a Doctor of Philosophy degree

in the field of Material Science Physics,

within the Faculty of Science.

Authored

by

Lehlohonolo Innocent Lisema

Supervisor: Prof. Trevor Derry

Co-supervisor: Dr Morgan Madhuku

TABLE OF CONTENTS

1 INTRODUCTION 1

1.1 Motivation 1

1.2 Problem Statement 2

1.3 Objectives 3

1.4 Outline 4

2 THEORETICAL ASPECTS OF BNNTS IN NANOTECHNOLOGY 7

2.1 Nanotubes 7

2.2 Boron nitride 9

2.2.1 Boron nitride Nanotubes (BNNTs) 10

2.2.2 Synthesis methods of Boron nitride nanotubes 13

3 ION IMPLANTATION IN BORON NITRIDE 18

3.1 Ion Implantation 18

3.2 Projected range (R_p) 19

3.2.1 Electronic stopping 21

3.2.2 Nuclear stopping 22

3.3 Radiation damage 25

3.3.1 Radiation damage in Boron nitride 26

3.4 Ion Channelling effect 28

4 EXPERIMENTAL METHODS 29

4.1 Sample preparation 29

4.2 Chemical Vapour Deposition (CVD) 30

4.3 Ion Implantation 32

4.3.1 Principles of ion implantation 33

4.4 Characterization Methods 39

4.4.1 Raman spectroscopy principles and instrumentation 39

4.4.2 X-ray diffraction (XRD) and Grazing incidence X-ray diffraction (GIXRD) 46
4.4.3 Scanning electron microscopy (SEM) 51
5 RESULTS 54
5.1 Simulation of stopping and range of ions in matter (SRIM)-2013 54
5.2 Scanning electron microscopy (SEM) 56
5.2.1 Samples prepared at 900°C 56
5.2.2 Samples prepared at 1000°C 57
5.2.3 Samples prepared at 1100°C 58
5.2.4 Samples prepared at 1200°C 59
5.3 Grazing incidence XRD characterization 60
5.4 Raman characterization 64
5.4.1 Raman spectra of BN nanocomposites 65
5.4.2 Raman micrographs 68
6 DISCUSSION 72
6.1 Growth mechanism of boron nitride nanostructures 72
6.2 Scanning electron microscopy (SEM) 74
6.2.1 Synthesized BNNTs Morphology 74
6.2.2 Synthesized BNNTs diameter 74
6.3 Grazing incidence XRD 76
6.3.1 Calculated lattice constants 76
6.3.2 Refined structural details 81
6.3.3 X-ray attenuation and X-ray depth 82
6.4 Raman derived calculated Average crystallite domain size 87
6.4.1 Raman Spectroscopy micrograph images 89
6.5 Summary 91
7 CONCLUSION 93
8 APPENDIX A 95
8.1 Williamson-Hall method 95
8.2 Simulated XRD patterns 96
8.2.1 Cubic BN F-43m COD 9008834 96

8.2.2 Hexagonal BN P63.mmc COD 9008997 97
8.3 Polycrystalline hexagonal boron nitride Raman spectrum 100
9 APPENDIX B 101
9.1 Conferences 101
9.2 Publications 102
10 REFERENCES 103

DECLARATION OF AUTHORSHIP

- This study was done solely while I was enrolled at this University as a research degree candidate.
- This thesis has never before been presented to this University or any other school for the purpose of obtaining a degree or qualification.
- All references to the published works of others have been explicitly acknowledged.
- All quotes from other authors' works have been properly cited, except for those that have been explicitly identified as quotations.
- I have recognized all significant sources of assistance that I have received.
- In cases where the thesis is based on collaborative work, I have clearly indicated the contributions made by myself and others involved in the project.

Signed: 

Date: 29 August 2023

ABSTRACT

This research focused on using Chemical Vapour Deposition (CVD) to synthesize boron nitride nanostructures, particularly nanotubes, and selectively introducing defects into them through ion implantation. Boron ion implantations were carried out at ambient temperature at 150 keV energy and fluences $1x10^{14}$ and $5x10^{14}$ ions/cm^2. The synthesized samples were analyzed using scanning electron microscopy (SEM), Raman spectroscopy, and Grazing incidence X-ray diffraction (GIXRD). Ion implantation was found to introduce defects into the surface of the samples, resulting in increased stress levels and a higher local density that favoured more crystallized nanostructures. SEM images showed clear evidence of BN nanostructures and boron nitride nanotubes (BNNTs), with the latter appearing as long, thin structures with diameters ranging from ~30-90nm.

After ion implantation, the Raman spectra of samples implanted with ion fluence 5×10^{14} ions/cm^2 at 1000^{o}C, show an amorphous h-BN peak, and a narrower, intense E_{2g} vibrational mode of h-BN is observed around 1366 cm^{-1} for samples synthesized at 1100^{o}C and 1200^{o}C. Raman analysis did not show any E_{2g} mode of vibration of h-BN for all samples at implanted with ion fluence 1×10^{14} ions/cm^2. The samples synthesized at 900 ^{o}C had no active 1366 cm^{-1} Raman peak present.

Grazing incidence X-ray diffraction (GIXRD) spectra revealed a prominent peak between 54 and 56 ° 2θ, corresponding to the (004) h-BN reflection, which was used to determine the average ***a*** and ***c*** lattice parameters 0.249 ± 0.0002 nm and 0.662 ± 0.001 nm, respectively, yielding an interplanar distance of 0.166 ± 0.0001 nm representing the stacking direction of the BN layers. The majority of the samples had broad peaks, indicative of a nanocrystalline material. The only exception was the sample grown at 1200 °C, which was found to have a Scherrer crystallite size >100 nm. In contrast, the rest of the samples had an average size of 3.5 ± 0.3nm.

The average crystalline domain size values confirmed that after ion implantation, the phonon lifetime would be longer due to a large domain size, indicating that the BN nanostructures were more crystallized. The fluence of $5x10^{14}$ ions/cm^2 showed to be the optimal growth condition for BNNTs. Overall, BNNTs and BN nanostructures

were effectively synthesized at 900°C, 1000°C, 1100°C, and 1200°C CVD temperatures, and insights into the influence of ion implantation on the composition as well as properties of BN nanostructures are presented.

The most noteworthy finding of the experiment was the substantial increase in the size of the Raman derived crystallite domains in the 1100°C and 1200°C samples following ion implantation with boron ions at a fluence of $5x10^{14}$ ions/cm^2.

To myself

*… A **PhD candidate is like an electron** in that they **cannot** remain in an **excited state**!*

*"And we know that **all things work together for good** to them that love God, to them who are the called according to his purpose."-Romans 8:28*

ACKNOWLEDGEMENTS

Prof. Trevor Derry and Dr. Morgan Madhuku, my supervisors, merit my sincere gratitude for their unflinching support, guidance, consistent motivation, and priceless insights that enabled me to complete this thesis. I would also like to appreciate Prof. Rudolph Erasmus for his assistance with Raman spectroscopic analysis, as well as Mr. Adam Shnier, Prof. David Billing, and Prof. Daniel Wamwangi for their contributions to the Grazing Incidence X-ray Diffraction (GIXRD) measurements. I am grateful to Prof. Neil Coville and Dr. Victor Mashindi for sharing their expertise and providing valuable insights on the chemical vapour deposition (CVD) experiment, and I would like to express my appreciation to Mr. Tony Miller for his assistance with the ion implantations.

Assistance was provided by iThemba LABS (Gauteng) through the utilization of the Varian-Extrion 200-20A2F Ion implanter.

Financial support for this research was provided by the S.A. Department of Science and Technology - National Research Foundation Centre of Excellence in Strong Materials, as well as the School of Physics at the University of the Witwatersrand.

I would like to express my gratitude to Dr. Nhluvoko, Liteboho, Boitumelo, Malefetsane, Sibusiso, and my siblings, *ausi* Maggie, *ausi* Palesa, and Kwantla, for their support. Finally, and most importantly, I express my gratitude for the support of my beloved partner, *khayalami!* Zwakele Mthiya, I want to honour you for being such an inspiration despite the challenges.

Above all, I give God thanks.

NOMENCLATURE

- **BN-boron nitride**
- ***c-BN*-cubic boron nitride**
- ***h-BN*-hexagonal boron nitride**
- **CNTs-Carbon nanotubes**
- **BNNTs-Boron nitride nanotubes**
- **MWNT-Multi-wall nanotube**
- **SWNT-Single-wall nanotube**
- **LDA-local density-functional approximation**
- ***dE*-energy lost by an ion matter**
- ***dx*-distance travelled by an ion**
- ***S*-stopping power (subscripts *t, n* & *e* denote total, nuclear & electronic, respectively)**
- ***C*(*x*)-density of implants/implanted species**
- ***D*-dose, fluence, or the number of ions per unit area**
- R_p**-mean projected range**
- ΔR_p**-average deviation in** R_p
- E_d **-displacement energy**
- ***b* -impact parameters**
- **distribution (**v_b**) of the impact parameters**
- **Magnesium oxide (MgO)**
- **iron (ii) oxide (**Fe_2O_3**)**
- **Ammonium hydroxide (**NH_4OH**)**
- **Boric Oxide (BO)**
- **hydroxide (**OH^-**)**
- **ammonium (NH4+)**
- **lithium chloride (LiCl),**
- **boron trifluoride (**BF_3**)**
- **magnetic field (*B*)**
- **radius of curvature (*R*)**

- **charge (*q*)**
- **extraction electrode potential (V_{ext})**
- **acceleration electrode potential (V_{acc})**
- **electric field (*E*)**
- ***E_{inc}* - energy of the incident light**
- **Incoming photon of frequency *w_i***
- **Emitted or absorbed a phonon of frequency *w_{ph}***
- **Scattered a photon of frequency *w_s***
- **$h -$ placks constant**
- ***q_i*-the wave vectors of the incoming photon**
- ***q_s*-the wave vectors of the incoming photon**
- ***q_{ph}*-the wave vectors of the emitted or absorbed phonon**
- **ϑ_i-incident angle**
- **ϑ_c-critical angle**
- **The damage density/vacancy concentration *C(x)***
- **mean number of vacancies/ion/Å (*C_p*)**
- ***D*-fluence**
- **σ-is the surface energy**
- **α-is the supersaturation ratio (p/p_0)**
- **p-is the vapour pressure of the growth species**
- **p_0-is the equilibrium vapour pressure of the condensed phase**
- **k -is the Boltzman constant**
- **T-temperature (ºC)**
- **P_N-The probability of nucleation**
- ***a* -lattice parameter**
- ***c*-lattice parameter**
- **ρ-density**
- ***A*, the atomic mass**
- **N_A, Avogadro's constant**
- **V_c, volume of a unit cell**
- **$D_{crystal}$- crystallite size**
- **$\beta_{\frac{1}{2}}$-FWHM**

- **λ-wavelength**
- **ϵ-Strain**
- **σ_s- Stress**
- **Attenuation length, X_L**
- **X-ray depth, X_d**
- **The laser penetration depth (P)**
- **absorption coefficient (α_a)**
- **μ_m-mass absorption coefficient**
- **SEM - scanning electron microscope**
- **GIXRD - grazing incidence X-ray diffraction**
- **CVD - Chemical Vapour Deposition**

LIST OF FIGURES

Figure 2.1: (a) Single-wall nanotube (MWNT), (b) Multi-wall nanotube (SWNT) [11]. 8
Figure 2.2: Structural types of nanotubes [9][10]. 8
Figure 2.3: (a) h-BN structure, (b) c-BN structure [2]. 9
Figure 2.4: Structures of: (a) Graphite. (b) Boron nitride [15] 10
Figure 2.5: LDA (local density-functional approximation) band structure of BN sheet compared with that of a single graphite sheet in the hexagonal Brillouin zone. The Fermi level and band gap are indicated, respectively, by the dot-dashed line and the shaded area [6]. 11
Figure 3.1: Diagram illustrates the projected range, which indicates the position where the majority of ions stop. 21
Figure 3.2: Variation of ion stopping power with ion energy, separately indicating the nuclear and electronic contributions to the total stopping power. 24
Figure 3.3: Graph generated by the SRIM model shows the relationship between the depth of penetration and the number of vacancies per ion and unit length (measured in Å) for various ions, namely boron, lithium, helium, and neon ions, which were implanted into h-BN at 150 keV. 27
Figure 3.4: Relationship between ion penetration depth and the atomic masses of different ions. 27
Figure 3.5: Schematic representation of the channelling effect in a monocrystalline material [48]. 28
Figure 4.1: Flow diagram, illustrating the preparation of samples. 29
Figure 4.2: Schematic illustrating the CVD experimental procedure. 30
Figure 4.3: CVD Experimental set-up using Carbolite CTF Tube Furnace (Serial No. 21-103513). 31
Figure 4.4: Si-substrates after deposition of BNNTs. 31
Figure 4.5: Varian-Extrion 200-20A2F ion implanter. 32
Figure 4.6: Schematic diagram of the 200-20A2F ion implantation system [49]. ..33
Figure 4.7: Schematic drawing of Freeman-type ion source [50]. 34
Figure 4.8: Schematic diagram of Mass Analyzer. 35

Figure 4.9: X-Y electrostatic scan system with dc deflection to avoid neutral atoms [54]. 37
Figure 4.10: Energy level diagrams demonstrating how an excited atom undergoes different-energy photon release due to: (a) Rayleigh scattering, (b) Stokes Raman scattering, and (c) anti-Stokes Raman scattering. [59]. 41
Figure 4.11: The Jobin-Yvon T64000 spectrometer design (provided by HORIBA Jobin Yvon Ltd., UK), which was used in this study. 43
Figure 4.12: Instrumentation for the Jobin-Yvon T64000 Raman analyser spectrometer. 44
Figure 4.13: D8 discover ADVANCE Bruker X-ray Diffractometer. 46
Figure 4.14: Schematic diagram of a diffractometer system. 48
Figure 4.15: Diagram representation of Bragg's law [63]. 48
Figure 4.16: Schematic of diagram X-ray tube [65]. 49
Figure 4.17: ZEISS Sigma 300 VP. 51
Figure 4.18: Schematic diagram of a scanning electron microscope [68].....53
Figure 5.1: The graph generated by the SRIM model shows the relationship between the depth of penetration and the number of vacancies per ion and unit length (measured in Å) for boron ions at 150 keV. 55
Figure 5.2: SEM image of synthesized boron nitride cauliflower-like nanocomposites, captured using secondary electron mode. 56
Figure 5.3: SEM micrograph of synthesized boron nitride nanocomposites at 1000ºC with the diameter of selected particles/composites/features indicated (diameter measurements indicated on image). 57
Figure 5.4: SEM image of boron nitride nanotubes (BNNTs) synthesized at 1100ºC, captured using secondary electron mode. 58
Figure 5.5: SEM images of sample synthesized at 1200 ºC, showing BN nanostructures of different shapes at different magnification, including many nanotubes, captured using secondary electron mode. The diameters of representative nanotubes are indicated in red. 59
Figure 5.6: Grazing incidence XRD spectra of h-BN cauliflower like nanocomposites grown at 900 ºC. 60
Figure 5.7: Grazing XRD spectra of h-BN nanostructures grown at 1000 ºC. 61
Figure 5.8: Grazing incidence XRD Spectra of BN nanotubes grown at 1100 ºC. .62
Figure 5.9: GIXRD spectra of CVD samples prepared at 1200 ºC. 63
Figure 5.10: Raman Spectra of CVD prepared h-BN nanostructures at 1000 ºC. ..65

Figure 5.11: Raman Spectra of CVD prepared BNNTs at 1100 ºC, the two plots per ion fluence come from the two measured spots on the sample. 66
Figure 5.12: Raman Spectra of BN nanostructures prepared at 1200ºC. 67
Figure 5.13: Raman spectroscopy micrograph of Si-Substrate. 68
Figure 5.14: Raman spectroscopy micrograph of samples prepared at 900°C CVD temperature (a) without ion implantation, (b) Sample implanted with 1×1014 ions/cm2 (c) Sample implanted with 5×1014 ions/cm2. 69
Figure 5.15: Raman spectroscopy micrograph of samples prepared at 1000 °C CVD temperature, (a) As-grown sample, (b) Sample implanted with 1×1014 ions/cm2, (c) &(d) Sample implanted with 5×1014 ions/cm2. 70
Figure 5.16: Raman spectroscopy micrograph of samples prepared at 1100 °C CVD temperature, (a) & (b) As-grown samples, (c)&(d) Sample implanted with 5×1014 ions/cm2, (e) Sample implanted with 1×1014 ions/cm2.....70
Figure 5.17: Raman spectroscopy micrograph of samples prepared at 1200 C CVD temperature, (a) As-grown samples, (b) Sample implanted with 1×1014 ions/ cm2. (c) Sample implanted with 5×1014 ions/cm2. 71
Figure 6.1: The stress-strain graph of ion implanted BN nanostructures.....80
Figure 6.2: A cross section visual illustrating the shape of X-ray attenuation length and X-ray depth.....84
Figure 6.3: The relationship of the BN nanostructures density and attenuation length as a function of the depth of X-rays.....86
Figure 6.4: Graph of the Raman peak derived average crystallite domain size as a function of FWHM.....88
Figure 8.1: Simulated XRD pattern of Cubic BN.....96
Figure 8.2: Simulated XRD pattern of h-BN.....97
Figure 8.3: Raman Spectra of bulk h-BN. 100

LIST OF TABLES

Table 2.1: Comparison of properties of BNNTS and CNTs.....12
Table 2.2: Various methods used for synthesizing BNNTs [38].....17
Table 5.1: Displays the determined concentration of damage density in the material. 55
Table 6.1: Determined lattice parameters and density of As-grown samples. 78
Table 6.2: Determined lattice parameters and density of samples implanted with 1e14 ions/cm^2 ion fluence.....78
Table 6.3: Determined lattice parameters and density of samples implanted with 5e14 ions/cm^2 ion fluence.....78
Table 6.4: The calculated strain and stress values. 80
Table 6.5: The X-ray attenuation length is determined from density values that are obtained experimentally.....83
Table 6.6: Calculated X-ray depth values.....85
Table 6.7: Raman derived Calculated Average crystallite domain size. 89
Table 8.1: Crystallographic Data for Cubic Boron nitride (CBN) Obtained from X-ray Diffraction (XRD) Analysis, COD 9008834. 97
Table 8.2: Crystallographic Data for hexagonal Boron nitride (h-BN) Obtained from X-ray Diffraction (XRD) Analysis, COD 9008997.....98
Table 8.3: TOPAS results (GIXRD 1 deg, full footprint) 98
Table 8.4:TOPAS results (GIXRD 1 deg, 3mm footprint).....99

CHAPTER 1

1 INTRODUCTION

1.1 MOTIVATION

One of the most significant categories in nanotechnology and nanostructures are nanotubes which are effectively rolled-up monolayer films. It is well known that structural, electrical, and optical properties of thin films are strongly correlated with their nanostructure, morphology, film thickness and impurities [1]. Irradiation of materials with energetic particles, such as ions or electrons, usually spoils their chemical or physical properties. However, recent studies [2] on irradiation of various nanostructures have shown that ion and electron bombardment can produce useful effects on nanomaterials and that ion or electron beams can be harnessed to change their morphology and modify their magnetic, electrical, and mechanical properties. The work done by Aradi et al [3], [4] and previous research [5], of ion implantation effects on bulk hexagonal BN (h-BN) have shown h-BN to cubic-BN (c-BN) transformation at the ion implanted subsurface. However, irradiation studies on bulk h-BN and c-BN systems can only provide very little knowledge available about defect production in BN nanostructures (nanotubes, nanoribbons, fullerenes, and nanosheets) under irradiation.

The atomic structure of boron nitride nanostructures is comparable to that of carbon nanostructures, the C atoms in graphene-like planes are replaced by alternating B and N atoms with almost the same in-plane lattice constants and interlayer distances. With a band gap of about 5.5 eV and no tube chirality or shape, BNNTs are always insulators in contrast to CNTs, which can be metallic or semiconducting [2]. Moreover, layered BN structures are thermally and chemically more stable, although their mechanical properties are comparable to those of carbon nanotubes. Surprisingly, regardless of their innovative significance and the need to know the

behaviour of these materials under irradiation conditions, the effects of ion irradiation on BN nanostructures have been hardly explored, despite extensive studies in nanostructured carbon materials. Therefore, ion beam irradiation studies in BN nano-systems have become necessary. The addition of extra atoms to the structure will also be considered.

1.2 PROBLEM STATEMENT

The investigation into advanced nanomaterials has opened up new pathways for technological progress in various sectors. Boron nitride nanotubes (BNNTs) and carbon nanotubes (CNTs) are two such materials that have garnered considerable attention due to their unique structural and functional traits. Both possessing a tubular structure, BNNTs and CNTs display remarkable mechanical strength, excellent thermal conductivity, and noteworthy electronic properties [6]. However, while extensive research has been conducted on the properties of CNTs, BNNTs remain comparatively less explored, particularly in the context of effects induced by radiation.

In previous research has unveiled the intriguing potential of harnessing positive ions to enhance the properties of bulk hexagonal boron nitride, revealing the ability to change its structural properties [5]. Despite these insights, the irradiation-induced responses of BNNTs have largely remained uncharted territory. This critical knowledge gap forms the backdrop for the current study, which seeks to address a series of fundamental questions to understand the behaviour and potential of BNNTs within radiation-hostile environments. The central objectives of this study can be summarized as follows:

Behaviour of BNNTs under Radiation: Under radiation hostile environments, how do BNNTs react? Do they retain their exceptional inherent properties, or do effects triggered by radiation alter their structural, thermal, and mechanical traits? Understanding the stability and integrity of BNNTs in such conditions is important, as it can influence their potential applications in diverse high-radiation settings, including space exploration, nuclear reactors, and medical imaging.

Ion beam interaction and enhancement of properties: This research aims to show the effects of ion beam exposure on BNNTs by building on the idea of modified bulk hexagonal boron nitride properties using positive ions. Can the already exceptional qualities of BNNTs be improved by ion irradiation? Is it possible to create BNNTs with certain properties using carefully regulated ion bombardment? These issues are at the core of the study since they may uncover novel development approaches for nanomaterials with exceptional capabilities.

1.3 OBJECTIVES

The study will use the Chemical Vapor Deposition (CVD) method for the synthesis of BNNTs, enabling precise control over their growth and morphology. This method ensures the production of high-quality nanotubes with desired attributes. Furthermore, ion implantation was harnessed as a means of intentionally modifying BNNT structures at the atomic level, thereby offering the potential to enhance their existing qualities or introduce novel properties that could be advantageous for specific applications.

This work aims to not only investigate BNNTs in radiation-hostile environments but also to unravel the intricate interplay between ion implantation and the resulting modifications in nanotube properties. By elucidating the innovative significance of BNNTs in both realms, this research holds the potential to contribute to advancements in materials science, nanotechnology, and diverse industries reliant on reliable and resilient materials in challenging environments.

1.4 OUTLINE

There are six chapters in this thesis.

Chapter 1: Introduction

This chapter discusses the significance of nanotubes in nanotechnology and the potential effects of ion irradiation on boron nitride nanostructures, specifically boron nitride nanotubes (BNNTs). The chapter highlights the similarities between the atomic structure of BNNTs and carbon nanotubes (CNTs) and the intrinsic properties they share. However, unlike CNTs, BNNTs are insulators with a band gap of ~5.5 eV, and their behaviour under ion irradiation conditions has not been extensively studied. The chapter presents the problem statement and research objectives of this study, which aim to explore how BNNTs behave in radiation-hostile environments and whether their characteristics can be improved after exposure to an ion beam. The study also highlights the innovative significance of BNNTs, and their potential uses in various applications.

Chapter 2: Theoretical aspects of BNNTs in nanotechnology

This chapter provides an introduction to the theoretical aspects of Boron nitride Nanotubes (BNNTs) in the field of nanotechnology. It begins by discussing nanotubes and their classification into single-wall (SWNTs) and multi-wall (MWNTs) structures based on their tubular structure. The discussion then moves on to Boron nitride (BN), a Group III-V semiconductor that has two stable crystal structures, hexagonal (*h*-BN) and cubic (*c*-BN). The chapter explains how BN is similar to carbon in distinct ways, producing soft sp^2 graphite-like and hard sp^3 diamond-like bonded phases. The focus of the chapter is on BNNTs which were discovered in 1994. BNNTs are always a wideband gap semiconductor, and their properties are compared with those of Carbon Nanotubes (CNTs). The chapter provides a detailed explanation of the similarities and differences between graphite and *h*-BN, which are the parental structures of carbon nanotubes and boron nitride

nanotubes. Finally, the chapter compares the electrical, thermal, and mechanical properties of BNNTs and CNTs.

Chapter 3: Ion implantation in Boron nitride

This chapter explains the technique of ion implantation, which is used to introduce impurities into solid materials by accelerating appropriate ions onto the material at energies between electron volts and mega-electron volts in a consistent and dependable manner. The ion-solid interactions that occur during implantation cause the implanted ions to lose energy and change course due to collision with the electrons or nuclei of the solid, producing defects in the slowing-down process. The characteristics of the implanted material are altered as a result of the interaction of the atoms and produced point defects in the material. The chapter also explains the projected range ($\boldsymbol{R_p}$) of implanted ions, which essentially indicates the depth at which most ions stop, and how the ion concentration can be modelled as approximately Gaussian around that depth with a standard deviation ($\Delta\boldsymbol{R_p}$). The chapter discusses electronic stopping, and the nuclear stopping power. Finally, the chapter provides equations for calculating the fluence, as well as information about using the SRIM® computer simulation program to estimate ion and recoil atom distribution and collision details.

Chapter 4: Experimental methods

This chapter provides an overview of the experimental and characterization tools used in this work, including the materials used, their preparation, the experiments done on them, and the characterization techniques used. The chapter specifically focuses on two experimental techniques: Chemical Vapour Deposition (CVD) and Ion Implantation. It describes the set-up and procedure of each technique and provides relevant figures to illustrate them. Additionally outlined are the fundamentals of ion implantation and the components of an ion implantation system. Overall, the chapter provides a detailed account of the experimental methods used in the study.

Chapter 5: Results and Discussion

In this chapter, a study on the synthesis and analysis of boron nitride nanostructures using chemical vapour deposition (CVD) and ion implantation experimental methods is presented. The study investigates the effects of different synthesis temperatures and ion implantation fluences on the structure and properties of the boron nitride nanostructures. The chapter describes the experimental procedures used to synthesize the samples, as well as the characterization techniques used to analyse their structure and properties, such as scanning electron microscopy (SEM), Raman spectroscopy, and grazing incidence X-ray diffraction (GIXRD). The results obtained from the characterization techniques are presented and discussed, including the damage density concentration calculated from SRIM simulation and the SEM, GIXRD and Raman spectroscopy results for the samples synthesized at 900°C, 1000°C, 1100°C and 1200°C. The chapter concludes with a summary of the main findings of the study.

Chapter 6: Summary and Conclusion

The final section of this chapter discusses the synthesis of boron nitride (BN) nanostructures, particularly nanotubes, using chemical vapor deposition (CVD), and the use of ion implantation to selectively introduce defects into BN nanostructures. The aim of the study was to look into how the properties of BN nanostructures are affected by ion implantation, such as stress levels, local density, and crystallinity. The samples were analysed, and the results of this study can potentially aid in the development of BN-based materials for various applications, such as electronics, optics, and aerospace engineering.

CHAPTER 2

2 THEORETICAL ASPECTS OF BNNTS IN NANOTECHNOLOGY

Norio Taniguchi of the University of Tokyo coined the term "nanotechnology" in 1974 [7]. It refers to the process of modifying materials on a nanometre scale. It is a branch of material science that is expanding rapidly. Although there are many different sizes and shapes of nanostructures, nanotubes in particular are the most significant ones in the field of nanotechnology.

2.1 NANOTUBES

In 1991, Sumio Iijima discovered nanotubes [8]. They are rolled up hexagonal sheets and have a tubular structure. Nanotubes can be divided into two groups: single wall (SWNTs)[1] and multi-wall (MWNTs)[2], Figure 2.1. Nanotubes can also be categorized as armchair, chiral, or zigzag structures. Based on how the sheet of atoms rolls, different categories are created. The axial direction determines whether the nanotubes are armchair, zigzag, or chiral [9]. Armchair or zigzag nanotubes are produced when a sheet of atoms is rolled along the symmetry axis; otherwise, chiral nanotubes are produced, Figure 2.2 [10]. The mechanical toughness, thermal conductivity, density, and electrical conductivity of nanotubes are all affected by structural variations. Some nanotubes are conductors attributable to their metallic nature, whilst others are semi-conductors due to their structural makeup.

[1] Single wall nanotubes (SWNTs) are made up of a single layer of atoms.
[2] Numerous circular tubes wrapped inside of one another make up multi wall nanotubes (MWNTs).

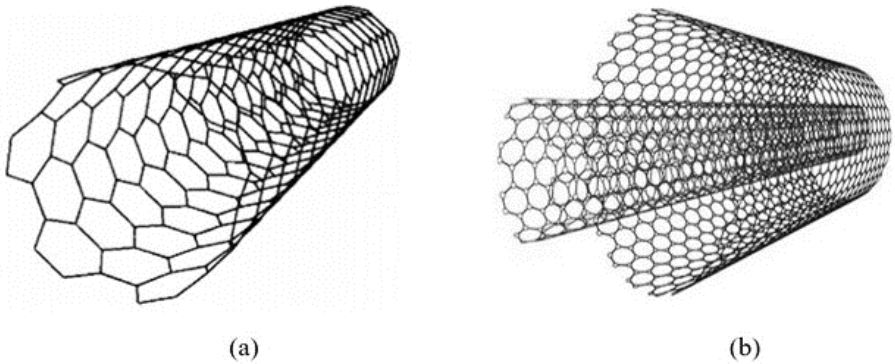

Figure 2.1: (a) Single-wall nanotube (MWNT), (b) Multi-wall nanotube (SWNT) [11].

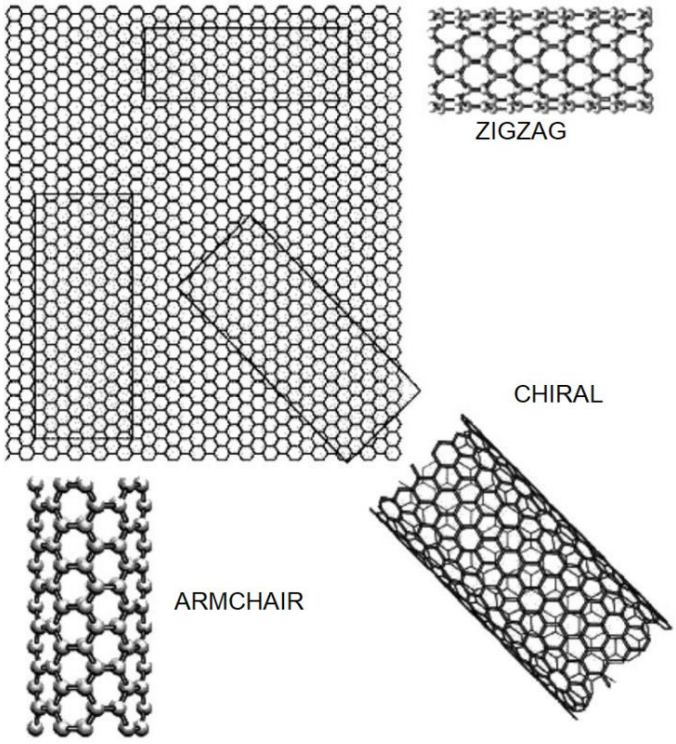

Figure 2.2: Structural types of nanotubes [9][10].

2.2 BORON NITRIDE

One of the Group III-V semiconductors is boron nitride (BN), which is composed of two elements from the Periodic Table's 3rd and 5th columns. Soft sp^2 graphite-like and hard sp^3 diamond-like bonded phases that are similar to carbon in distinct ways are produced by BN. The two stable crystal structures of boron nitride are hexagonal (h-BN, sp^2 graphite-like) and cubic (c-BN, sp^3 diamond-like), the latter being the second hardest material after diamond [2], Figure 2.3 displays the crystal lattice structure of hexagonal-BN, where the flat basal planes are composed of three hexagonal rings consisting of nitrogen and boron atoms. Each boron atom in the lattice structure is bonded to a nitrogen atom. On the other hand, the cubic-BN has a unit cell that is made of four boron and four nitrogen atoms that are tetrahedrally connected. The structure of cubic-BN is known as the zinc-blende structure.

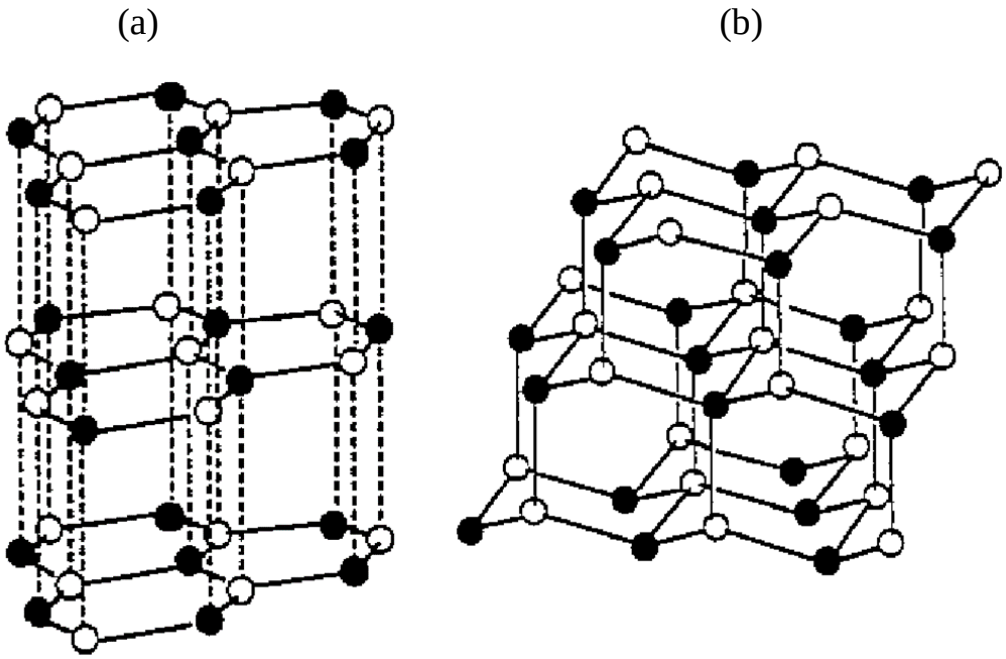

Figure 2.3: (a) h-BN structure, (b) c-BN structure [2].

2.2.1 BORON NITRIDE NANOTUBES (BNNTS)

A theoretical prediction regarding the presence of BNNTs was made in 1994 [12]. Boron nitride has several relevant properties, including being isoelectronic to carbon and possessing a stable hexagonal structure similar to graphite. Carbon nanotubes (CNTs) have attracted a lot of experimental and theoretical attention since they were first discovered in 1991 [8]. Depending on their chirality or helicity, CNTs can either be a conductor or a semiconductor, but BNNTs are always a wideband gap semiconductor [13] [14].

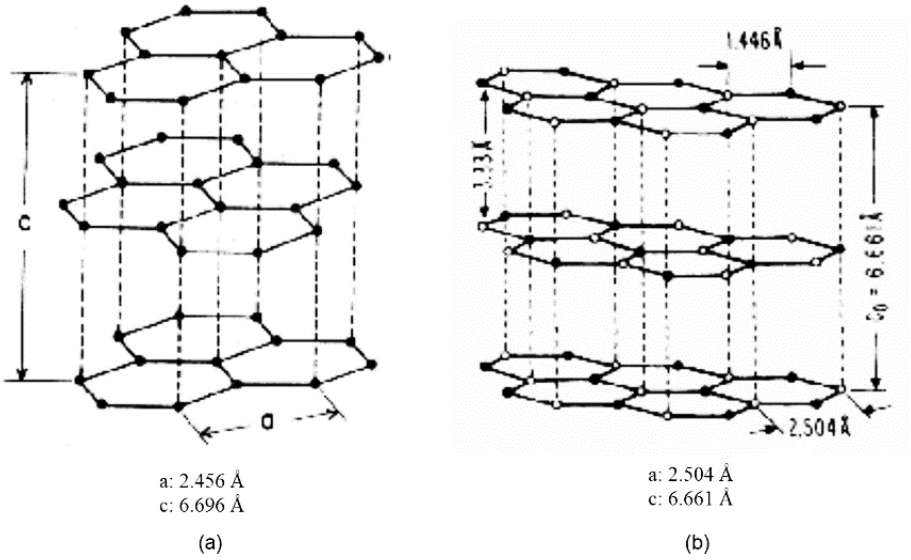

Figure 2.4: Structures of: (a) Graphite. (b) Boron nitride [15]

Figure 2.4 shows that graphite and hexagonal boron nitride, which are the parental structures of carbon nanotubes and boron nitride nanotubes, are quite similar. Both of these materials are made up of hexagonal lattice layers; however, h-BN is made up of alternating boron and nitrogen atoms, whereas graphite has carbon atoms in every position in the lattice. The layering of these materials differs somewhat. Layers of h-BN are organized in such a way that boron atoms in one layer are immediately on top of nitrogen atoms in adjoining layers, and vice versa. Hexagons in graphite

are misaligned and do not stack on top of one another, which results in a different stacking pattern. The in-plane lattice constants and interlayer distances for graphite and h-BN are 2.46 Å, 3.35 Å, and 2.50 Å, 3.33 Å, respectively [15].

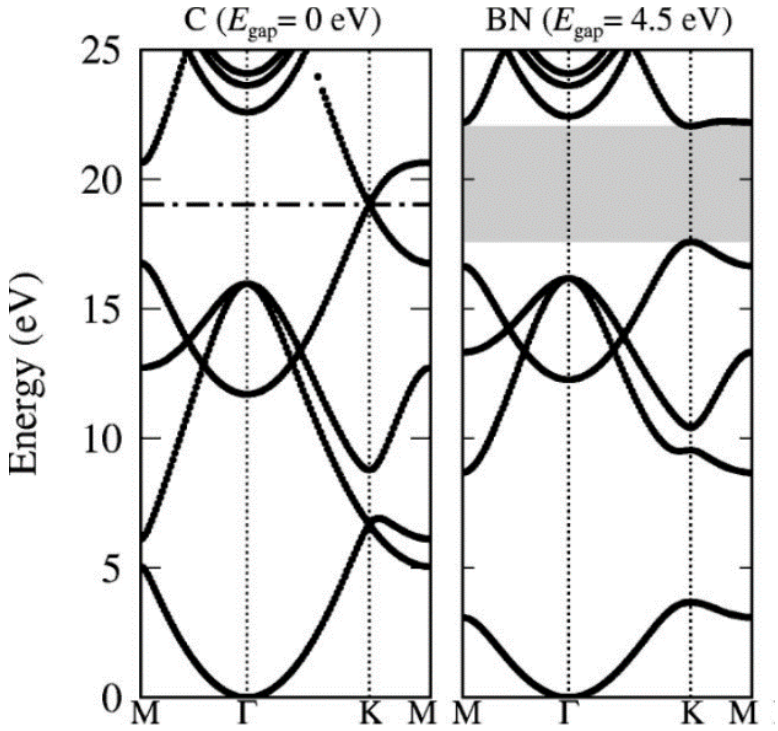

Figure 2.5: LDA (local density-functional approximation) band structure of BN sheet compared with that of a single graphite sheet in the hexagonal Brillouin zone. The Fermi level and band gap are indicated, respectively, by the dot-dashed line and the shaded area [6].

In Figure 2.5, the BN single layer LDA band structure is compared to that of a graphite sheet at the Fermi level. Graphite and h-BN have quite distinct electronic properties. Two bands cross each other at Fermi energy in a single sheet of graphite. For a single layer of h-BN, analogous bands do not overlap each other, resulting in a 4.5 eV band gap[3] [6].

[3] The band gap of **bulk** h-BN has been measured experimentally to be 5.8 eV.

Carbon nanotubes (CNTs) can be either metallic or semiconductor in nature. All boron nitride nanotubes (BNNTs), however, are semiconductors. BNNTs have a constant electron band gap of 5.5 eV regardless of tube diameter or chirality [6].

Table 2.1: Comparison of properties of BNNTS and CNTs.

	BNNTs	**CNTs**
Electrical properties[15]	Always semiconducting [above 4 eV gap]	Metallic or semiconducting
Young's modulus[16]	1.18 TPa	1.33 TPa
Thermal conductivity[15]	600 W / mK	3000 W / mK
Oxidation resistance[17]	Stable up to 800 °C	Stable up to 300 to 400 °C in air
Elastic Modulus [12]	~ 850 GPa	150 GPa

The properties of BNNTs and CNTs are compared in **Table 2.1**. Because of their comparable Young's moduli, both materials (BNNTs and CNTs) are equally appropriate for mechanical applications. Due to their higher level of chemical resistance than CNTs, BNNTs can endure more extreme conditions and reactions, but they have lower thermal conductivity. Nonetheless, BNNTs have properties that are just as desirable for application as carbon nanotubes, if not more so. As a result, further research into BNNTs is essential.

2.2.2 SYNTHESIS METHODS OF BORON NITRIDE NANOTUBES

The methods that have been successful in creating carbon nanotubes (CNTs), such as arc discharge [18], ball-milling [19], laser ablation [20], substitution reaction of boron nitride (BN) atoms from CNT templates [21], and chemical vapour deposition [22], have also been utilized to produce boron nitride nanotubes (BNNTs). Each method involved specific precursors and conditions that were carefully chosen to facilitate the synthesis of BNNTs.

2.2.2.1 ARC DISCHARGE

The first experimental finding of BNNTs in an arc discharge was made by Chopra et al. in 1995 [23]. In a hollow tungsten anode electrode, a BN rod was introduced as a starting material to produce BNNTs. The anode component rapidly vaporized by the arc plasma that formed between the cathode and anode. The chamber used for the synthesis of BNNTs was pumped down to the ideal pressure level, and the electrode pair gap adjusted to a maximum of 1 mm. Discharge occurs between 20 and 40 Volts, and up to 150 A of current. The temperature can exceed ~4000 K during the discharge procedure. Due to the insulating property of boron nitride (BN) rods, which could disrupt the discharge process, they were substituted with boron-containing chemical compounds that are highly conductive, such as YB_6 and HfB_2, or a combination of boron, nickel, cobalt, and nitrogen gas. By doing this, the anode's conductivity was raised while simultaneously providing catalytic activity for the formation of BNNT [24][25][26]. By arc-melting YB_6 powder, Narita et al. [24] were able to create BNNTs, and the presence of YB_2 particles at the ends of the nanotubes provided proof that yttrium had a catalytic effect on the production of few-walled BNNTs (4–10 layers). In their production of BNNTs, Loiseau et al. [25] used a HfB_2 electrode that was hot-pressed and of high purity, and they observed that a significant number of the nanotubes produced had fewer layers and flat ends. Through the addition of a small quantity of nickel and cobalt as the main catalysts to a boron-rich conducting electrode, Cumings et al. [26] successfully produced a large quantity of double-walled BNNTs using an arc discharge method. The

fundamental drawback of the arc discharge technique is that because the reaction zone at the arc core is contained in a small volume, it is challenging to generate BNNTs on a large scale.

2.2.2.2 BALL-MILLING

Boron precursors are introduced into the stainless-steel milling chamber, which contains steel balls. Chen et al. [19] ball-milled boron powder for 150 hours in the presence of NH_3 gas and then subjected it to isothermal annealing at 1200°C in an N_2 atmosphere. The fundamental concept of the procedure is that mechanical energy is applied to the boron precursor to initiate structural, morphological, and chemical changes. In a subsequent publication [27], the findings suggested that a lengthy milling process would be essential to obtaining a large yield of BNNTs because it would increase the nitration reaction between boron and NH_3, which would result in more nucleation structures that would aid in the creation of BNNTs. Iron fragments from the milling ball and chamber combined with boron powder can serve as a strong catalyst to accelerate the nitriding reaction during the procedure. The original morphology of BN clusters on iron seed particles determined the type of as-grown BNNTs, according to Kim et al. [28], who investigated the development of BNNTs from amorphous boron coated on the surface of catalytic iron seed particles produced in stainless steel containers. In his research, crystalline boron powder transformed into an amorphous structure, which then catalyzed the synthesis of BNNTs during the annealing period. Surface iron fragments were present on the amorphous framework. Since milling was done in nitrogen gas, no nitriding reaction took place throughout the procedure. It should be mentioned that the end product had a relatively poor purity since it frequently includes BNNTs in addition to amorphous boron and boron nitride flakes.

2.2.2.3 LASER ABLATION

A boron or boron nitride target is heated using a laser to a temperature higher than the melting point of boron (around 2000°C) inside a furnace. This causes the target to change from a solid to a liquid state and react with nitrogen gas. The temperature of the area exposed to laser radiation rises to several hundred Kelvin due to the energy generated by the light from the laser. Carrier gas (i.e., helium and nitrogen) is introduced into the oven during laser ablation. The generated nanotubes are transported through this carrier gas then gather on the cool metal trap. The first successful use of the laser ablation approach in BNNT synthesis was made by Golberg et al. [20], when hexagonal and cubic BN targets were heated by a laser to 5000 K in a diamond anvil cell under extremely high nitrogen gas pressure (5-15 GPa), multi-walled BNNTs were created. Similar to the way CNTs are made, Yu et al. [29] produced BNNTs by applying laser energy to a target that had been formed by combining h-BN powder with Ni-Co (cobalt and nickel nano powder) catalyst.

2.2.2.4 CARBON SUBSTITUTION

Han et al. [30] used this approach first. They utilized CNTs as a template to create BNNTs since the structures of CNTs and BNNTs are similar. The carbon substitution method substitutes the carbon atoms in the CNTs with boron and nitrogen atoms. The reaction was conducted in an induction-heating system using graphite-based susceptors. An uncovered sintered graphite crucible containing B_2O_3 material was then filled with CNTs. They placed cubicles of graphite into the induction furnace and maintained them there at 1773 K for 30 minutes. They created the CNTs they used with a Chemical vapour deposition (CVD) process, and the resultant powder was further refined through oxidation. Later, this method was employed to create BNNTs from B-C-N tubes [31]. Although this method yields fine BNNT structures, it is still difficult to remove carbon from the finished product. This synthesis process is also undesirable since an induction furnace is required and high temperatures are involved. The reaction expected to take place can be expressed as:

$$\mathbf{B_2O_3 + 3C(nanotubes) + N_2 \rightarrow 2BN(nanotubes) + 3CO} \qquad \mathbf{2.1}$$

To interact with the carbon nanotubes and the nitrogen (N_2) gas, it was anticipated that the boron oxide gas produced by the B_2O_3 powder would propagate up towards the area holding the nanotubes.

2.2.2.5 CHEMICAL VAPOUR DEPOSITION

One of the most well-known techniques for creating carbon nanotubes has been chemical vapour deposition (CVD), and it has most recently been utilized to create boron nitride nanotubes. In comparison to other methods, this method offers greater controllability of growth parameters in terms of growth mechanism, experimental setup, precursors, catalysts, and temperature, guaranteeing outstanding nanomaterial quality [30].

CVD was used for the first time to synthesize purified BNNTs using borazine as a precursor. However, due to the danger of borazine, the technique was not used [32]. As a result, scientists introduced the most effective non-toxic precursors while also creating their own CVD processes. There are three primary stages that the significant advancements in BNNTs CVD synthesis may be divided into. Tang et al. [33] and Zhi et al. [34] constituted the initial step. In this step, BNNTs were synthesized in high yield using the Boron Oxide CVD (BOCVD) process in an induction furnace using boron (B), magnesium oxide (MgO), and iron oxide (FeO) as precursors. The production of BNNTs followed the Vapour Liquid Solid (VLS) growth process, because at a certain temperature, the interaction of the compounds produces B_2O_2 vapours (i.e., melted catalyst particles) [35]. These catalysts condensate on the substrate when their partial vapour pressures are suitably raised. The produced B_2O_2 vapour combines with N_2 from the NH_3 gas to form the BN-species. These species are subsequently diffused into the condensed catalysts until they precipitate as BNNTs [36]. The second step is that of Lee et al. [22] and Zhi et al. [34], wherein the induction furnace is replaced with a traditional horizontal tube furnace. Additionally, pure BNNTs were grown directly on Si or SiO_2 substrates in the

temperature range 1100-1200ºC using a specific ratio of the precursors (B, MgO, and FeO) (2: 1: 1, 4: 1: 1). The process was coined TCVD. The last stage is that of Lee et al. [22] and Ahmad et al. [37]. By using argon gas (to create an inert the atmosphere in tube) instead of vacuum, the TCVD method was made even simpler. Thus, the method created is known as argon aided TCVD. This simplified strategy was utilized in this thesis since it helped to reduce the costs of the experimental set-up.

Table 2.2: Various methods used for synthesizing BNNTs [38].

Technique	Temperature (ºC)	Advantages	Dis-advantages
Arc-discharge	3500	Highly crystalized, SWBNNTs and MWBNNTs	Containing BN onion and cages like morphologies as impurities
Laser ablation	1200-5000	Highly crystalized, SWBNNTs and MWBNNTs	Containing BN cones etc. as impurities
Carbon substitution	750-1580	Having controlled morphology	Containing carbon in lattice as Impurities.
Ball milling	1000-1200	Large yield	Low purity with B, h-BN, and BN fibre as impurities
CVD	1100-1200	High quality and large quantity up to gram level	Search for a specific method (CVD) with reaction parameters and precursors

CHAPTER 3

3 ION IMPLANTATION IN BORON NITRIDE

Ernest Rutherford and Niels Bohr performed experiments and developed theory that revealed the physics of ion-solid interactions to comprehend how particles enter, slow down, and rest in matter [39]. Ion solid interactions are based on the acceleration of energetic ions into a solid target material's surface, which causes the emission of radiation (such as photons) and particles (such as electrons), which may then be quantified using various characterization methods [40]. It is possible to obtain energetic ions such as alpha particles from radioactive sources or from simple nuclear processes involving neutrons from a reactor that can emit protons, tritons, and other particles. The development of suitable particle accelerators is now a more straightforward method of generating energetic particles with adequate flux in a practical energy range (i.e., keV or GeV) [41]. Ion implantation, substrate sputtering, and ion beam mixing are just a few of the procedures that result from ion-solid interactions. This thesis has solely employed ion implantation.

3.1 ION IMPLANTATION

Ion implantation is a technique that is used to introduce impurities into solids by accelerating the appropriate ions onto the material at energies between electron volts and mega-electron volts in a consistent and dependable manner. Its main field of use is semiconductor research, where it is the preferred method for electrical doping of semiconductors [42]. The majority of the ions settle in a shallow surface layer of the target material, becoming neutral atoms and producing defects in the slowing down process. The interaction of the atoms and produced point defects in the material alters the characteristics of the implanted material. The implantation depth and ion concentration can be regulated by adjusting the energy and fluence of the ions; as a

result, an accurate adjustment of the energy and fluence can produce the appropriate impurity and damage profile.

3.2 PROJECTED RANGE (R_P)

The energy loss and path deviation of ions in the studied material is a result of collisions with the electrons or nuclei of the material, which occur as a consequence of the ion-material collisions. The core principle of energetic ion impact is the extremely high localized density of the energy delivered to the target by the particles, as opposed to the interaction of energetic electrons or photons with matter [41]. In this manner, solids may experience the same energy density for a very brief period of time (10^{-17} to 10^{-15} s) within a very small volume (10^{-17} to 10^{-16} cm^3), which is otherwise only encountered in the area of an exploding hydrogen bomb. The target material's "stopping power" can be defined as the energy lost by an ion per unit path length. It is made up of two parts: nuclear stopping power ($\boldsymbol{S_n}$) and electronic stopping power ($\boldsymbol{S_e}$), Equation 3.1[4] [43]. Thus, the measurement of the length $\boldsymbol{x}$ along the path of the ion (also referred to as total range, $\boldsymbol{R}$) or along the line of the beam (also referred to as projected range, $\boldsymbol{R_p}$) is a random variable.

$$\boldsymbol{S = -\frac{dE}{dx} = S_n + S_e} \qquad \textbf{3.1}$$

Figure 3.1 shows the projected range, which essentially indicates the depth at which most ions stop. It is possible to estimate the distribution of implanted ions around a certain depth ($\boldsymbol{R_p}$) by using a Gaussian approximation with a standard deviation ($\Delta\boldsymbol{R_p}$) [44][45]. So, the ion concentration can be written as

[4] From equation 3.1, $\boldsymbol{S_n} = \left(\frac{dE}{dx}\right)_n$ and $\boldsymbol{S_e} = \left(\frac{dE}{dx}\right)_e$

$$C(x) = C_p - \frac{(x - R_p)^2}{2\Delta R_p^2} \quad \textbf{3.2}$$

where C_p, which is defined as the peak concentration, is

$$C_p = \frac{D}{\sqrt{(2\pi\Delta R_p^2)}} \cong \frac{0.4D}{\Delta R_p} \quad \textbf{3.3}$$

The dose of implantation is determined by the sum of ions implanted per unit area of the specimen, which is represented by the variable D. The variable I corresponds to the beam current, which is scanned over the surface of the specimen for a specific period of time (t). The integration of the beam current over time gives the total implanted charge (Q), which can be calculated using the equation provided.

$$Q = \int_{t_0}^{t_1} I dt \quad \textbf{3.4}$$

Therefore, the fluence (D) equals the total embedded charge, Q, divided by the cross-sectional beam area, A, multiplied by the ion charge (q_i). Thus, the result is the following equation:

$$D = \frac{Q}{q_i A} \quad \textbf{3.5}$$

The SRIM® computer application may be used to execute TRIM Monte Carlo computations to estimate ion and recoil atom distribution and collision details [42].

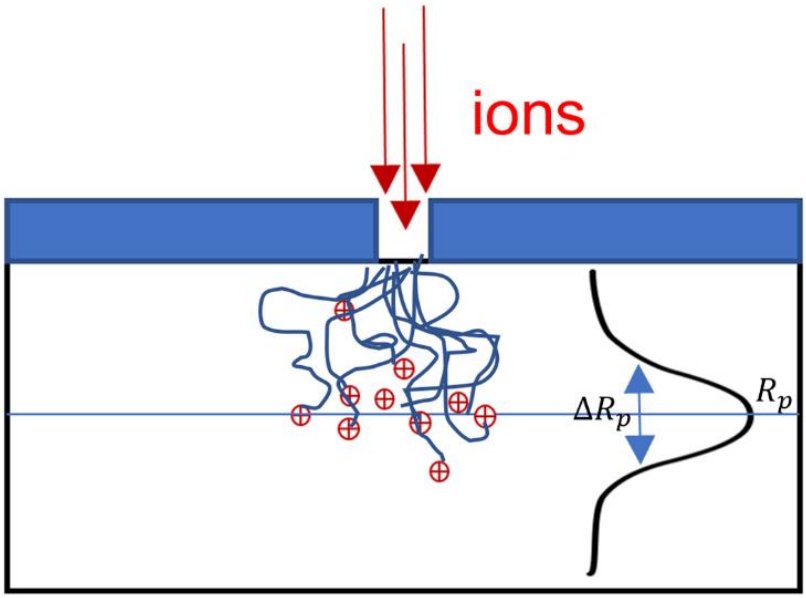

Figure 3.1: Diagram illustrates the projected range, which indicates the position where the majority of ions stop.

3.2.1 ELECTRONIC STOPPING

Electronic stopping occurs when the implanted ion collides inelastically with the target atoms' electrons. The target atom may get excited and ionized as a result of the collisions. As the ions move through the electron cloud of a target atom, most ions will be fully stripped of electrons as they slow down in a solid, the slowing down is due to the excitation of electrons in the electron cloud of solid atoms to higher quantum states. The ions will progressively decelerate ultimately reaching a point where it is effectively neutralized [43]. These ions are neutral at the end of their range (low ionization state). After coming to rest, the ion takes up electrons (e.g., from the conduction band) and gets back to its normal neutral state, i.e., becomes an atom. At high energies and velocities, ions undergo electronic stopping, which results in reduced interaction with target nuclei, because when ions are moving fast, they exert a force on the heavy nuclei for too short a time to displace them. As a consequence, there is minimal displacement of target atoms, leading to less damage caused by electronic stopping in terms of target atom displacement.

The relationship between energy $\boldsymbol{E}$ and electron stopping power ($\boldsymbol{S_e}$) is given by the following expression, Figure 3.2 [43][44]:The relationship between energy $\boldsymbol{E}$ and electron stopping power ($\boldsymbol{S_e}$) is given by the following expression, Equation 3.6 [44]:

$$S_e(E) = \left(\frac{8\pi e^2 a_0}{\varepsilon_0}\right) \frac{z_1 z_2}{\left(z_1^{\frac{2}{3}} + z_2^{\frac{2}{3}}\right)^{\frac{3}{2}}} \left[\frac{E}{E_0}\right]^{\frac{1}{2}} \quad \textbf{3.6}$$

Where $\boldsymbol{z_1}$ and $\boldsymbol{z_2}$ are the atomic numbers of the target and the ion, respectively, and $\boldsymbol{a_0}$ is the Bohr Radius. The electronic stopping power $\boldsymbol{S_e(E)}$ is directly proportional to the square root of the energy of the incident ion, as indicated in Equation 3.7:

$$S_e \propto E^{\frac{1}{2}} \quad \textbf{3.7}$$

The stopping power maximum is where the velocity of the ions is equivalent to the target electrons' Bohr velocity, $\boldsymbol{v_o}$ ***(m/s)***, is where electronic stopping is at its optimum, which occurs when the incident ion has an energy between 10 to 100 MeV. At higher ion energies the interaction time with the electrons drops off, and so does their stopping power. With ion energy of ~100 keV, this region of high-energy physics is irrelevant for the purpose of this thesis.

3.2.2 NUCLEAR STOPPING

As the ion decelerates, the electronic stopping power decreases in magnitude, and the nuclear interaction becomes the dominant process responsible for the ion's stopping. Nuclear stopping occurs through elastic collisions between the ion and the target nucleus and is commonly described as an interaction between two nuclei. The massive damage to the material lattice structure is caused by nuclear interactions

[44]. At low energies, usually below 10 keV for light ions in boron nitride, nuclear stopping dominates, and ions interact mainly with the nuclei of the target material. During this interaction, when ions transfer more energy than displacement energy ($\boldsymbol{E_d}$) to the target nuclei, this leads to displacement of atoms from their initial lattice sites. This displacement can cause significant damage to the material by creating structural flaws such as vacancies and interstitials in the crystal structure.

The following expression relates nuclear stopping power to energy, Equation 3.8:

$$S_n(E) = N\frac{\pi^2}{2}E^{-2}a\left[\frac{z_1 z_2 m_1}{m_1 + m_2}\right] \qquad \textbf{3.8}$$

The variables N, a, z_1, z_2, m_1, and m_2 are atomic concentration of the target material, lattice parameter, atomic numbers of the ion and target, respectively. Equation 3.9 below indicates that there is an inverse square relationship between the energy of the incident ion and nuclear stopping:

$$S_n(E) \propto E^{-2} \qquad \textbf{3.9}$$

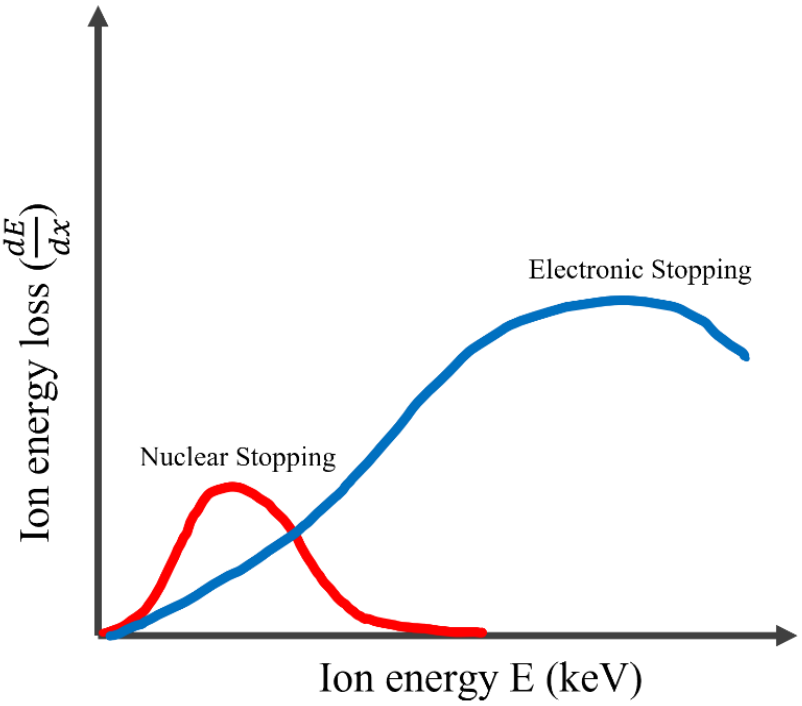

Figure 3.2: Variation of ion stopping power with ion energy, separately indicating the nuclear and electronic contributions to the total stopping power.

Figure 3.2 shows that both stopping powers rise with energy until they approach an optimum output, after which they fall [41]. At energies that are many orders of magnitude greater than the nuclear threshold, electronic power transfer achieves its maximum value. While nuclear energy transfer predominates for low energy heavy ions with stopping powers in the eV/Å range, light ions of all energies and energetic heavy ions with stopping powers in the keV/Å range supply a greater amount of energy via electronic excitation than through nuclear collisions.

3.3 RADIATION DAMAGE

The target material sustains radiation damage when energetic ions repeatedly interact with the target atoms, knocking them out of their lattice locations and rupturing chemical bonds in the process. If an ion possessing an energy greater than the displacement energy (E_d) of the target material and collides with an atom in its lattice position, the atom may be removed from its position, resulting in the creation of a vacancy. This process gives rise to Frenkel pair defects [46]. A displacement spike occurs when the recoil atom's energy exceeds (E_d), which will further lead to the formation of Frenkel pairs. A collision cascade typically generates a significant number of Frenkel pair defects. Once the recoil energy of the ion drops below the displacement energy (E_d), it can no longer displace the target nuclei from their lattice sites. Instead, it will lose its energy via collisions, leading to atomic vibrations within their lattice sites. The nearby nuclei share the vibrational energy caused by the collision, which manifests as heat. A thermal spike of this type often forms inside a plasma-like structure and lasts for around $\sim 10^{-12}$ seconds. However, since BN is analogous to carbon, the formation of diamond defects reveals they are not significantly influenced by displacement spikes [47]. When temperatures are appropriate, point defects can move through diffusion. Depending on the layer's depth-width and annealing temperature self-interstitial atoms that are diffusing can either diffuse out of the layer being implanted or meet up with vacancies and remove them.

Derry et al. [47] found that different temperature conditions influence the movement of point defects within the damage cascade created by the implanted ion in their research on 'point defect engineering' in ion-implanted diamond. All point defects remain intact at extremely low temperatures (typically below 320K in diamond). Higher temperatures (between 320K and 800K in diamond) cause the interstitials to move while the vacancies stay immobile, and at even higher temperatures (usually above 800K in diamond), all of the basic defects become mobile. Generally, interstitials have a greater degree of mobility than vacancies [47].

The extent of radiation damage resulting from ion implantation depends on various implantation parameters such as implantation fluence, temperature, target material nanostructure, and ion mass. During and after ion implantation, ordinary defects like

vacancies and interstitials may interact to generate disordered regions across the target material, including impurity clusters, dislocation loops, grain boundaries, voids, crystalline inclusions, or gaseous inclusions that may span a substantial region of the material. It is important to monitor any effects that the additional implanted atoms may have on the chemistry of BN.

3.3.1 RADIATION DAMAGE IN BORON NITRIDE

The SRIM (Stopping and Range of Ions in Matter) program was used to perform computer simulations for a comprehensive understanding of the ion implantation process on h-BN using various ions. Monte Carlo simulations were utilized by this program to estimate the range and damage distribution caused by high-energy ion interactions with the target material. To determine the depth distribution of implanted ions and simulate the radiation damage profile, the SRIM-2013 version was employed, considering the vacancies generated during the ion collision cascade. For ions employed in the implantation procedure, simulations were performed at 150 keV. He^+, Li^+, B^+, and Ne^+. These data were used to calculate the simulated damage density and range of the implanted ions.

Figure 3.3 and Figure 3.4 demonstrate that heavier ions propagate the surface less deeply while causing significant damage. Ions that are lighter can travel deeper into the surface while causing less damage. As atomic mass increases, penetration depth decreases, implying that heavier ions do not reach as far beneath the surface of h-BN.

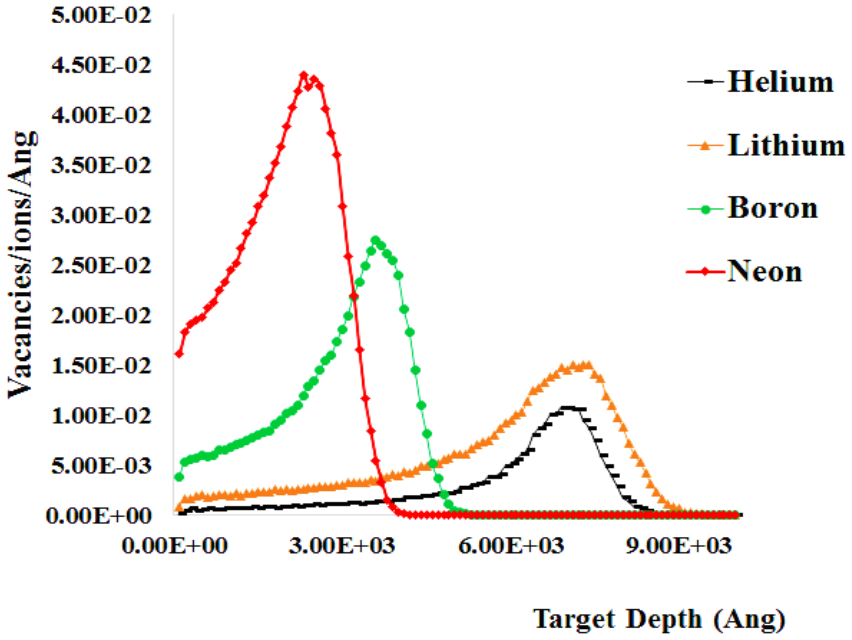

Figure 3.3: Graph generated by the SRIM model shows the relationship between the depth of penetration and the number of vacancies per ion and unit length (measured in Å) for various ions, namely boron, lithium, helium, and neon ions, which were implanted into h-BN at 150 keV.

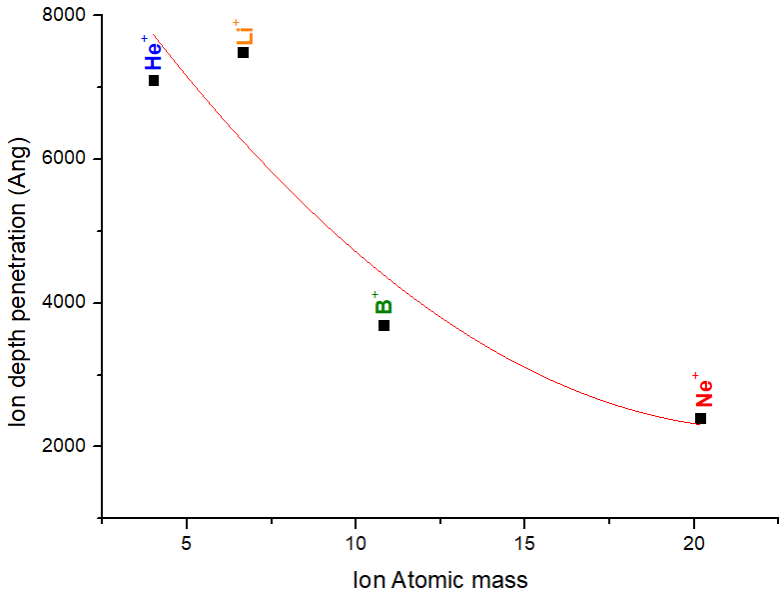

Figure 3.4: Relationship between ion penetration depth and the atomic masses of different ions.

3.4 ION CHANNELLING EFFECT

When energetic charged particles strike a solid target, different physical events can take place, including Rutherford scattering, energy-loss processes, secondary-electron emission, nuclear reactions, and X-ray emission. These processes' cross sections are all influenced by the impact parameters ($\boldsymbol{b}$) involved in collisions with certain target atoms [48]. The distribution ($\boldsymbol{v_b}$) of the impact parameters is unaffected by the relative orientations of the target and beam directions if the target material is homogenous and isotropic. The motion of both the target atoms and the projectiles becomes random with respect to each other as a consequence. [40].

$$\boldsymbol{v_b(b) \approx 2\pi b} \qquad \textbf{3.10}$$

The Channelling Effect is characterized by the correlation between the orientation of the target atoms and the distribution of impact parameters in a single crystal, which is dependent on the crystal structure, as well as the mass and energy of the incoming ions. This effect occurs when the angle between the crystal axis and beam direction is less than a critical angle. When an incident ion channelled, it enters the target substance more deeply than it would have otherwise by moving down the spaces in the crystal structure. This happens when an ion approaches a row of atoms at reducing angles, with each contact reducing the angle with little energy loss.

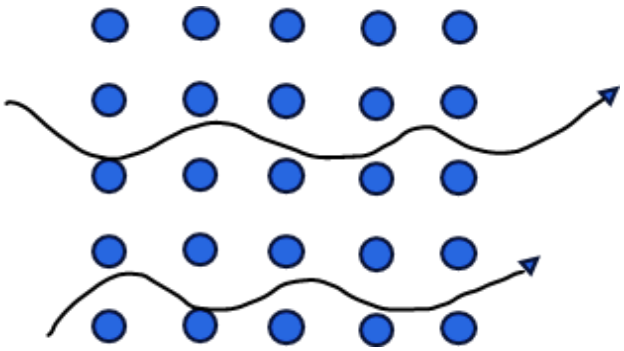

Figure 3.5: Schematic representation of the channelling effect in a monocrystalline material [48].

CHAPTER 4

4 EXPERIMENTAL METHODS

A thorough overview of the experimental and characterization tools used in this work is provided in this chapter. It provides a description of the various materials used, their preparation, the experiments done on them, and ultimately the characterization techniques used.

4.1 SAMPLE PREPARATION

Silicon wafer (100) was cut into small pieces and placed in an ethanol-containing beaker. The Si-substrates were cleaned in an ultrasonic bath. The crucible was filled with a combination of boron (B), magnesium oxide (MgO), and iron (ii) oxide (Fe_2O_3) (2:1:1 molar ratio), and the Si-substrates were put on top of the precursors. The crucible was then moved to a tube furnace.

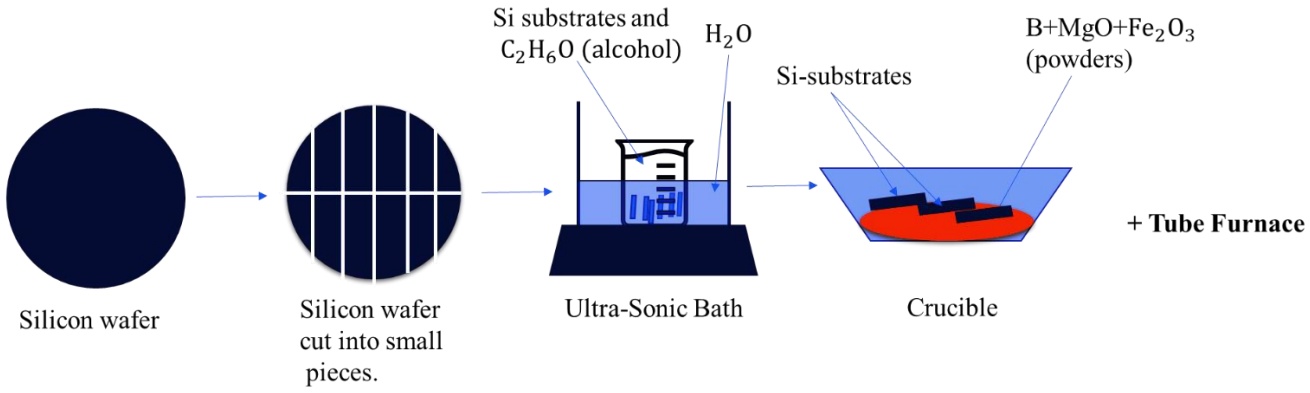

Figure 4.1: Flow diagram, illustrating the preparation of samples.

4.2 CHEMICAL VAPOUR DEPOSITION (CVD)

Lee, Chee Huei, et al [22], demonstrated that the synthesis of boron nitride nanotubes (BNNTs) using the boric oxide chemical vapour deposition (BOCVD) method is an important development and can be easily replicated by researchers who work on the growth of carbon nanotubes (CNTs).

The crucible containing the precursors and Si substrates was placed within a quartz tube. The quartz tube was then put into the furnace's tube chamber. The gas cylinders were connected to the quartz tube gas inlets. Argon gas was fed through the system to eliminate air and produce an inert atmosphere. Simultaneously, the temperature was gradually raised. When the desired temperature was reached, the argon was turned off and ammonia (NH_3) gas was added into the system. The CVD synthesis were carried out for one hour at temperatures of 900°C, 1000°C, 1100°C and 1200°C, Figure 4.2.

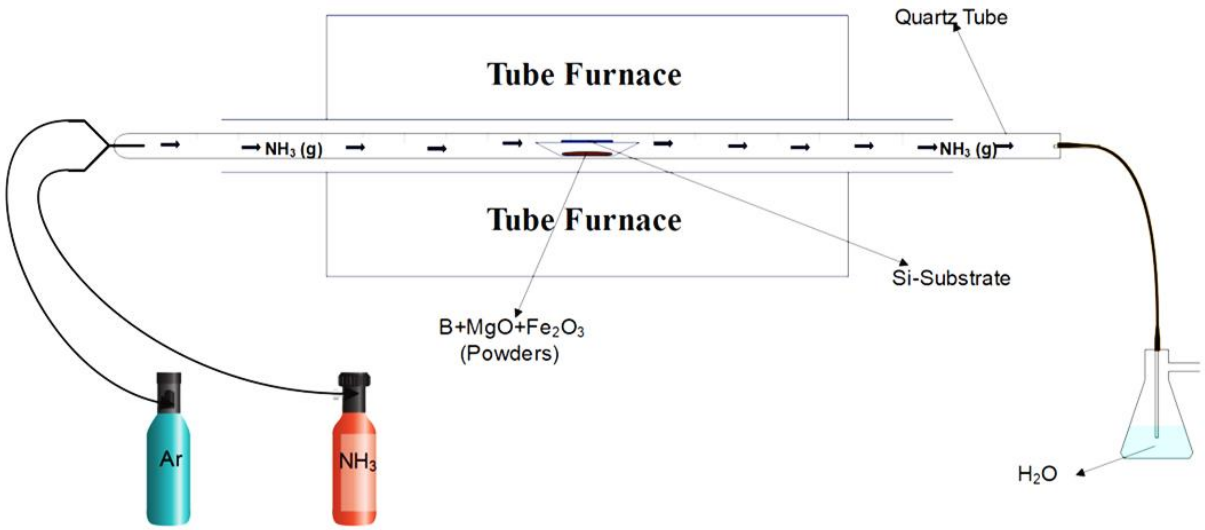

Figure 4.2: Schematic illustrating the CVD experimental procedure.

At high temperatures, reactive B_xO_y vapours will react with NH_3 to generate BNNTs. MgO and Fe_2O_3 operate as catalysts. The reason water is used as a filtration system

is because since there is hydrogen bonding, and ammonia vapour is very soluble in water. Ammonium hydroxide (NH_4OH) is created when ammonia gas dissolves in water. This compound can then break down into ammonium (NH^{4+}) and hydroxide (OH^-) molecules.

Figure 4.3: CVD Experimental set-up using Carbolite CTF Tube Furnace (Serial No. 21-103513).

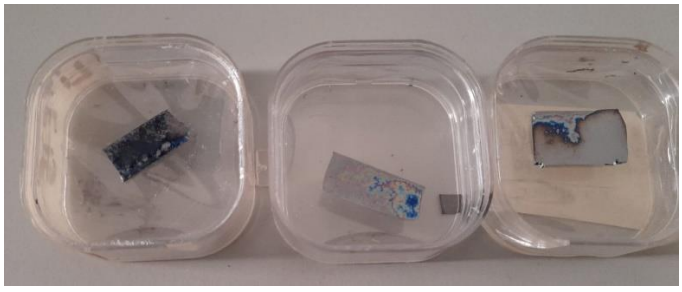

Figure 4.4: Si-substrates after deposition of BNNTs.

4.3 ION IMPLANTATION

The ion implantations were performed at iThemba LABS in South Africa, using the Varian-Extrion 200-20A2F ion implanter, which can accelerate ions to energies from 10 keV to 170 keV, Figure 4.5. These measurements were done using B^+ ions at room temperature. All implantations were done at energy 150 keV as in E. Aradi et al. [4] and our prior work [5]. Here, the fluences used were 1×10^{14} and 5×10^{14} ions/cm^2.

Figure 4.5: Varian-Extrion 200-20A2F ion implanter.

4.3.1 PRINCIPLES OF ION IMPLANTATION

An ion implantation system typically consists of an ion source, a mass analyzing magnet, an electrostatic accelerator, a beam manipulation system, and an end station section that houses the target sample, Figure 4.6.

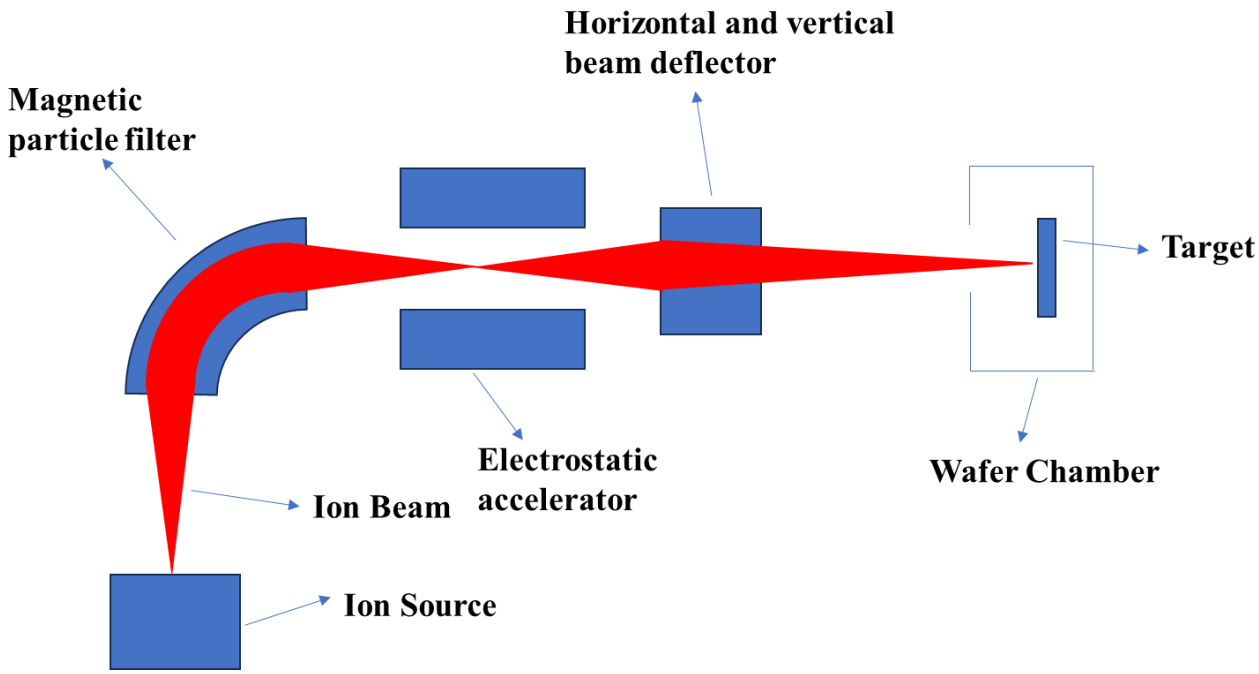

Figure 4.6: Schematic diagram of the 200-20A2F ion implantation system [49].

Desired ions are accelerated to the samples in a high vacuum (10^{-5} to 10^{-7} Torr) to prevent collision with certain remaining gases. To achieve the desired pressure, a pumping system is thus needed. A typical pumping system includes a Turbo molecular pump (1×10^{-7} Torr) assist by a rotary vane pump (1×10^{-3} Torr) for roughening. Once the chambers are at 10^{-7} Torr the roughing valve is closed and the ion pump and titanium sublimation pump take over, bringing the pressure down to 10^{-10} Torr.

4.3.1.1 ION SOURCE

The 200-20A2F ion implanter utilizes the Freeman Arc Discharge ion source which is capable of generating ion beams from a variety of materials, including solids and gases [49]. Helium, neon, lithium chloride (LiCl), or boron trifluoride (BF_3) are examples of gases that are injected into the ion source. By running a large current through a tungsten filament, thermionic emission produces electrons in the ion source. When these electrons hit the gas molecules in the source chamber, the valence shell electrons are stripped away, creating ions. Positive ions are drawn to the acceleration slit by an electron reflector electrode driven with a negative potential of about 2 kV in relation to the filament, and they are then accelerated with an extraction voltage of 25 kV (at which the ion source floats) in the direction of an analyser magnet. Electrons are also repelled back to the filament by the negative bias.

The extraction electrode has a negative bias, which causes positive ions to be extracted from the ion source and accelerated to energies of around 20 keV. However, some of these ions collide with the extraction electrode surface, producing X-rays and secondary electrons. To increase the probability of plasma ionization and the creation of positive ions, an electron reflector electrode is used to send electrons back into the source. The ion beam is produced as ions flow out through a small slit in the electrodes as a stream of ion flux [50].

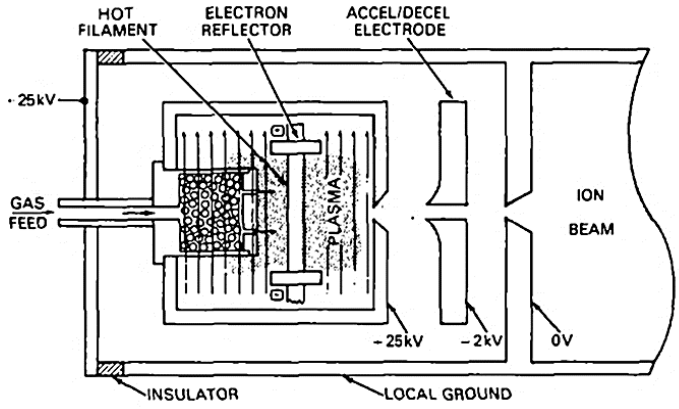

Figure 4.7: Schematic drawing of Freeman-type ion source [50].

4.3.1.2 MASS ANALYSER

When ions move through a magnetic field (***B***), they encounter a force that is perpendicular to both their velocity (***v***) and the magnetic field. This force causes the ions to follow a curved path, and the radius of this path (***R***) can be calculated using Equation 4.1 that takes into account the mass (***m***) and charge (***q***) of the ions.

$$R = \frac{mv}{qB} \qquad \textbf{4.1}$$

Only selected ions with the proper radius of curvature can pass through the acceleration column by changing the magnetic field. Ions with a high/small mass to charge ratio (***m/q***) will not pass through the beam path when angled at 90°, Figure 4.8 [51].

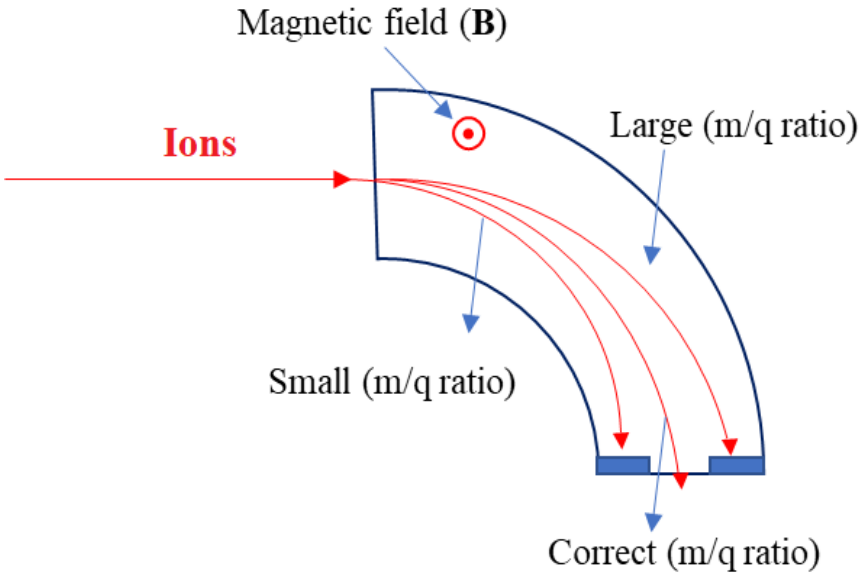

Figure 4.8: Schematic diagram of Mass Analyzer.

4.3.1.3 ACCELERATION TUBE

After being mass analyzed, the ions are directed towards the acceleration column. Inside this column, the ions are given a final kinetic energy by the extraction electrode potential (V_{ext}) and the acceleration electrode potential (V_{acc}) which are located within it. The final kinetic energy of the ions depends on these potentials. In order to increase the kinetic energy of ions for high-energy ion implantation, several acceleration electrodes are arranged in a series along the beam line. This arrangement allows the ions to acquire energy levels as high as 150 keV. On the other hand, for shallow ion implantation, the acceleration electrode is reversed which results in a low-energy ion beam [52].

4.3.1.4 BEAM MANIPULATION SYSTEMS

Electrostatic and magnetic fields are employed in these systems to achieve a homogeneous surface implantation of the target sample and to steer the ion beam towards the desired target location. Following acceleration, an electrostatic quadrupole triplet lens is used to concentrate the beam by applying transverse forces to maintain a small beam radius around the primary beam axis. Due to the rapid expansion induced by its space charge, the ion beam changes its shape. This happens because the ions remain in close proximity to each other for a longer time period during low energy propagation, leading to strong repulsion between the ions in the beam. This repulsion causes the beam shape to deviate from the primary axis and spread out. During the beam transportation and resolution process, any secondary charged particles are eliminated from the beam transport system using quadrupoles with fields of opposite polarity. Positively charged particles are captured by negatively biased electrodes, whereas negatively charged particles are captured by positively charged electrodes [53].

The ion implanter includes beam deflection plates that function similarly to the beam focusing system in removing negative polarity secondary ions and electrons from the beamline. The neutralization effect, which results from collisions between a positively charged beam and neutral gas particles, typically leads to ion-electron

pairs being produced in the beamline through ionization collisions. As a result, ionization usually occurs in the beamline. However, this process only partially neutralizes the ion beam. The ion beam can be bent using electrostatic plates to remove undesired particles, including remaining neutral atoms, that are still present in the beamline and are being propelled towards the target sample. Neutrals are undesirable because they are not deflected by the scanner plates and can generate a "hot spot" with additional fluence in the centre of the target sample. To solve the issue, a solution involves using parallel electrostatic plates that deflect ions towards the target sample while leaving neutrals undisturbed. This feature can be combined with a single pair of scanner plates. The scanner plates are positioned along the x- and y-axes with opposite potentials, creating an electromagnetic field (E) between them. When charged particles pass through the plates, they experience perpendicular forces due to the electric fields. As a result of this, the necessary ions are diverted. Since neutral atoms are untouched by electric fields, they will simply pass between the plates without being diverted. The ion beam is moved across the surface of the specimen using the x-y scan plates, Figure 4.9 [53][54], producing a spatially uniform implant.

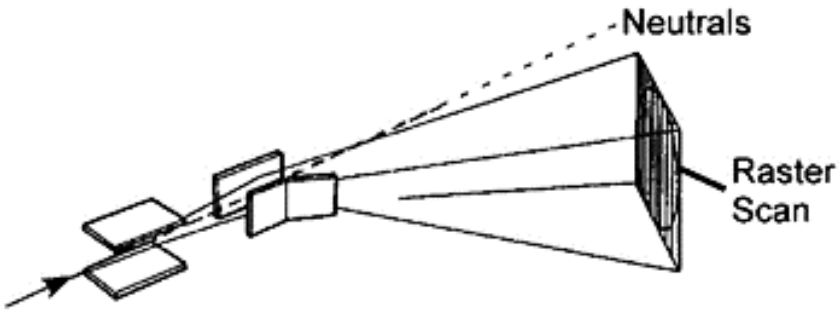

Figure 4.9: X-Y electrostatic scan system with dc deflection to avoid neutral atoms [54].

4.3.1.5 END STATION

The ion implantation procedure is carried out at the end station, is where the beam is directed once it has been scanned. The samples that will be implanted are positioned on a target holder in the end station. As a result of the stopping mechanism, the implantation process frequently results in significant phonon production, which raises the target sample's temperature significantly and necessitates an active cooling equipment. To keep the implantation temperature at a certain level, the active temperature control system uses a heater and liquid nitrogen. Additionally, the end station measures implant fluence and reduces fluence error. Faraday cups are used for this implant fluence control, which repels secondary electrons to prevent the current multiplication effect. A Faraday cup, which is an insulated block, is utilized to measure the charge of a stream of ions. If the energy of the ions that enter the cup exceeds the work function of the material, secondary electrons are generated (e.g., stainless steel, carbon, graphite). The problem is that the charge on the cup appears to have increased by one additional positive ion when a secondary electron leaves the cup. This issue can be overcome to by applying a ring at the entrance to the Faraday cup with a negative bias potential [40]. In this system there are four Faraday cups surrounding the target.

4.4 CHARACTERIZATION METHODS

The characterization of the samples was carried out before and after implantation using Raman spectroscopy, grazing incident X-ray diffraction (GIXRD), and scanning electron microscopy (SEM).

4.4.1 RAMAN SPECTROSCOPY PRINCIPLES AND INSTRUMENTATION

The method known as Raman spectroscopy was discovered by C.V. Raman, who also co-authored the first publication on it with K.S. Krishnan [55]. It is technique based on the inelastic scattering of incoming light by vibrational molecules. It measures molecular vibrations. Raman spectroscopy involves illuminating a sample with a monochromatic laser beam, which interacts with the molecules in the sample and produces scattered light. It is based on the *Raman effect*, which states that the frequency of a small fraction of scattered radiation varies from the frequency of monochromatic incoming light. Material inhomogeneities, such as molecular vibrations and imperfection, cause scattering. A photon scatters off a phonon (lattice vibration).

4.4.1.1 RAMAN EFFECT

The process whereby electrons relax after absorbing incident radiation and release a photon is coined photoluminescence. Rayleigh scattering occurs when an excited electron releases its energy and returns to the initial vibrational state. This occurs when the frequency of the scattered radiation is identical to the frequency of the original radiation. The amount of light that is inelastically scattered is significantly lower, often around 10^{-7}. This type of scattering is called the Raman effect, which involves a change in energy ($\boldsymbol{E_{inc}}$) of the incident light radiation and the energy of the Raman scattered light, known as the Raman shift. The Raman shift is required to change the vibrational state of a molecule from $\boldsymbol{v_i}$ to $\boldsymbol{v_j}$. In other words, the interaction

between photons of light and the phonons (vibrations and rotations of the molecules) in the sample causes the incident light's frequency to change [56].

4.4.1.2 RAMAN EFFECT: CLASSICAL APPROACH

Lattice dynamics are primarily involved in Raman scattering. There are two ways to approach it: classically or quantum mechanically.

The traditional explanation for the Raman effect is that it arises due to the interaction between the dipole moments of molecules in the sample being illuminated by incoming electromagnetic radiation. If a polarizable molecule is subjected to electromagnetic radiation, both the oscillating electric and magnetic field components of the radiation can interact with the molecule, but the magnetic component has a minimal effect on the molecule's dipole moment, its equilibrium electronic distribution changes, resulting in the formation of induced dipoles around the molecule. If these induced dipoles undergo normal molecular vibration in response to the external electric field, they can produce radiation. Raman spectroscopy is used to induce molecular vibrations and collect data on the bonding environment of the molecules in a material. The classical mechanics approach of this phenomenon is explained in detail in the literature [57].

4.4.1.3 RAMAN EFFECT: QUANTUM APPROACH

The fundamental principle of the Raman effect involves an interaction between the photon and the phonon in a material. Phonons can exhibit different modes, such as rotational, vibrational, or a combination of both [58]. This principle is based on the quantization of the electronic, vibrational, and rotational states of a molecule. The process involves a direct transition from state $\boldsymbol{n}$ to the virtual state, and relaxation back to the same state, resulting in Rayleigh scattering. On the other hand, the direct transition from one vibrational (or rotational) state $\boldsymbol{v_n}$ to another $\boldsymbol{v_n}\pm1$ results in an infrared (IR) spectrum. Raman scattering results in scattered radiation with a frequency different from that of the incident radiation. Within Raman scattering,

there are two processes known as Stokes scattering and anti-Stokes scattering. Stokes scattering is a process in which an electron in the ground vibrational state is excited to a virtual state and then relaxes to a higher energy level than the ground state. Anti-Stokes scattering, on the other hand, involves the excitation of an electron to a virtual state, followed by relaxation to the ground state with less energy than initially had, Figure 4.10 [59]. This frequency change is referred to as inelastic scattering, and it is regulated by quantum mechanical selection rules.

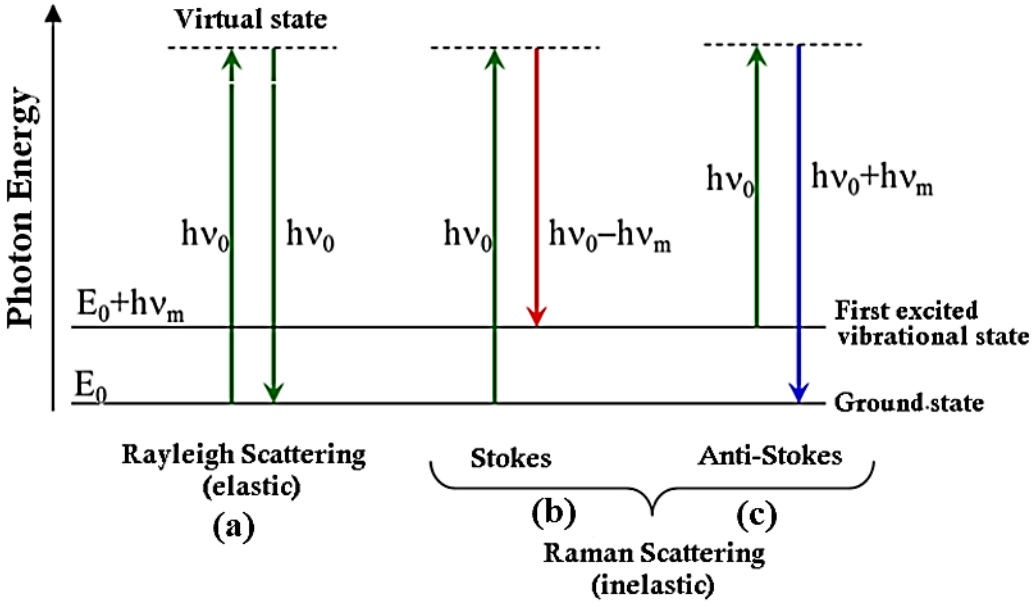

Figure 4.10: Energy level diagrams demonstrating how an excited atom undergoes different-energy photon release due to: (a) Rayleigh scattering, (b) Stokes Raman scattering, and (c) anti-Stokes Raman scattering. [59].

In the Raman scattering process, energy and momentum are conserved. If a photon with a frequency of w_i causes the creation or absorption of a phonon with a frequency of w_{ph} during the scattering process, a scattered photon with a frequency of w_s is produced. This is in accordance with the principle of conservation of energy:

$$\hbar w_i = \hbar w_s \pm \hbar w_{ph} \qquad \textbf{4.2}$$

The value of $\hbar$ is h divided by 2π, where h is Planck's constant.

$$q_i = q_s \pm q_{ph} \quad \textbf{4.3}$$

The wave vectors of the incoming photon, scattered photon, and emitted or absorbed phonon are denoted as q_i, q_s, and q_{ph}, respectively. The symbols '+' and '-' denote Stokes and anti-Stokes processes, respectively. At normal temperatures, the initial excited state is not highly populated, and according to Boltzmann statistics, anti-Stokes Raman scattering is less likely to occur. Anti-Stokes scattering generally produces a weaker Raman signal compared to Stokes scattering, as it involves the transfer of energy from the molecule to the incoming light photons [60].

4.4.1.4 INSTRUMENTATION

The Jobin-Yvon T64000 Raman spectrometer located at the University of the Witwatersrand's School of Physics was used for measurements, Figure 4.12. For Raman excitation, a strong coherent 514.5nm Argon (Ar^+) laser beam was utilized. However, since laser beams are not completely monochromatic, a laser transmission filter was employed to decrease the width of the incident beam. Nevertheless, recovering useful data from Raman scattered light can be challenging as it is very feeble and situated near Rayleigh scattered light, which is much brighter. Therefore, careful signal processing techniques must be implemented to extract the necessary data from the signal components. The spectrometer is a dispersive instrument with three monochromators. The filtered beam is focused onto the sample in a volume of approximately 1 μm^3 using an objective lens device. A holographic notch filter is put between the sample and the monochromators to eliminate unwanted light before the spectrometer recognizes and measures the Raman signal. Once the filtered light is received, the monochromators, which consist of dispersive devices with diffraction gratings, disperse the broadband signal into discrete spectral lines based on their wavelengths. The Jobin-Yvon T64000 spectrometer can maintain its resolution if operated in single spectrograph mode, as long as the Raman signal is

not located too close to the Rayleigh line. In the exit slit of the third monochromator, CCD detectors are installed to detect photons and convert them into digital signals. These data can be stored in a computer [56].

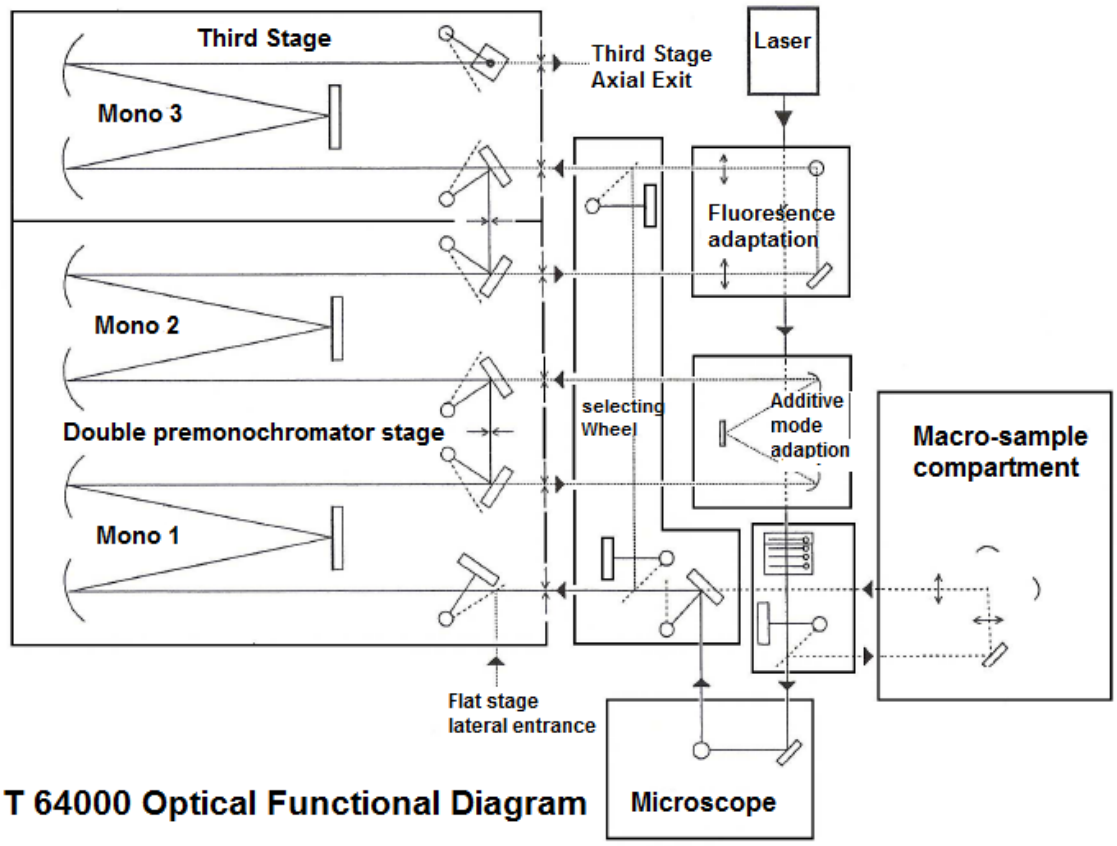

Figure 4.11: The Jobin-Yvon T64000 spectrometer design (provided by HORIBA Jobin Yvon Ltd., UK), which was used in this study.

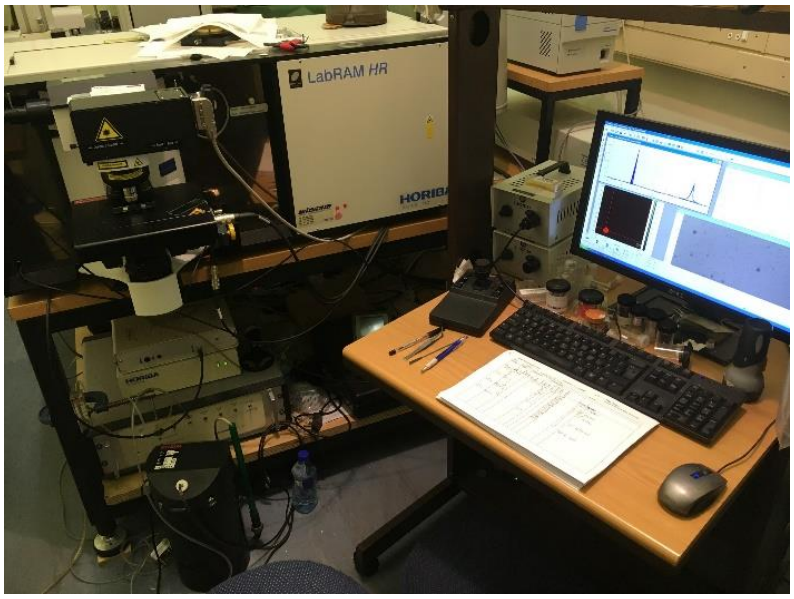

Figure 4.12: Instrumentation for the Jobin-Yvon T64000 Raman analyser spectrometer.

4.4.1.5 PROCEDURE

The Raman spectrometer is operated using a computer, and it can be used in either macro-Raman mode, which involves measuring large sample pieces in a macro compartment, or micro-Raman mode, where measurements are performed on a microscope stage. The laser light can be focused on the sample's surface to a diameter of 1 μm. The spectrometer can operate in 2-D mapping mode when measurements are taken on the X-Y microscope stage, and it can be used in 3-D mapping mode with the help of a piezo Z-stage scanner. In the experimental work discussed in this thesis, the micro-Raman mode was used.

In this study, ambient conditions were used for all of the Raman measurements. The 514 nm argon laser was used as the excitation source for the experiments, and the beam power was set at 200 mW. The equipment has a spectrometer that had a grating with 1800 grooves/mm and a CCD detector that was cooled with nitrogen. Using micro-Raman in single spectrograph mode, a virgin Si substrate was characterized

in the first round of Raman experiments. The output spectra were measured using a CCD detector that was cooled with liquid nitrogen and connected to a computer for data presentation, analysis, and storage.

Raman spectroscopy was carried out both before and after ion implantation. To ensure intensity accuracy and consistency, the spectrometer was calibrated using a silicon wafer (100) as a reference sample. It is anticipated that the typical optical vibration phonon modes of h-BN with space group $P6_3/mmc$ will be present at the Brillouin zone centre [61], represented by the following equation

$$\Gamma = 2B_{lg} + A_{2u} + E_{lu} + 2E_{2g} \qquad \textbf{4.4}$$

Equation 4.4 represents the optically inactive phonon mode, which is denoted as $2B_{lg}$, and is not observed in any optical vibrational spectrum. The in-plane B-N bending and out-of-plane B-N stretching of boron nitride, which correspond to A_{2u} and E_{lu}, respectively, and are infrared-active phonon vibrational modes, are not expected to be present in the visible Raman spectrum. The final component of the equation represents the Raman active mode (E_{2g}), which typically exhibits two vibrational centres. These symmetry centres are produced by the displacement of both boron and nitrogen atoms in both the in-plane and out-of-plane directions [62].

4.4.2 X-RAY DIFFRACTION (XRD) AND GRAZING INCIDENCE X-RAY DIFFRACTION (GIXRD)

The study of crystal structures and atomic spacing is done using the X-ray diffraction method. It is based on a cathode ray tube's monochromatic X-rays' constructive interference. These experiments were carried out using the D8 discover ADVANCE Bruker X-ray Diffractometer located at the University of the Witwatersrand's School of Chemistry, Figure 4.13. The diffractometer is outfitted with CuKα radiation with a wavelength of λ=1.5406 Å and is operated at a voltage of 40 kV with a current of 40 mA. Measurements were made on the CVD prepared Si-samples both before and after implantation.

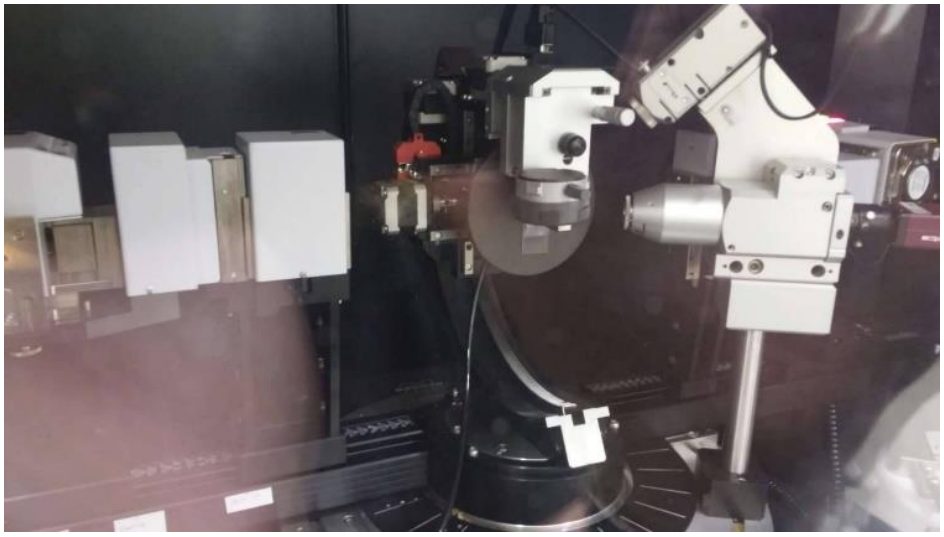

Figure 4.13: D8 discover ADVANCE Bruker X-ray Diffractometer.

4.4.2.1 PRINCIPLES OF X-RAY DIFFRACTION

When an electric current is passed through a tungsten filament cathode, it heats up and releases electrons. Under high vacuum these electrons are then accelerated towards a metal target anode, typically made of copper or molybdenum. When these electrons collide with the target metal, they transfer energy to electrons in the metal atoms, knocking them out of their usual positions and creating vacancies in the innermost electron shells. Electrons from outer shells can then fall into these vacancies and release energy in the form of X-rays with specific energies, known as characteristic X-rays. The two most common types of characteristic X-rays are K_α and K_β rays, which are emitted when outer-shell electrons fall into vacancies in the innermost electron shell of the metal atoms. The energy released in this process is unique to each element, making characteristic X-rays a powerful tool for analysing the elemental composition of a sample, Figure 4.16. The K_αCu X-rays have wavelengths of ~0.15nm and K_β ~0.13nm. The reason why X-rays of the wavelength ~0.15 nm are needed and ~0.13nm X-rays are filtered is to see clearly the interference patterns observed at the specific diffracting angles for the crystal; K_αX-rays have much higher intensity and would a very good signal to noise. When incoming electrons are redirected back from the core level, they lose energy and produce both single frequency (characteristic) and a broad spectrum (Bremsstrahlung) X-rays. Bremsstrahlung X rays have a wide spectrum, and after being removed by a filter, the sample is exposed to monochromatic X-rays instead. When X-rays interact with a sample and satisfy Bragg's law, they will be in phase and undergo constructive interference and this will lead to the reinforcement of the scattered X-rays and an overall increase in the intensity at specific angles, resulting in diffracted X-rays. By rotating the sample through a range of angles and measuring the intensity of diffracted X-rays at each angle, a diffraction spectrum of the sample can be obtained. In an X-ray diffractometer, the sample is mounted on a rotating stage that can be tilted at an angle θ with respect to the incident X-ray beam, while the detector is positioned on an arm that can rotate at an angle of 2θ (the angle between the incident and reflected beam, Figure 4.15) to detect the diffracted X-rays. The detector measures the intensity of the diffracted X-rays, which is then converted to a count rate and output to a PC monitor for analysis Figure 4.14.

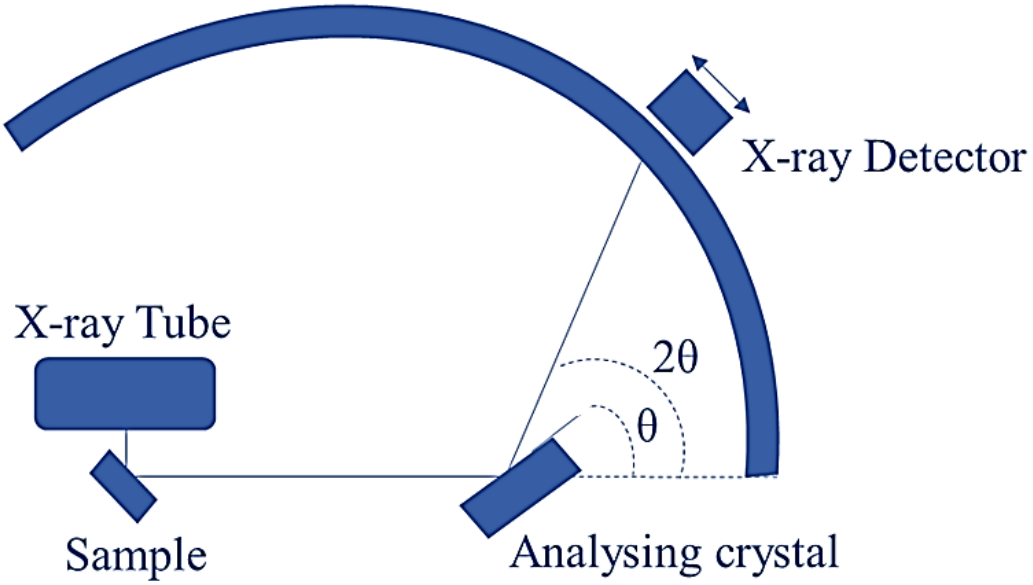

Figure 4.14: Schematic diagram of a diffractometer system.

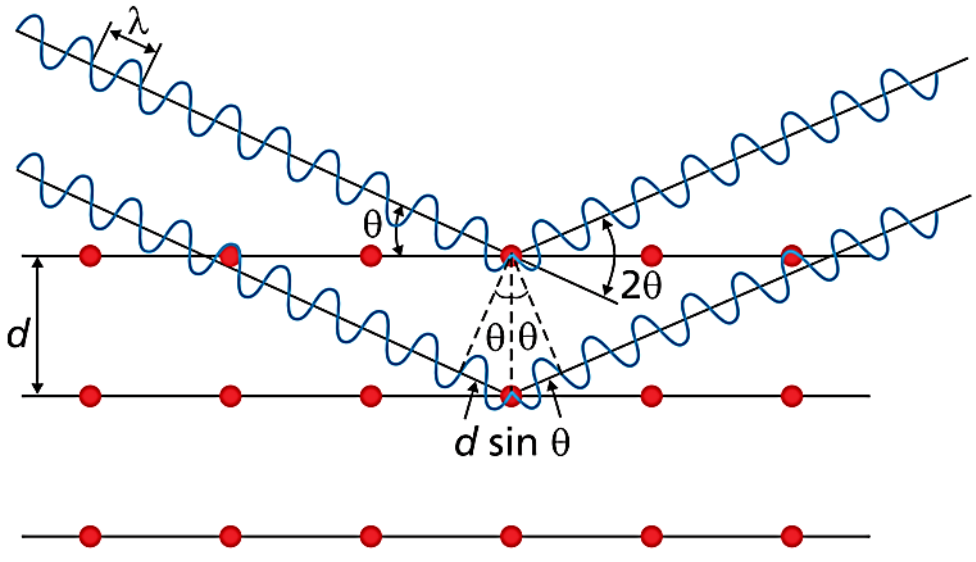

Figure 4.15: Diagram representation of Bragg's law [63].

The unique diffraction peaks of a material provide information about the atomic nanostructure, structure, and orientation of the crystallites. The *d*-spacing of the set of planes being scattered is defined by each peak, and the position, intensity, and width of the peaks can be analysed to determine these characteristics of the material [64]. Grazing incidence X-ray diffraction (GIXRD) was used in this thesis to analyse the crystal structure of the sample.

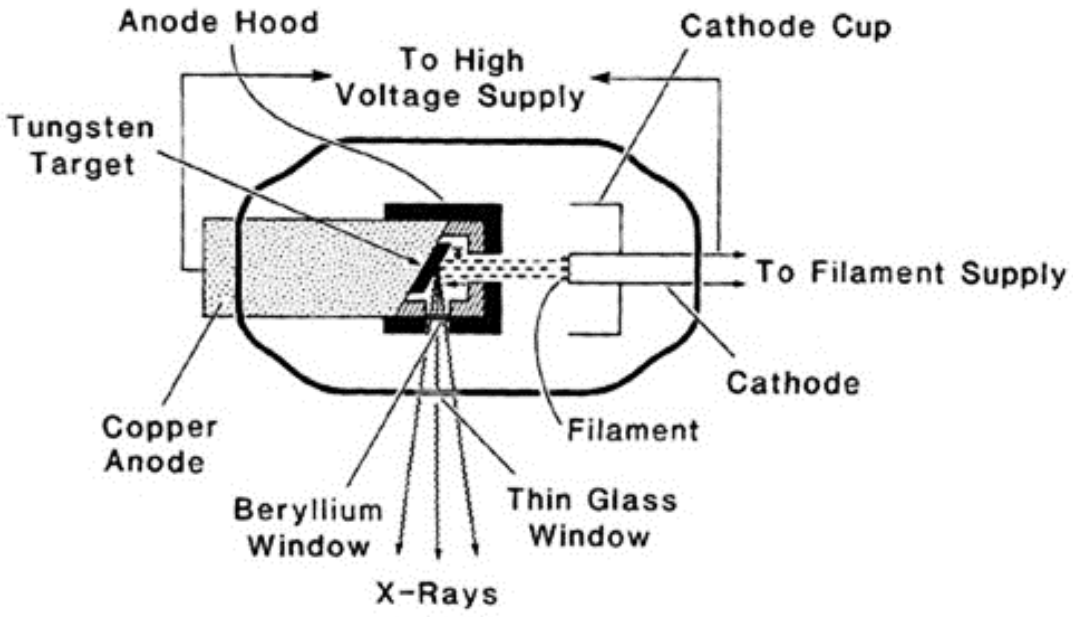

Figure 4.16: Schematic of diagram X-ray tube [65].

4.4.2.2 GRAZING INCIDENCE XRD

GIXRD is a method for analysing crystal surface structures, as opposed to traditional XRD, which gives information about a material's internal structure. The incident X-rays are directed at a very small angle ($\boldsymbol{\vartheta}$) to the sample surface, which is close to the critical angle for total external reflection, usually less than 1º depending on the solid material. When the angle of incidence ($\boldsymbol{\vartheta_i}$) is greater than the critical angle ($\boldsymbol{\vartheta_c}$), the reflected X-rays can reveal the subsurface information of the material ($\boldsymbol{\vartheta_i > \vartheta_c}$). Unlike in the $\boldsymbol{\theta}$ - $\boldsymbol{2\theta}$ scan configuration, when both the sample and the detector are in synchronous rotating motion, the sample remains stationary while the detector rotates across the $\boldsymbol{2\theta}$ angular range during the measurement of the GIXRD diffracted profile. The incidence angle and area under irradiation stay constant during the measurement [66].

GIXRD characterization was performed at a ϑ_i=1° incidence angle, and recording was done from 2ϑ =10° to 2ϑ=80° in increments of 0.1° for ~3 hours.

4.4.3 SCANNING ELECTRON MICROSCOPY (SEM)

The Scanning electron microscope (SEM) used is a ZEISS Sigma 300 VP located in the Chemical and Metallurgical Engineering, University of the Witwatersrand, Figure 4.17. It has a field emission gun, and the SEM software is ZEISS 'Smart SEM'. SEM was used in this work mainly to investigate the surface topography of the samples.

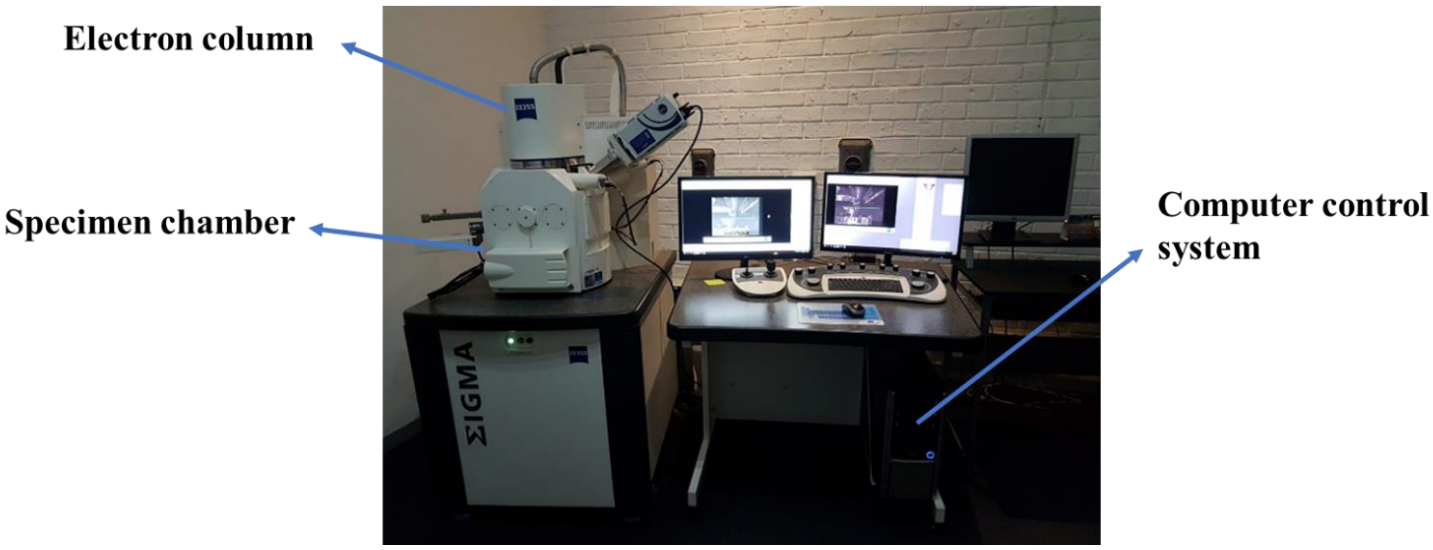

Figure 4.17: ZEISS Sigma 300 VP.

4.4.3.1 PRINCIPLES OF SCANNING ELECTRON MICROSCOPY (SEM)

The scanning electron microscopy (SEM), apparatus can be separated into three main components: the electron column, where electrons are accelerated, the specimen chamber, where the sample is placed, and the computer/electronic controls, Figure 4.17 [67]. The upper part of the electron column contains an electron gun that creates a beam of electrons. The beam is focused into a small diameter (few nanometres) probe by electromagnetic lenses positioned within the column. The scan coils in the column move the probe across the surface of the sample in the chamber at the end of the column. To facilitate electron beam generation and advancement, the electron gun, column, and specimen chamber are kept under vacuum.

SEM is a potent tool for material analysis. The fundamental idea is that an appropriate source, usually a tungsten filament or a field emission gun, produces an electron beam. Under high vacuum a narrow beam of electrons is created by accelerating these electrons at a high voltage (for example, 3kV-15 kV) and passing it through a set of electromagnetic lenses and apertures. Through the use of scan coils, the incident beam scans the specimen's surface. When accelerated electrons collide with a material, they may scatter elastically, inelastically, or, if the material is thin enough, they may not scatter at all. Elastic scattering occurs when an electron comes contact with the electrostatic potential of an atom's nucleus; there is no energy loss in this process only the position of the involved electrons is altered. Inelastic scattering refers to a process in which the incident electron loses some of its energy to the atom or specimen being studied. This energy is transferred to the bound electrons of the lattice, which become excited. This process can cause radiation damage to the object being studied. These excitations result in various signals, which reveal details about the structure of the material. The signals that occur as a result of electrons contacting the surface of the material, such as backscattered electrons, secondary electrons, and characteristic X-rays, are are collected and processed to obtain images and chemistry of the material surface [65].

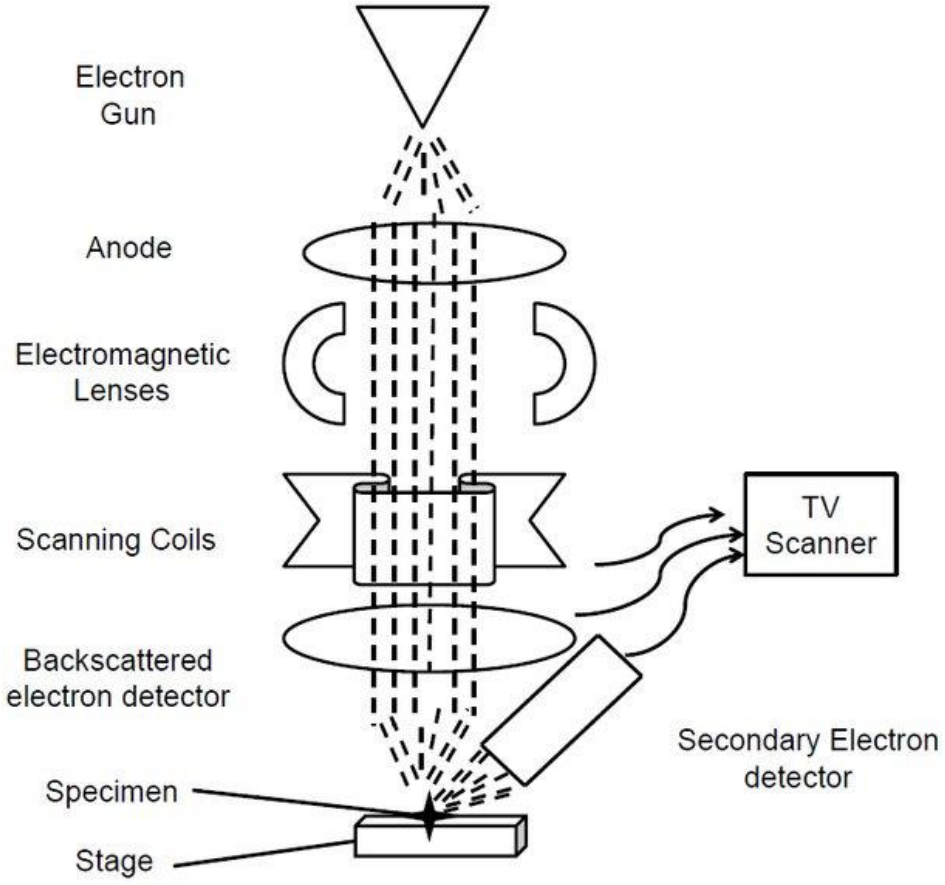

Figure 4.18: Schematic diagram of a scanning electron microscope [68].

CHAPTER 5

5 RESULTS

5.1 SIMULATION OF STOPPING AND RANGE OF IONS IN MATTER (SRIM)-2013

Figure 5.1 shows the SRIM simulations on the distribution of the number of vacancies per ion and unit length (Å) in h-BN, caused by the implantation of boron ions (B^+) at 150 keV. Notably, the curve shows that for boron ions at energy 150 keV, the range of ion penetration depth is ~0.4 μm. To calculate the damage density or vacancy concentration ***C(x)*** in the material, one needs to multiply the mean number of vacancies ($\boldsymbol{C_p}$) generated by the damage distribution for each ion per unit length by the fluence (***D***) over the total area, Equation 5.1. At 150 keV, the probability of nuclear stopping is expected to be low due to the relatively low atomic number of boron thus the stopping will be mostly electronic.

$$\boldsymbol{C(x) = C_p \times D} \qquad \textbf{5.1}$$

The calculation of the damage density concentration for boron ions was conducted based on the data obtained from the SRIM simulation. Therefore, for energy 150 keV at room temperature, at fluences of $1x10^{14}$ and $5x10^{14}$ ions/cm^2 **Table 5.1** has the vacancy concentration for boron:

Table 5.1: Displays the determined concentration of damage density in the material.

Ions	Optimum fluence (10^{14}ions/cm^2)	C_p(vac/10^{-8}cm-ion)	R_p(Å)	C(x)(10^{21}vac/cm^3)
Boron	1	2.75x10^{-2}	3.7x10^3	0.28
	5	2.75x10^{-2}	3.7x10^3	1.4

The term "optimum ion fluences" pertains to the specific fluence level that yielded the best results in terms of transforming the subsurface region of bulk h-BN into cubic BN [4][5].

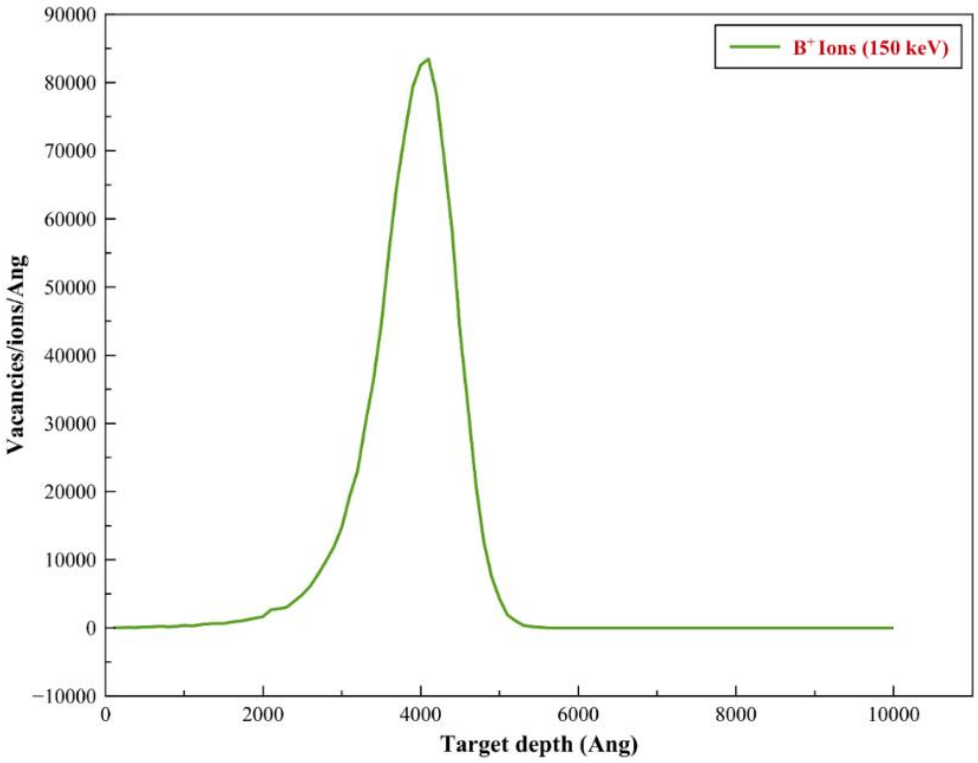

Figure 5.1: The graph generated by the SRIM model shows the relationship between the depth of penetration and the number of vacancies per ion and unit length (measured in Å) for boron ions at 150 keV.

5.2 SCANNING ELECTRON MICROSCOPY (SEM)

5.2.1 SAMPLES PREPARED AT 900°C

Figure 5.2 shows Boron nitride cauliflower like structures of the sample synthesised at 900 ºC for a growth duration of 1 hour, prior to ion implantation.

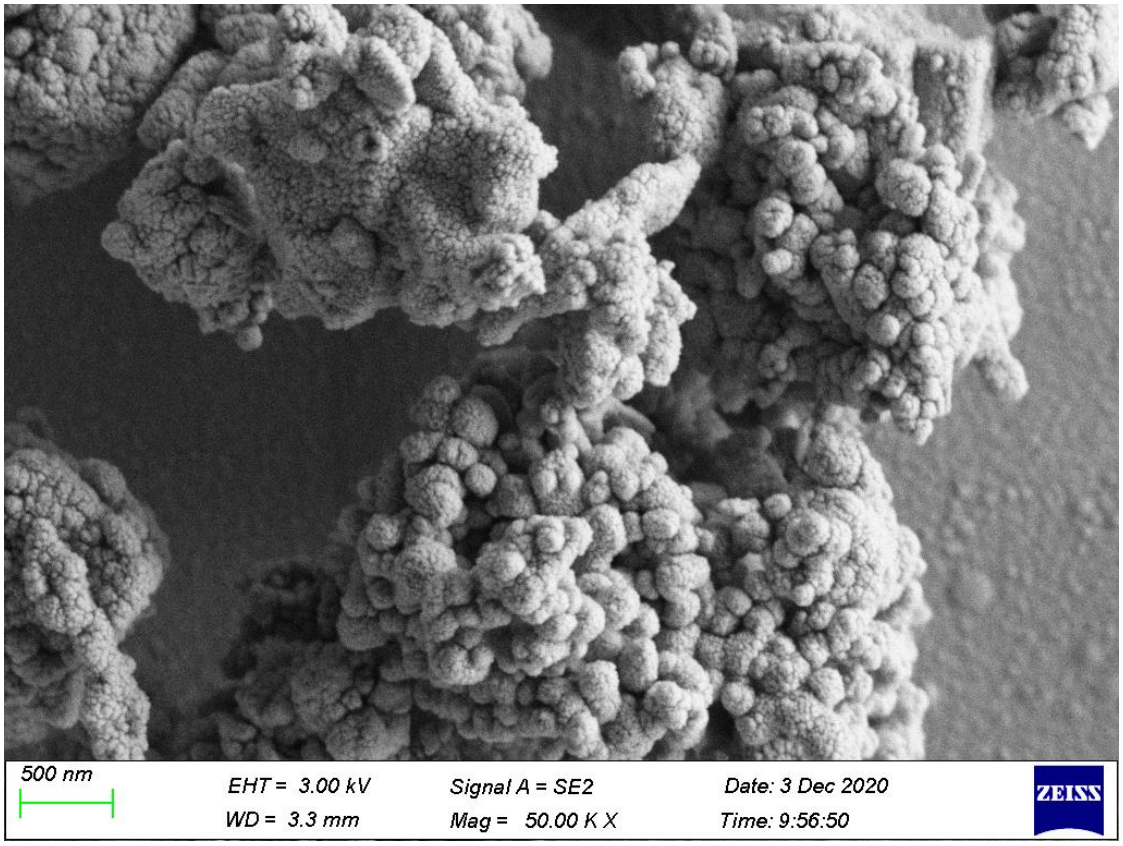

Figure 5.2: SEM image of synthesized boron nitride cauliflower-like nanocomposites, captured using secondary electron mode.

5.2.2 SAMPLES PREPARED AT 1000°C

Figure 5.3 shows the SEM image of BN nanostructures synthesized at 1000ºC prior to ion implantation. It is clear from the image that raising the temperature affects the phase transition of how the BN nanocomposites behave; there are some nanotubes (~50-80 nm diameter, indicated on the image) and a cauliflower-like nanostructure.

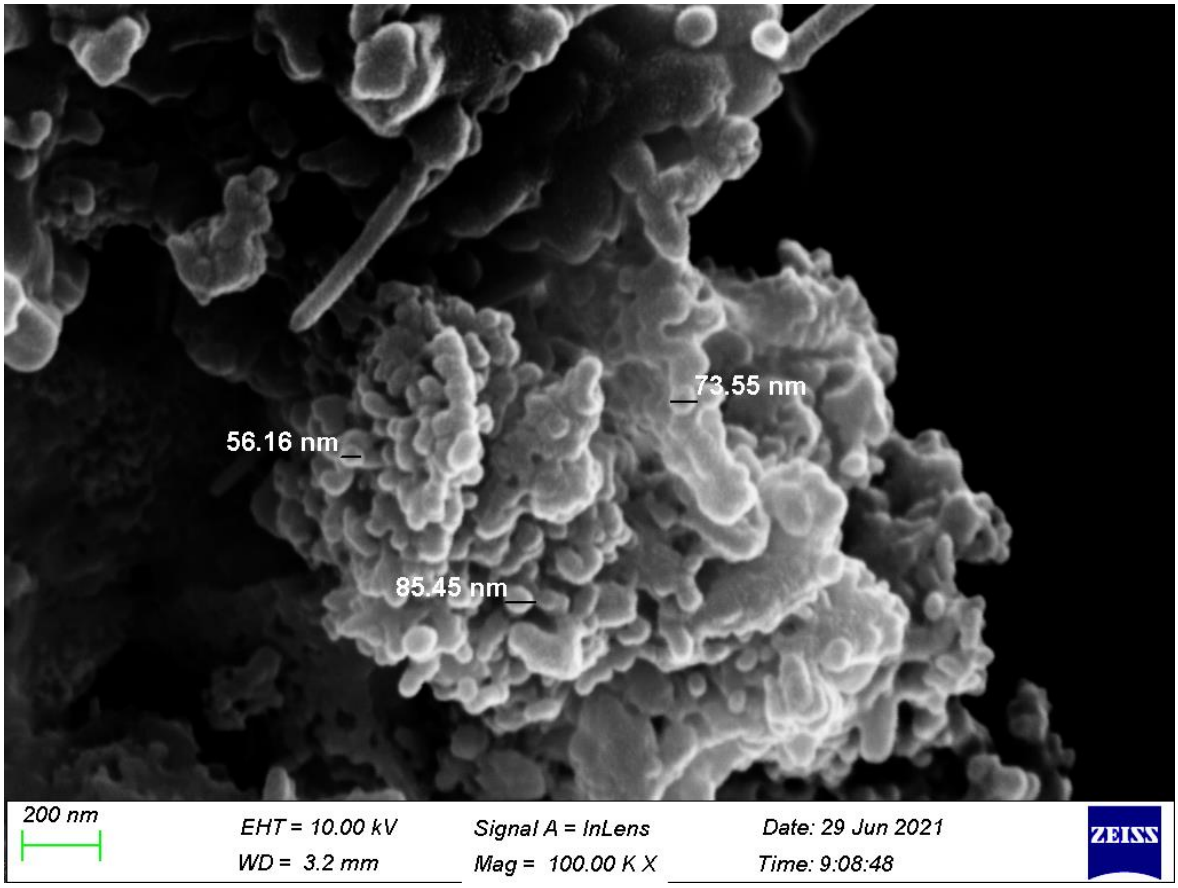

Figure 5.3: SEM micrograph of synthesized boron nitride nanocomposites at 1000ºC with the diameter of selected particles/composites/features indicated (diameter measurements indicated on image).

5.2.3 SAMPLES PREPARED AT 1100°C

The BNNTs synthesized at 1100°C prior to ion implantation are depicted in Figure 5.4. The tubes (~40-80nm diameter) show swollen tip characteristics that are found on many nanotubes.

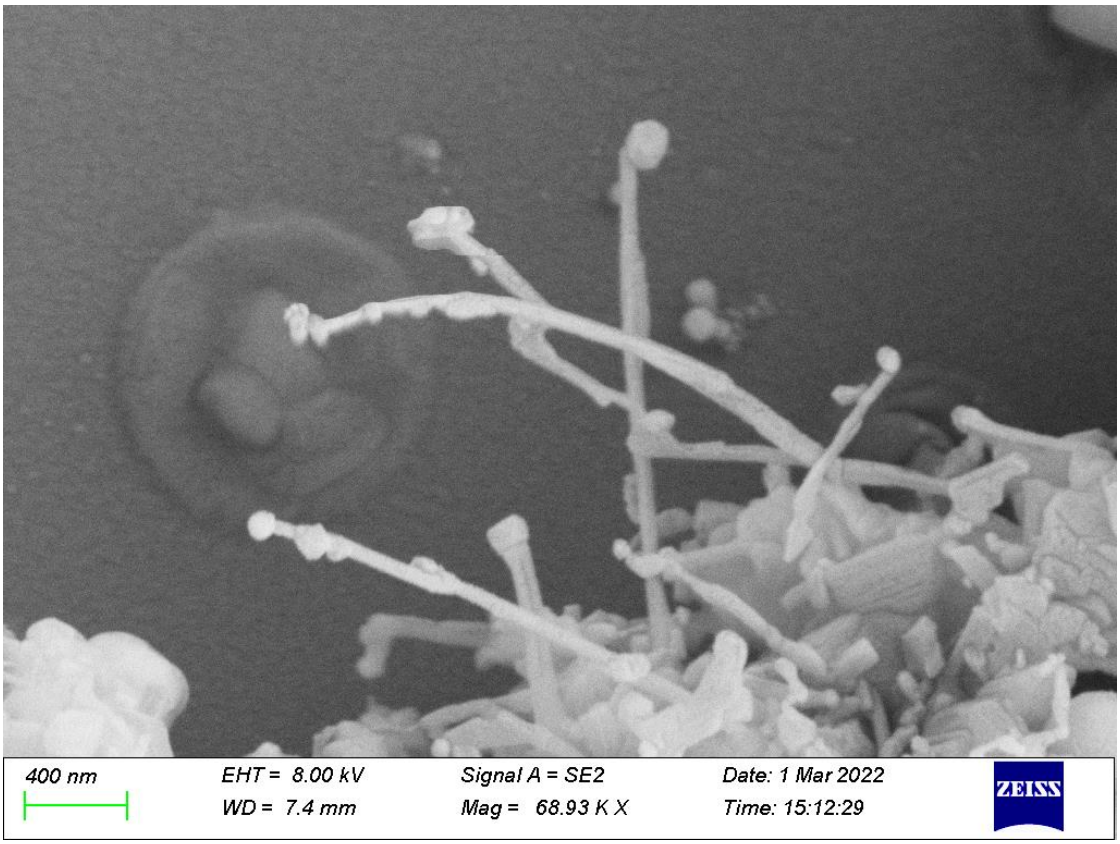

Figure 5.4: SEM image of boron nitride nanotubes (BNNTs) synthesized at 1100ºC, captured using secondary electron mode.

5.2.4 SAMPLES PREPARED AT 1200°C

The SEM images of samples synthesized at 1200 °C in Figure 5.5 (prior to implantation) show the presence of BN nanostructures at various magnifications. It is clear that various shapes of BN nanostructures were synthesized, cauliflower-like composites, nanospheres, and poly-dispersed nanotubes (~30-40nm) can be observed. Most of the latter have strong curvatures.

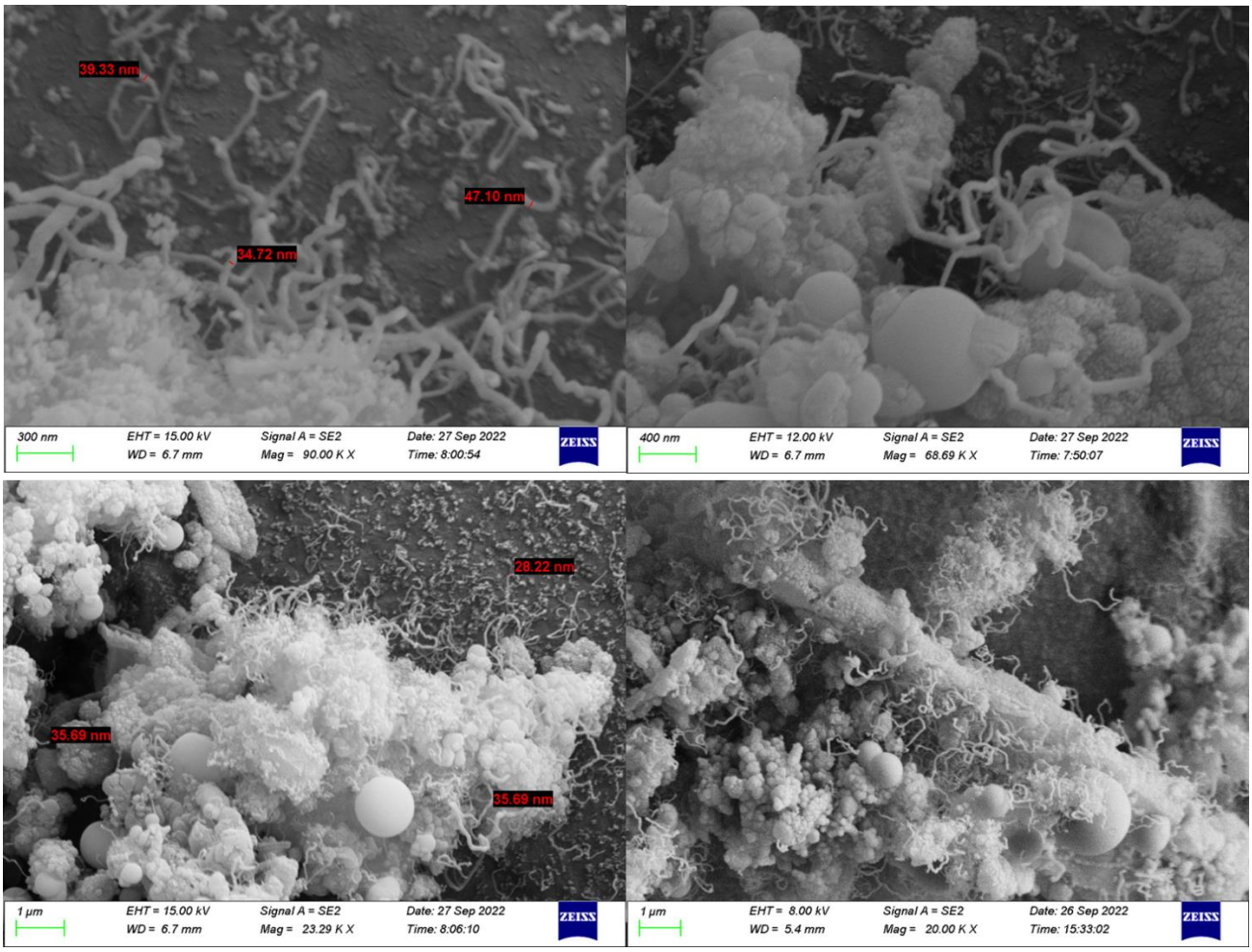

Figure 5.5: SEM images of sample synthesized at 1200 ºC, showing BN nanostructures of different shapes at different magnification, including many nanotubes, captured using secondary electron mode. The diameters of representative nanotubes are indicated in red.

5.3 GRAZING INCIDENCE XRD CHARACTERIZATION

The collected GIXRD patterns, both before and after ion implantation present a peak near 55.4° 2θ. This peak is consistent across the dataset, additional features are observed at lower angles, yet these are poorly defined above the background noise and are only observed for subsets of the patterns, Figure 5.6 to Figure 5.9. The data was compared to the literature structures COD 9008834 and COD 9008997 of cubic and hexagonal BN, respectively, from the Crystallography Open Database (Figure 8.2 in Appendix) [69].

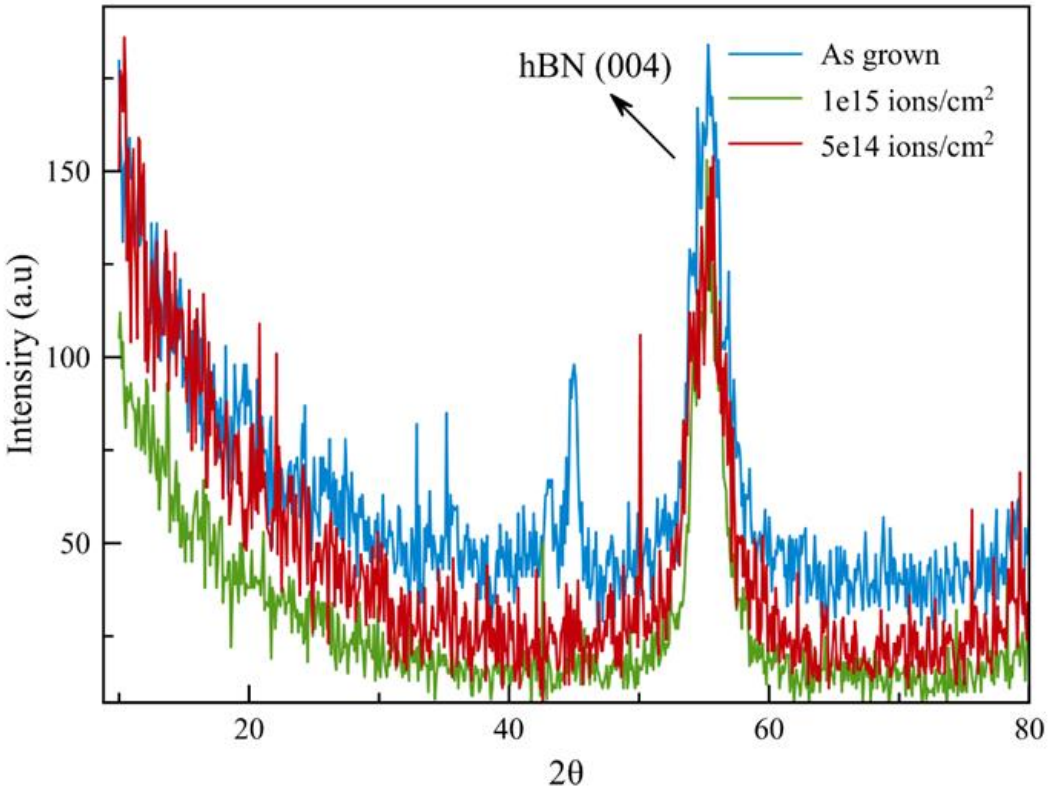

Figure 5.6: Grazing incidence XRD spectra of h-BN cauliflower like nanocomposites grown at 900 ºC.

The cubic structure offered no peaks comparable to the collected data, while the (004) peak from the hexagonal phase (h-BN) is consistent with the ~55.4° 2θ peak.

This peak cannot be attributed to the Si substrate, nor Si_3N_4, SiB_x, MgO, or Fe_xO_y phases which were considered due to the components used during synthesis.

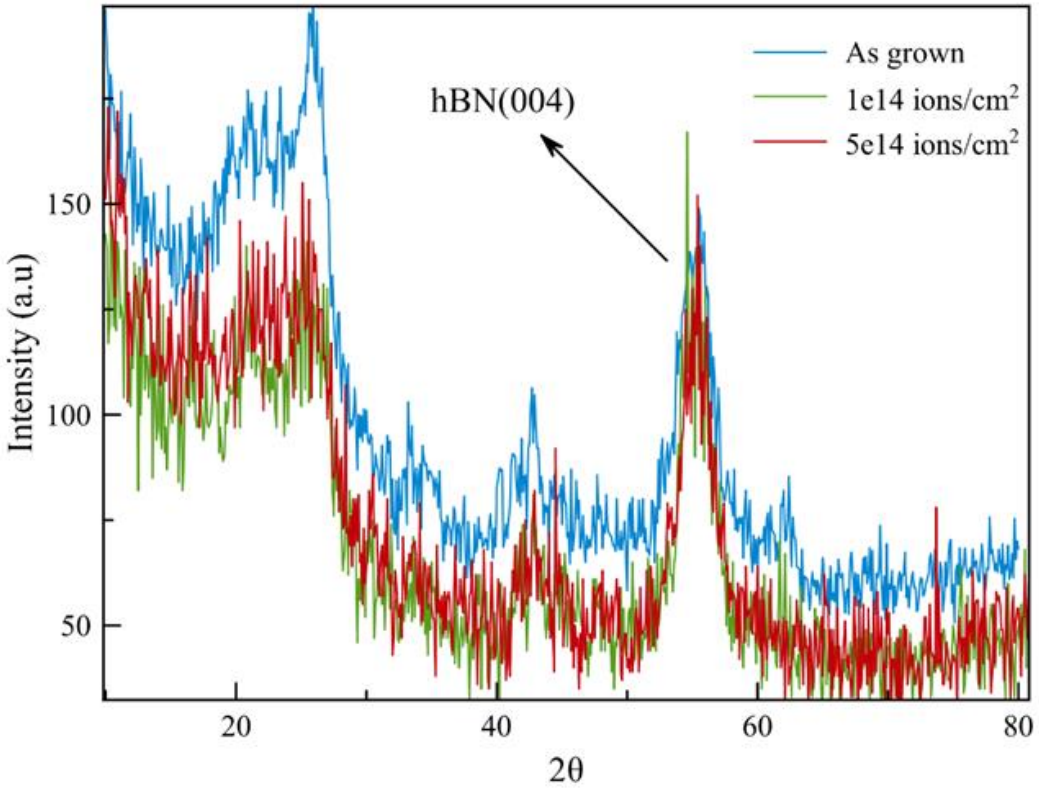

Figure 5.7: Grazing XRD spectra of h-BN nanostructures grown at 1000 ºC.

The absence of the full set of expected peaks could potentially be justified by a preferred crystallite growth orientation. In context of the (002) peak expected near ~26.7° 2θ, the scattering vector being probed by the GIXRD would be ~84 ° with respect to the surface, for the (004) peak this is ~77 °, in combination with a preferred orientation, this difference can potentially explain the absence of the (002) peak.

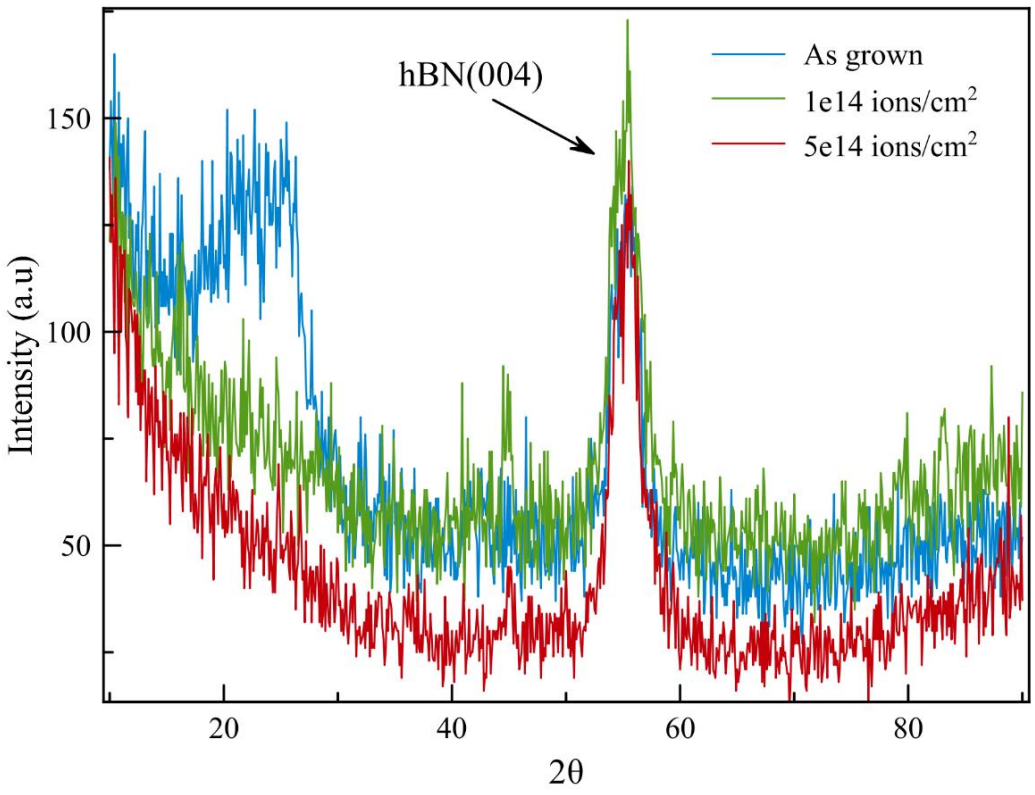

Figure 5.8: Grazing incidence XRD Spectra of BN nanotubes grown at 1100 ºC.

The possibility of preferred crystallite orientation cannot be taken for granted and thus warrants further investigation. Additionally, the formation of unidentified phases cannot be ruled out, this provides sufficient information to consider h-BN or a closely related structure as a possible source of the observed GIXRD peaks.

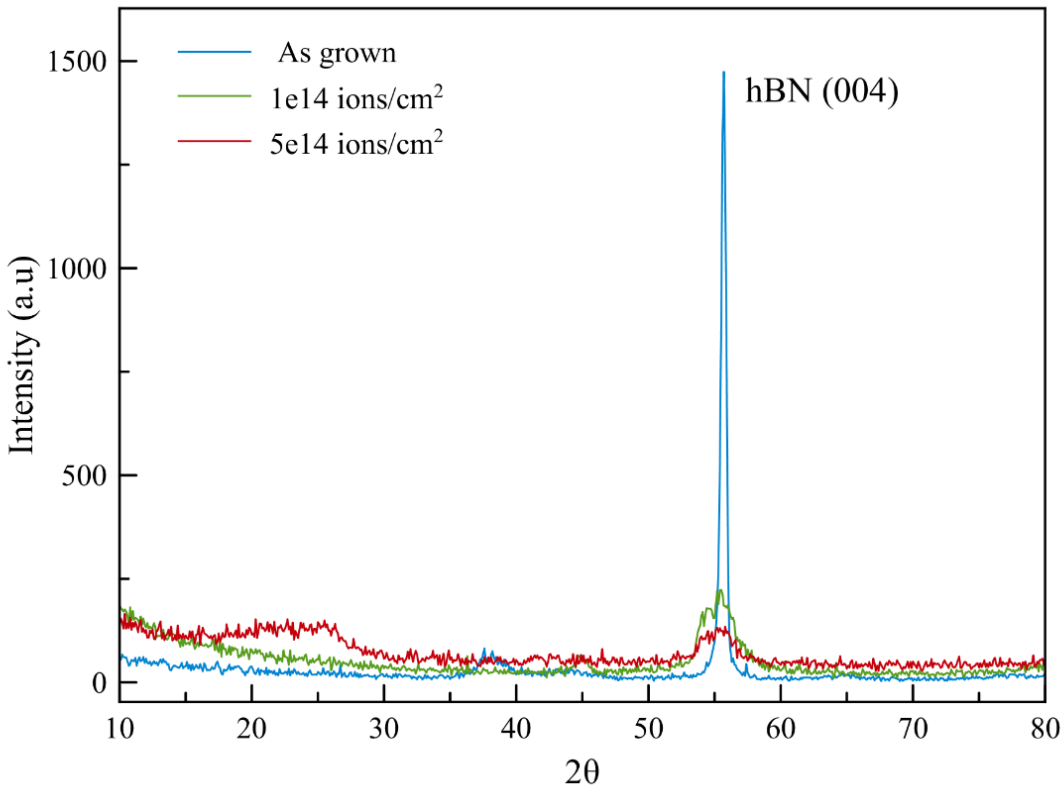

Figure 5.9: GIXRD spectra of CVD samples prepared at 1200 ºC.

5.4 RAMAN CHARACTERIZATION

The penetration depth of a particular wavelength of light into a material is defined as the depth at which the intensity (or power) of the electric field of the light has decayed to a value that corresponds to a fraction of 1/e of the incident light. Using this definition, laser penetration depth (***P***), is calculated by taking the inverse of the absorption coefficient ($\boldsymbol{\alpha}$), that is $\boldsymbol{P = \alpha^{-1}}$.

The absorption coefficient is calculated by using,

$$\boldsymbol{\alpha = \frac{4\pi k_e}{\lambda}} \qquad \textbf{5.2}$$

where $\boldsymbol{k_e}$ is the extinction coefficient (0.041 for *h*-BN) and $\boldsymbol{\lambda}$ is the photon's wavelength. For a 514.5nm laser (2.41 eV) and an h-BN sample, ***P*** is calculated to be approximately 1 μm. According to SRIM simulations in Figure 5.1, the range of implantation for boron at 150 keV is approximately 0.4μm. During the Raman spectroscopy measurements, the laser penetrates significantly deeper than the ion implantation range, thus ensuring that all potential implantation damage is sampled during the measurement.

Hexagonal BN has one intense Raman peak (E_{2g} mode) at 1366 cm^{-1} (see Figure 8.3 in Appendix). It is the typical B-N bond stretching vibration within the basal planes and it depicts the high frequency vibrational Raman mode [70]. The second Raman peak at 51.8 cm^{-1} is associated with the layer shearing vibration between the basal layers and is a low frequency mode [70][61].

5.4.1 RAMAN SPECTRA OF BN NANOCOMPOSITES

Figure 5.10 to Figure 5.12 is the Raman spectra of the samples before and after ion implantation.

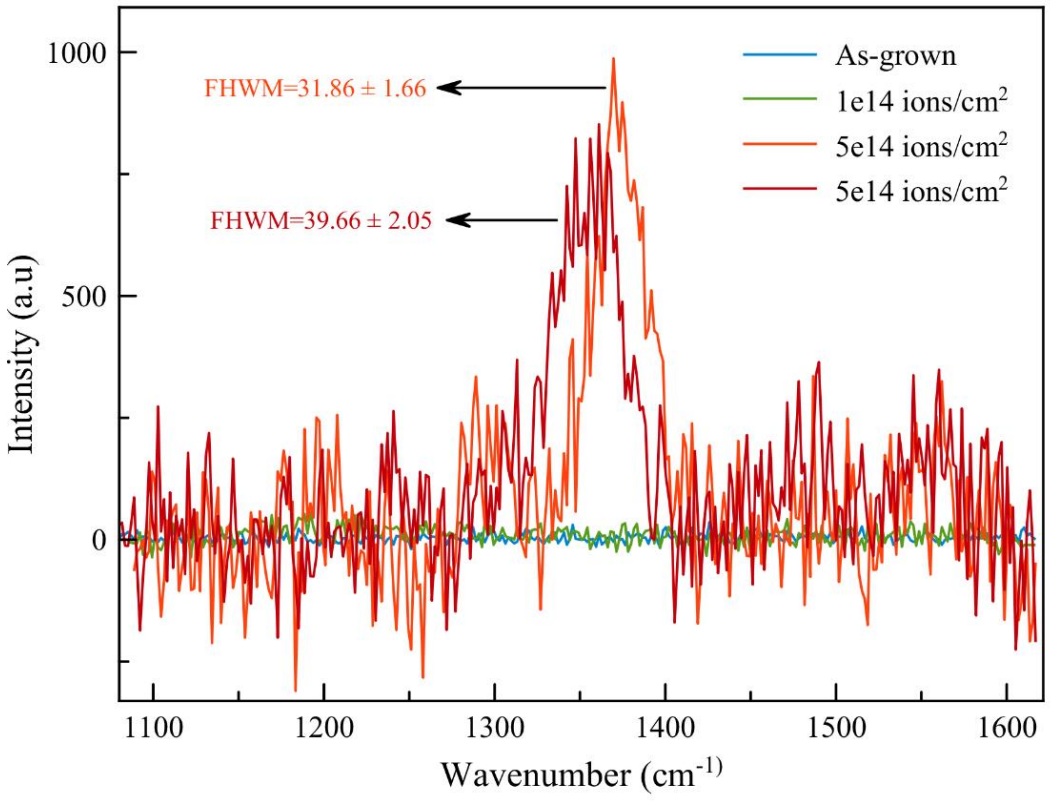

Figure 5.10: Raman Spectra of CVD prepared h-BN nanostructures at 1000 ºC.

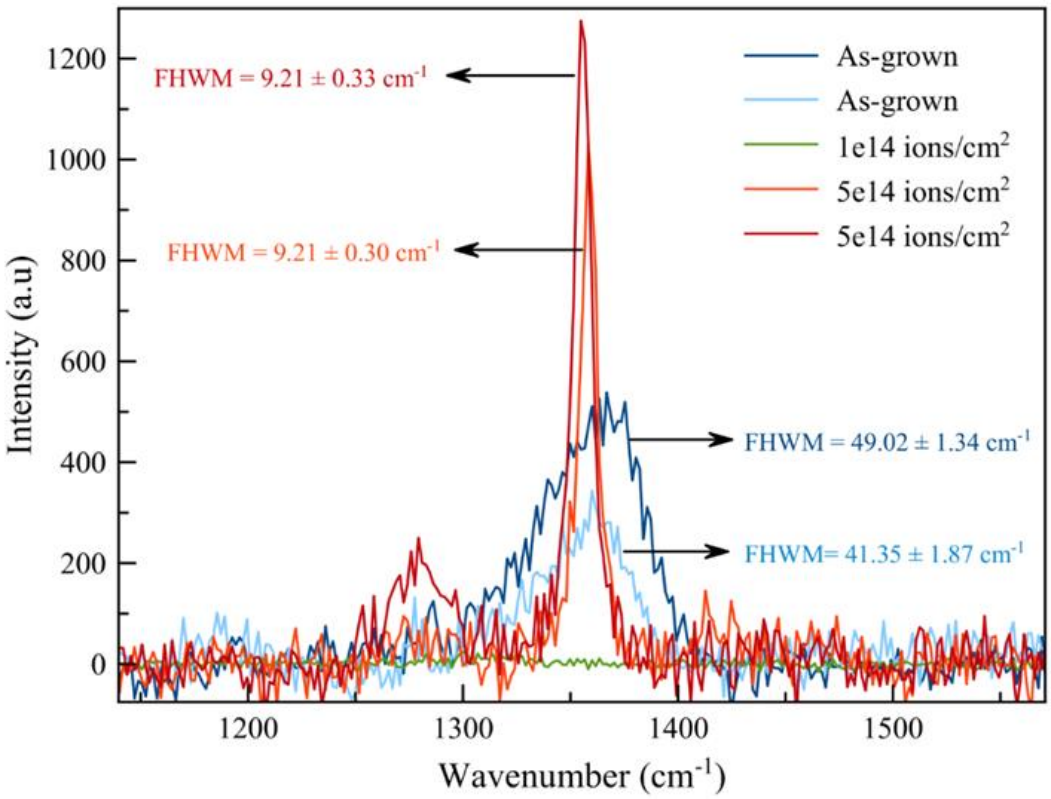

Figure 5.11: Raman Spectra of CVD prepared BNNTs at 1100 ºC, the two plots per ion fluence come from the two measured spots on the sample.

Before ion implantation, samples synthesized at 1000ºC did not show any peak in the vicinity of 1366 cm^{-1} (Figure 5.10), while sample synthesized at 1100ºC and 1200ºC showed a clear broad peak in the range 1350-1370 cm^{-1} (Figure 5.11 and Figure 5.12). This is attributed to the presence of amorphous h-BN in these samples.

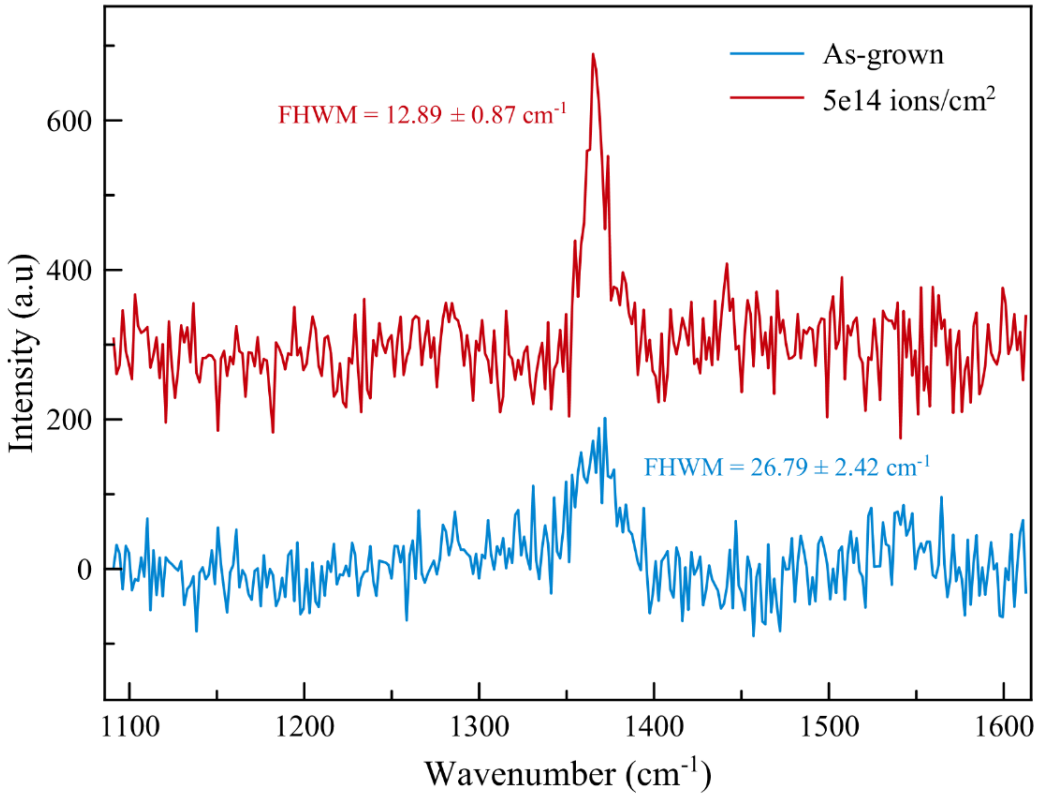

Figure 5.12: Raman Spectra of BN nanostructures prepared at 1200ºC.

After ion implantation, the Raman spectra of samples implanted with ion fluence 5×10^{14} ions/cm^2 at 1000ºC, Figure 5.10 show an amorphous h-BN peak, and a narrower, intense E_{2g} vibrational mode of h-BN is observed around 1366 cm^{-1} for samples synthesized at 1100ºC and 1200ºC, Figure 5.11 and Figure 5.12 respectively. Raman analysis did not show any E_{2g} mode of vibration of h-BN for all samples at implanted with ion fluence 1×10^{14} ions/cm^2. The samples synthesized at 900 ºC had no active 1366 cm^{-1} Raman peak present.

5.4.2 RAMAN MICROGRAPHS

Raman spectroscopy is a powerful technique used to investigate the structural and vibrational properties of materials. In this study, the Raman spectroscopy micrograph of samples before and after ion implantation is presented herein. The laser beam has a diameter of about 1 μm, and it is focused about 2-3 micron near to the (0,0) coordinate on the image. The images were mainly to show the particles that produced h-BN spectra.

5.4.2.1 VIRGIN SILICON SUBSTRATE

Figure 5.13 is the Raman spectroscopy micrograph of a Si (001) substrate, before CVD and ion implantation. The surface is clean in the sense that there is nothing deposited on it, but it has some dust particles.

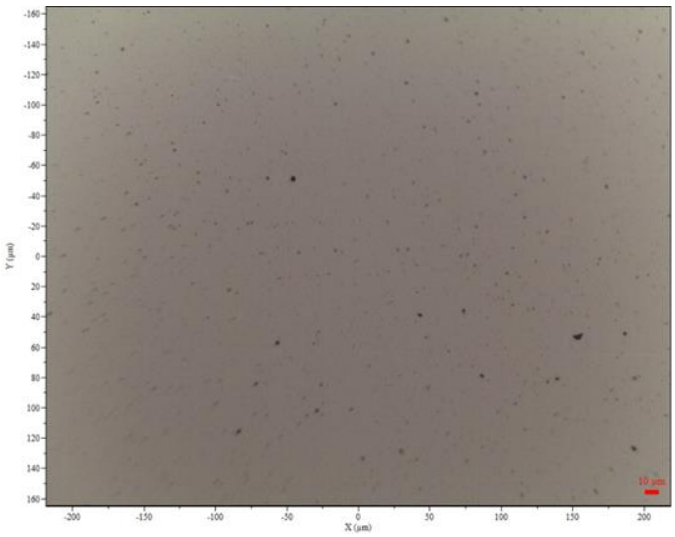

Figure 5.13: Raman spectroscopy micrograph of Si-Substrate.

5.4.2.2 SAMPLES BEFORE AND AFTER ION IMPLANTATION

The Raman spectroscopy micrograph of the samples for both before and after ion implantation are shown in Figure 5.14 to Figure 5.17. The images of the samples surface have dark regions that could be clusters of BN nanostructures formed during CVD deposition. The samples are different after ion implantation and there is an obvious surface colour change.

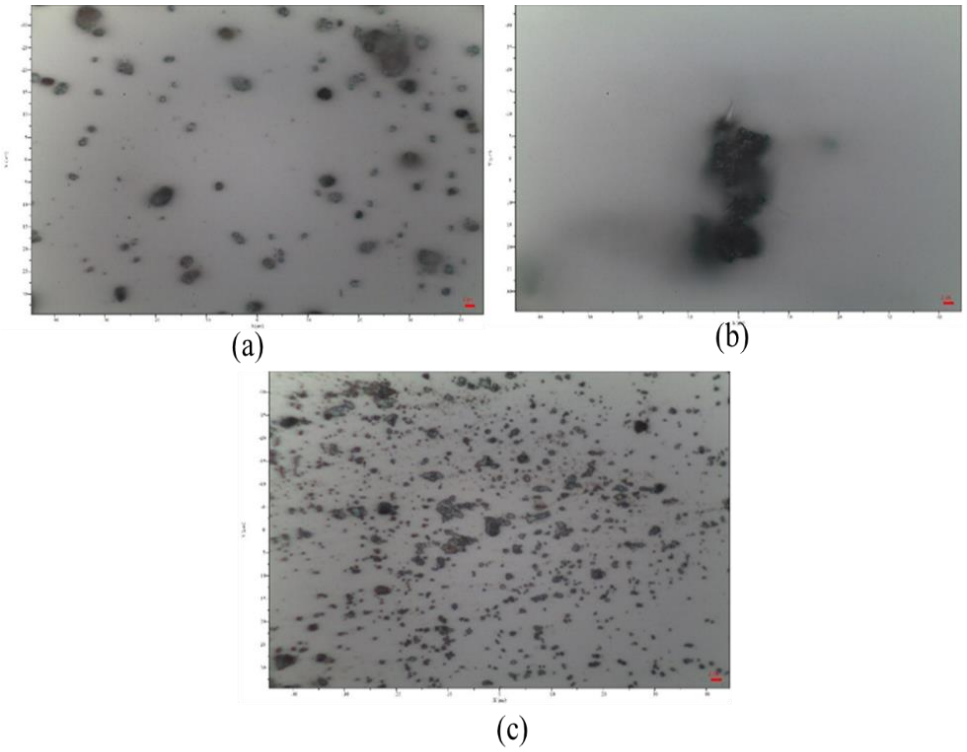

Figure 5.14: Raman spectroscopy micrograph of samples prepared at 900°C CVD temperature (a) without ion implantation, (b) Sample implanted with 1×10^{14} ions/cm^2 (c) Sample implanted with 5×10^{14} ions/cm^2.

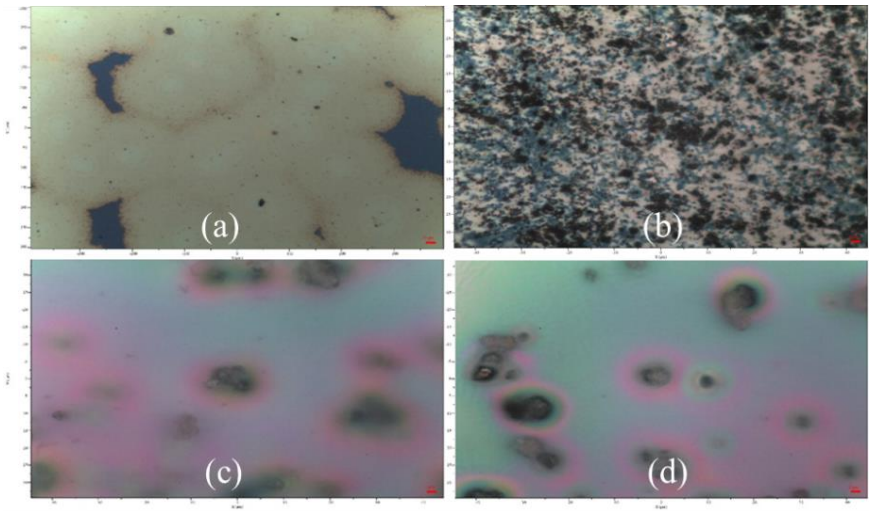

Figure 5.15: Raman spectroscopy micrograph of samples prepared at 1000 °C CVD temperature, (a) As-grown sample, (b) Sample implanted with 1×10^{14} ions/cm^2, (c) &(d) Sample implanted with 5×10^{14} ions/cm^2.

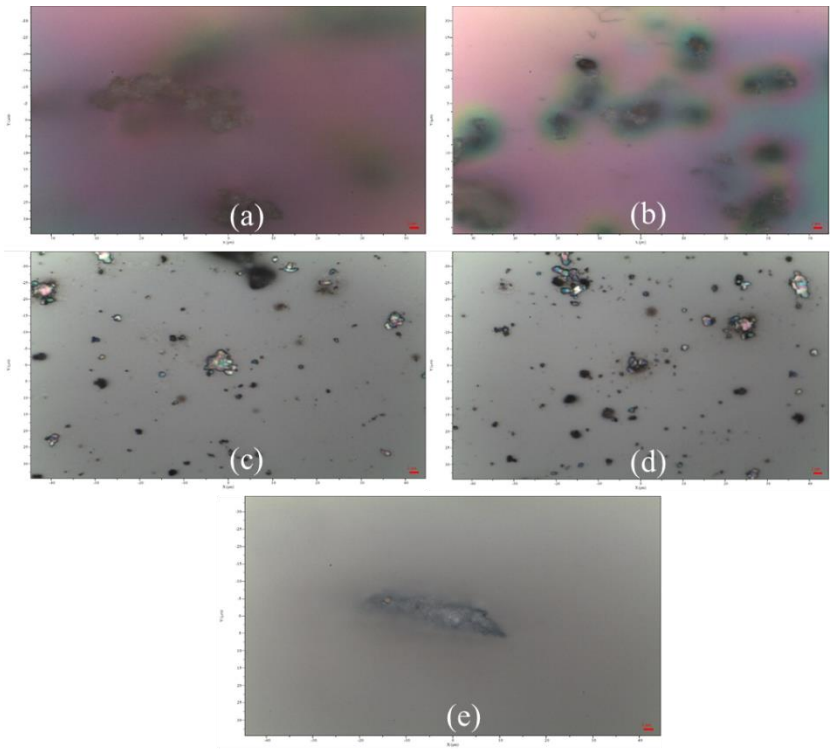

Figure 5.16: Raman spectroscopy micrograph of samples prepared at 1100 °C CVD temperature, (a) & (b) As-grown samples, (c)&(d) Sample implanted with 5×10^{14} ions/cm^2, (e) Sample implanted with 1×10^{14} ions/cm^2.

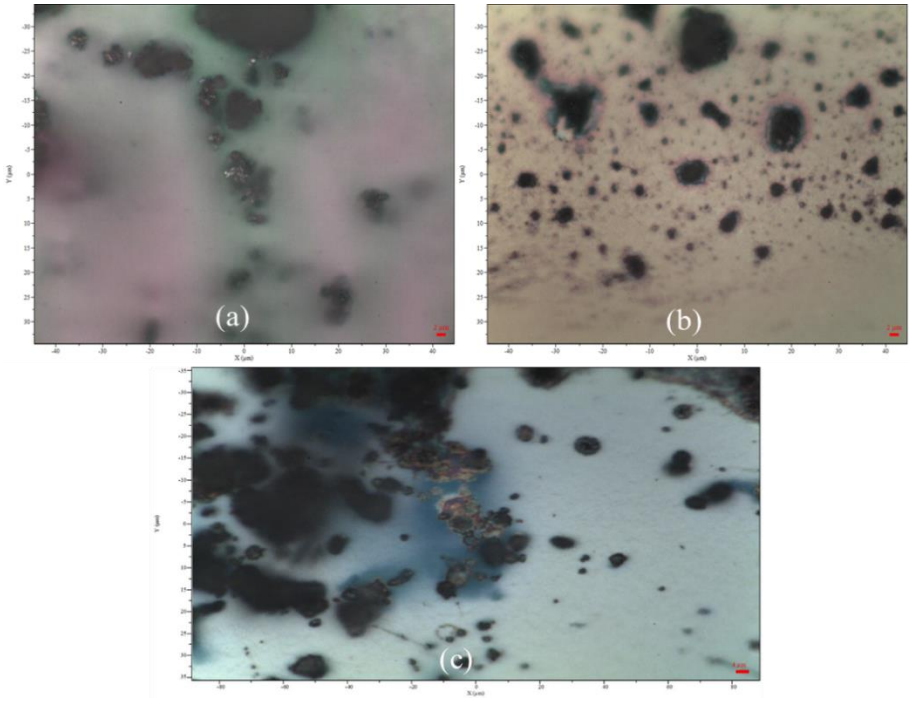

Figure 5.17: Raman spectroscopy micrograph of samples prepared at 1200 C CVD temperature, (a) As-grown samples, (b) Sample implanted with 1×10^{14} ions/ cm^2. (c) Sample implanted with 5×10^{14} ions/cm^2.

CHAPTER 6

6 DISCUSSION

6.1 GROWTH MECHANISM OF BORON NITRIDE NANOSTRUCTURES

The formation of boron nitride nanostructures, especially nanotubes (Figure 5.2 to Figure 5.5) using the chemical vapour deposition method, can be explained by the theory of nucleation [22][71]. The probability of nucleation is given by

$$P_N = Bexp^{\left(-\frac{\pi\sigma^2}{k^2T^2 \ln \alpha}\right)} \quad \textbf{6.1}$$

Where B (a constant), σ (surface energy), and α_s (the supersaturation ratio, calculated as p/p_o). p is the vapour pressure of the growth species, p_0 is the equilibrium vapour pressure of the condensed phase, k is the Boltzman constant and T is the absolute temperature in Kelvin.

From Equation 6.1, P_N is proportional to exp $\left(\frac{1}{T^2}\right)$. This indicates that an increase in temperature increases the probability of nanotube nucleation. This is evident from the growth of nanotubes when the experimental temperature was increased from 900ºC to 1200ºC in increments of 100ºC. Secondly, the surface energy of the metal oxide catalyst also affects the probability of nucleation for nanostructures. MgO and Fe_2O_3 were used in this work. Supersaturation α_s and P_N are also proportional meaning if the partial pressure of the growth species rises, the level of supersaturation will increase. Consequently, there will be a greater probability of nucleation of BN nanostructures due to the heightened degree of supersaturation caused by the increased partial pressure of the growth species. This was accomplished by layering Si-substrates on top of the precursors in a crucible

enclosed within a sealed quartz tube in an NH_3-filled atmosphere. The CVD experimental setup is intended to collect and capture growth species in order to improve the nucleation rate of BN nanostructures formed by reacting with NH_3 gas.

6.2 SCANNING ELECTRON MICROSCOPY (SEM)

6.2.1 SYNTHESIZED BNNTS MORPHOLOGY

Raman and GIXRD analysis have verified that the SEM images reveal the presence of both BN nanostructures and BN nanotubes. BNNTs appear as long, thin structures with relatively uniform diameters, while the nanostructures appear as irregularly shaped structures clustered together forming cauliflowers like shapes with varying sizes. Figure 5.5, which is the SEM image of samples prepared at a temperature of 1200 °C; shows BN-nanospheres of different sizes and BNNTs dispersed throughout the surface of the sample.

6.2.2 SYNTHESIZED BNNTS DIAMETER

BNNTs in the SEM images have diameters of ~30-80nm, which is consistent with the reported diameters in previous studies [72]. The diameter of BNNTs can affect the mechanical, electrical, or other properties of the BNNTs [73]. In a study conducted by Chen *et al* [74], examining the mechanical properties of individual BNNTs, the findings demonstrated that the effective transverse elastic modulus of the BNNTs increases with the number of tube walls and decreases with an increase in diameter. The diameter of the BNNTs can also affect their electrical properties, such as their electrical conductivity and bandgap. Smaller diameter BNNTs have been shown to have wider bandgaps and lower electrical conductivity than larger diameter BNNTs [75]. Therefore, the ~30-80nm diameter range of the BNNTs in the SEM image suggest that they have relatively wide bandgaps and low electrical conductivity, which could limit their use in electronic applications that require high conductivity and smaller bandgap.

The diameter of the BNNTs can also affect other properties, such as their thermal conductivity and effective surface area for electrochemical applications. Smaller diameter BNNTs have been shown to have higher thermal conductivity and surface area than larger diameter BNNTs [73][75]. Therefore, the 30-80 nm diameter range

of the BNNTs in the SEM image suggest that they have relatively high thermal conductivity and surface area, which could make them suitable for applications that require efficient heat transfer or high surface area, such as catalyst support.

At an energy of 150 keV, the range of a boron ion in BNNTs can be estimated to be about ~400 nm using the SRIM software package. This means that the boron ions are expected to pass through several BNNTs in the size range of 30-80 nm before coming to a stop. This suggests that the primary mechanism for energy loss of the boron ions in BNNTs will be through electronic stopping. The contribution of nuclear stopping to the total energy loss of the boron ions is expected to be small at this energy [43].

6.3 GRAZING INCIDENCE XRD

Grazing Incidence X-ray Diffraction (GIXRD) and conventional X-ray diffraction (XRD) are both techniques used to study the crystal structure and morphology of thin films. However, GIXRD is generally preferred over conventional XRD for the analysis of thin films on substrates. The reasons why GIXRD may be preferred over conventional XRD for the analysis of thin films is because in GIXRD, the X-rays are incident on the sample at a very low angle (typically less than 1 degree) with respect to the surface of the sample in this work grazing incidence angle was with respect to the silicon substrates [66][76].

This results in a very shallow penetration depth of the X-rays into the sample, enhancing the surface sensitivity of the technique. The Si-substrate can often give a strong diffraction signal that can interfere with the analysis of the thin film. GIXRD is better than conventional XRD at reducing the contribution of the substrate to the diffraction pattern, as the incident angle of the X-rays is close to the critical angle for total external reflection, resulting in a significant reduction in the intensity of the scattered beam.

6.3.1 CALCULATED LATTICE CONSTANTS

The following equation, representing the planar spacing equation for hexagonal crystal structures, is given below, Equation 6.2 [77].

$$\frac{\mathbf{1}}{\boldsymbol{d^2}} = \frac{\mathbf{4}}{\mathbf{3}}\left(\frac{\boldsymbol{h^2 + hk + k^2}}{\boldsymbol{a^2}}\right) + \frac{\boldsymbol{l^2}}{\boldsymbol{c^2}} \qquad \mathbf{6.2}$$

$$\boldsymbol{sin^2\theta} = \left(\frac{\boldsymbol{\lambda^2}}{\boldsymbol{4a^2}}\right)\left[\frac{\mathbf{4}}{\mathbf{3}}(\boldsymbol{h^2 + hk + k^2}) + \frac{\boldsymbol{l^2}}{(\boldsymbol{c/a})^2}\right] \qquad \mathbf{6.3}$$

Equation 6.3, is derived by utilizing Bragg's law and the planar spacing equation for hexagonal systems. It incorporates various variables such as hkl (Miller indices), a and $\boldsymbol{c}$ (lattice parameters), $\boldsymbol{\lambda}$ (the wavelength used for diffraction measurements), and $\boldsymbol{\theta}$ (the diffraction angle).

In a given diffraction pattern, the lattice parameter $\boldsymbol{a}$, and the ratio $\boldsymbol{c/a}$ remain fixed. To calculate the lattice parameter $\boldsymbol{a}$, only the indices where $\boldsymbol{l=0}$, that is ($\boldsymbol{hk0}$), are used. Thus, $\boldsymbol{c}$ can be determined by only considering indices where $\boldsymbol{h=0}$, $\boldsymbol{k=0}$, i.e. ($\boldsymbol{00l}$). The density of the particles was then determined from the calculated lattice parameters using the following equation:

$$\boldsymbol{\rho = \frac{nA_r}{V_c N_A}} \qquad \textbf{6.4}$$

Where $\boldsymbol{A(g.mol^{-1})}$ is the atomic mass, $\boldsymbol{N_A}$ $\boldsymbol{(mol^{-1})}$ *is t*he Avogadro's constant, $\boldsymbol{V_c = a^2 c \sin(60°)}$ is the volume of the unit cell and $\boldsymbol{n}$ are the number of atoms in the unit cell.

$$\boldsymbol{D_{crystal} = \frac{k\lambda}{\beta_{\frac{1}{2}} \cos\theta}} \qquad \textbf{6.5}$$

The TOPAS-academic convolution-based model used (it employs the Scherrer Equation 6.5 and convolution for instrumentation broadening contribution), to determine in the crystallite size of the h-BN nanostructures. Where $\boldsymbol{D}$ is the crystallite size, $\boldsymbol{\lambda}$ wavelength of the incident X-ray beam, $\boldsymbol{k}$ is the Scherrer constant ~0.94, $\boldsymbol{\theta}$ is the Bragg angle for the specific ($\boldsymbol{hkl}$) plane, $\boldsymbol{\beta_{\frac{1}{2}}}$ is the FWHM of the diffraction peak [76].

The **Table 6.1** to **Table 6.3** below contain calculated lattice parameters and crystallite sizes of the As-grown implanted and implanted samples prepared at different temperatures:

Table 6.1: Determined lattice parameters and density of As-grown samples.

As grown samples	**900** ℃	**1000** ℃	**1100** ℃	**1200** ℃
***c* (nm)**	0.662	0.663	0.663	0.658
***a* (nm)**	0.249	0.249	0.249	0.247
Density (g/cm^3)	2.33	2,32	2,31	2,36
Crystallite Size(nm)	3.75	3.26	3.57	114.76

Table 6.2: Determined lattice parameters and density of samples implanted with 1e14 ions/cm^2 ion fluence.

1×10^{14} **ions/cm^2**	**900** ℃	**1000** ℃	**1100** ℃	**1200** ℃
***c* (nm)**	0.662	0.663	0.663	0.661
***a* (nm)**	0.249	0.249	0.249	0.249
Density (g/cm^3)	2.32	2.31	2.31	2.33
Crystallite Size (nm)	3.87	3.81	3.43	3.58

Table 6.3: Determined lattice parameters and density of samples implanted with 5e14 ions/cm^2 ion fluence.

5×10^{14} **ions/cm^2**	**900** ℃	**1000** ℃	**1100** ℃	**1200** ℃
***c* (nm)**	0.663	0.662	0.662	0.663
***a* (nm)**	0.249	0.249	0.249	0.249
Density (g/cm^3)	2.31	2.32	2.32	2.31
Crystallite Size(nm)	2.76	3.35	3.40	4.01

From **Table 6.1** to **Table 6.3** the average $\boldsymbol{a}$ and $\boldsymbol{c}$ lattice parameters were 0.249 ± 0.0002 nm and 0.662 ± 0.001 nm, respectively, yielding an interplanar distance of 0.166 ± 0.0001 nm.

The peak size and broadening in XRD patterns give a lot of information, for example factors that cause peak broadening include instrumentation, the presence of defects, the differences in strain and Scherrer crystallite size. The Hall-Williamson method can be used to determine the strain in the crystallites [78]:

$$\boldsymbol{\beta_{\frac{1}{2}} \cos\theta = \frac{k\lambda}{D} + \epsilon(4 \sin\theta)} \qquad \textbf{6.6}$$

Where $\boldsymbol{\epsilon}$ is the strain in the crystallites. The work done by E. Hernández et al [79] and N. Konstantin et al [80], they determined the theoretical average elastic modulus ($\boldsymbol{E_{BN}}$) of BNNTs to be ~850GPa using *ab initio* calculations. Suryavanshi, Abhijit P. et al [81], experimentally determined the average value of ~722GPa, from 18 individually cantilevered BNNTs, this result is in good agreement with the theoretical value [79]. In this work the elastic modulus determined from *ab initio* computations was used because one advantage of using *ab initio* methods to calculate the elastic modulus of BNNTs is that they can provide detailed information about the underlying electronic and atomic structure of the material, which can help to explain the mechanical properties [80].

Table 6.4 has the calculated strain and stress in the crystallite for As-grown and implanted samples. Strain within the crystal lattice causes a distortion of the regular atomic arrange. This distortion can result in additional scattering of X-rays, leading to broadening of the diffraction peaks. The width of the XRD peak varies inversely with Scherrer crystallite size. The peak broadens as the crystallite size decreases, Equation 6.5. The calculated average stress and strain were 0.52 ± 0.003 and 441 ± 3.0 GPa, respectively.

Figure 6.1 show the stress-strain of as-grown and ion implanted BN-nanostructures. An increase in the crystallite strain, increases the stress in the BN-nanostructures.

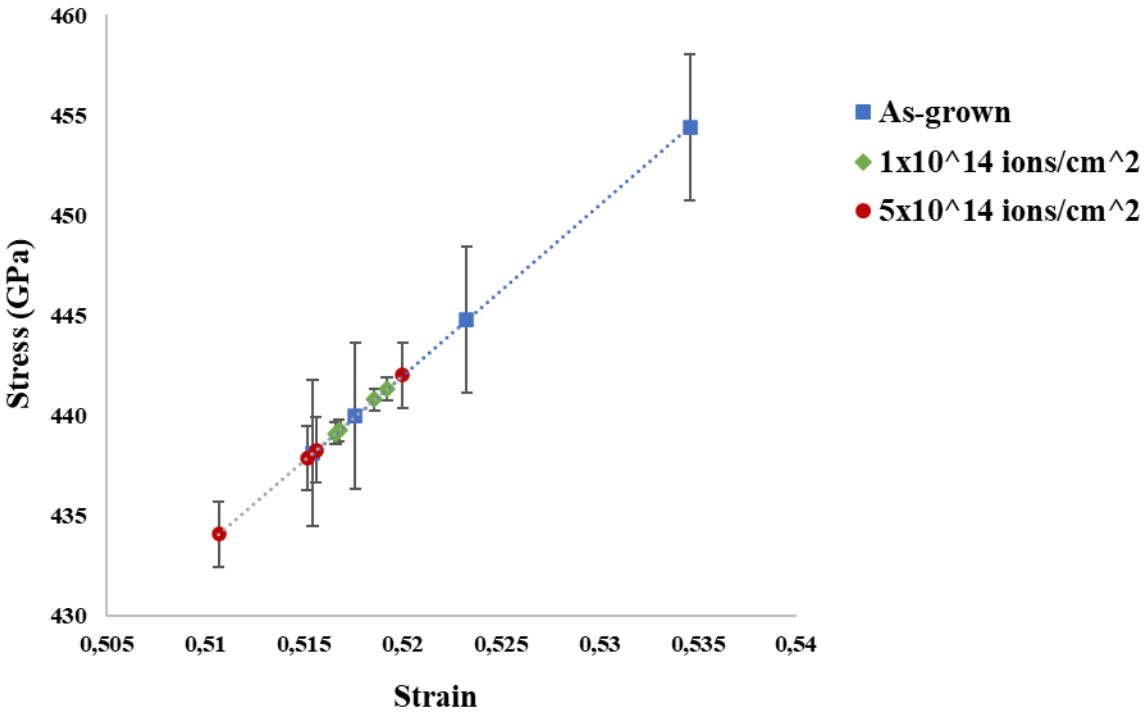

Figure 6.1: The stress-strain graph of ion implanted BN nanostructures

Table 6.4: The calculated strain and stress values.

Temperature	**As-grown**		$\mathbf{1 \times 10^{14}\ ions/cm^2}$		$\mathbf{5 \times 10^{14}\ ions/cm^2}$	
	Strain, $\boldsymbol{\epsilon}$	Stress, $\boldsymbol{\sigma_s}$ (GPa)	Strain, $\boldsymbol{\epsilon}$	Stress, $\boldsymbol{\sigma_s}$ (GPa)	Strain, $\boldsymbol{\epsilon}$	Stress, $\boldsymbol{\sigma_s}$ (GPa)
900℃	0.523	445	0.518	441	0.511	434
1000℃	0.515	438	0.519	441	0.516	438
1100℃	0.518	440	0517	439	0.516	438
1200℃	0.535	454	0.517	439	0.520	442

6.3.2 REFINED STRUCTURAL DETAILS

The ~54 ° 2θ peak was tentatively assigned to the (004) h-BN peak index. From this, the sample crystallinity can be considered using peak width as a proxy. This can be interpreted using the Scherrer crystallite size which is related to size of the coherent scattering domains in the structure. The presented values consider broadening from a 3 mm X-ray beam footprint and no additional instrument broadening factors making them a lower bound estimate. When considering nanomaterials, the sample broadening dominates the overall peak broadening making estimates for such materials a reasonable approximation even without a comprehensive instrument profile description. The majority of samples provided broad peaks indicative of a nano-crystalline material with the exception of the 1200 °C as-grown sample. The latter was refined to a ~115 nm crystallite size with the balance of samples represented by an average size of 3.5 nm (σ = 0.3 nm). The difference between these values is suggested to be a result of the formation of alternative structural features as observed in the SEM microscopy. At 1200 °C nano-spheres with sizes as large as a few hundred nanometres are formed which could explain the narrower diffraction peak. This is not observed in the XRD patterns after ion implantation, which is a process with the potential to segment scattering domains. This is converse to the Raman measurements in which there is an increased coherent interaction volume on implantation.

The c-axis lattice parameter was refined using the position of the tentatively assigned (004) h-BN peak. The values below 1200 °C were sufficiently close with no clear trends, such that they are described by the average of 0.662 ± 0.0006 nm. For the 1200 °C samples the ***c***-axis showed relative tensile strain with implantation with lattice parameters of 0.658, 0.662, and 0.663 nm for the as-deposited, 1×10^{14} and 5×10^{14} $\mathrm{ions/cm^2}$ samples respectively.

Similarly, the differences in integrated intensity for samples prepared below 1200°C was 32.8 ± 7.2 where variations in substrate size between samples could account for the intensity variations. This was not the case for the 1200 °C samples where a marked decreasing trend in intensity was observed with ion implantation with values of 122, 41, and 27 for the as-grown, 1×10^{14} and 5×10^{14} $\mathrm{ions/cm^2}$ samples, respectively.

A possible explanation for the decrease in characteristic peak intensity in the 1200°C XRD patterns after ion implantation is loss of crystallinity in the sample due to ion bombardment. The ion implantation process involves the introduction of high-energy ions into the lattice structure of the material, which can cause displacement of atoms from their original lattice sites, leading to the formation of lattice defects such as vacancies, interstitials, and dislocations. These structural defects may induce strain, micro-strain and/or affect domain size of the coherent scattering in the crystallites. Such effects can lead to peak shifts and peak broadening.

The high peak intensity observed at 1200ºC for the as-grown BNNTs is an indication of increase in crystallinity, which typically improves the optical and vibrational properties of the material. At higher temperatures, the growth conditions of the BNNTs may have favoured the formation of longer and more crystalline BNNTs or the formation of competing structures such as identified in SEM images of Figure 5.5.

6.3.3 X-RAY ATTENUATION AND X-RAY DEPTH

As an X-ray beam passes through a material, the intensity of the X-ray photons decreases due to interactions with the atoms of the sample. The loss of X-ray photons from the beam results in a decrease in intensity. The attenuation depth is defined as the depth at which the X-ray intensity is reduced to 1/e of its value at the surface of the material. The reduction in intensity is influenced by the absorption coefficient ($\boldsymbol{A}$) and penetration depth ($\boldsymbol{X_L}$) of the material. The intensity decreases exponentially and is given by the following Equation 6.7 [82]:

$$\boldsymbol{X_L = 1/(\mu_m \rho)} \qquad \textbf{6.7}$$

This is called the X-ray attenuation length ($\boldsymbol{X_L}$) or the mean free path of X-rays. The equation incorporates variables such as the mass absorption coefficient ($\boldsymbol{\mu}$) and the density ($\boldsymbol{\rho}$) of the material. The density of silicon wafer and h-BN is 2.33 g/cm^3 and

2.27 g/cm^3, respectively, while the X-ray tube used in the study had a CuKα_1 wavelength of 1.540Å, which corresponds to an X-ray photon energy of 8.051 keV. Consequently, the mass absorption values for an X-ray photon energy of 8.051 keV are $\boldsymbol{\mu_m}$(8.051 keV) = 1.85 cm^2/g for boron, $\boldsymbol{\mu_m}$ (8.051 keV) = 6.71 cm^2/g for nitrogen, and 64.21 cm^2/g for silicon [83]. The sum of the individual coefficients, each multiplied by the weight fraction present, yields the overall mass coefficient of BN:

$\boldsymbol{\mu_{BN}} = C_B\mu_B + C_N\mu_N = (0.44)(1.85\text{cm}^2/\text{g}) + (0.56)(6.71\text{cm}^2/\text{g})$, giving $\boldsymbol{\mu_m} = 4.57\text{cm}^2/\text{g} + 64.21\text{cm}^2/\text{g}$ as the absorption mass coefficient for BN and Si-substrate [83]. Based on the given values of mass absorption coefficient and density, the attenuation length of X-ray photons was calculated to be ~32µm. **Table 6.5** presents the calculated X-ray attenuation lengths obtained from the experimentally determined density values (see **Table 6.1** to **Table 6.3**).

Table 6.5: The X-ray attenuation length is determined from density values that are obtained experimentally.

T (°C)	**As-grown**	$\mathbf{1 \times 10^{14}\ ions/cm^2}$	$\mathbf{5 \times 10^{14}\ ions/cm^2}$
	Attenuation length, $\boldsymbol{X_L}$ **(µm)**	Attenuation length, $\boldsymbol{X_L}$ **(µm)**	Attenuation length, $\boldsymbol{X_L}$ **(µm)**
900	31.2	31.3	31.3
1000	31.3	31.3	31.3
1100	31.3	31.3	31.3
1200	31.0	31.2	31.3

The GIXRD spectral data shows the intensity of diffraction peaks as a function of the diffraction angle. These peaks occur at specific 2θ angles where the material can diffract X-rays based on Bragg's equation. In other words, for a substance to refract X-rays, the 2θ angle needs to fulfil the required conditions of Bragg's equation.

When analysing crystal structure characteristics like the lattice parameters, Miller indices are used to study the diffraction peak patterns, which are used to identify various planes of a material. This aids in the identifying of the material.

The X-rays' penetration depth ($\boldsymbol{X_d}$) into the material is crucial when performing X-ray diffraction on samples. The X-rays are, however, aimed at the material at a very small angle, GIXRD was used because the implanted layer for boron ions was very thin, around 0.4 μm, Figure 5.1. To find the X-ray depth, it was necessary to calculate the X-ray attenuation length ($\boldsymbol{X_L}$). The X-ray depth is calculated from the following Equation 6.8 (see Figure 6.2).

$$\boldsymbol{X_d = X_L \times tan\,(\vartheta_i)} \qquad \textbf{6.8}$$

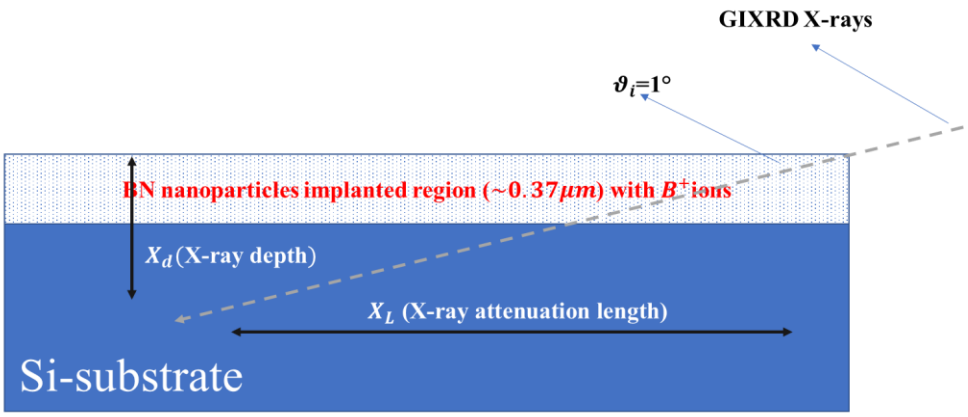

Figure 6.2: A cross section visual illustrating the shape of X-ray attenuation length and X-ray depth.

Table 6.6: Calculated X-ray depth values

T (°C)	As-grown		1×10^{14} ions/cm^2		5×10^{14} ions/cm^2	
	Attenuation length, X_L (μm)	X-ray depth, X_d (μm)	Attenuation length, X_L (μm)	X-ray depth, X_d (μm)	Attenuation length, X_L (μm)	X-ray depth, X_d (μm)
900	31.2	0.54	31.3	0.55	31.3	0.55
1000	31.3	0.55	31.3	0.55	31.3	0.55
1100	31.3	0.55	31.3	0.55	31.3	0.55
1200	31.0	0.54	31.2	0.54	31.3	0.55

Figure 6.3 show how changes in the density of nanostructures affect the attenuation length of X-rays concerning their penetration depth. When the density of the nanostructures rises, the attenuation of X-rays diminishes, leading to a reduction in the distance at which the majority of X-rays will stop. The average attenuation length and depth of X-rays is 31.30 ± 0.05 μm and 0.55 ± 0.0009 μm, respectively.

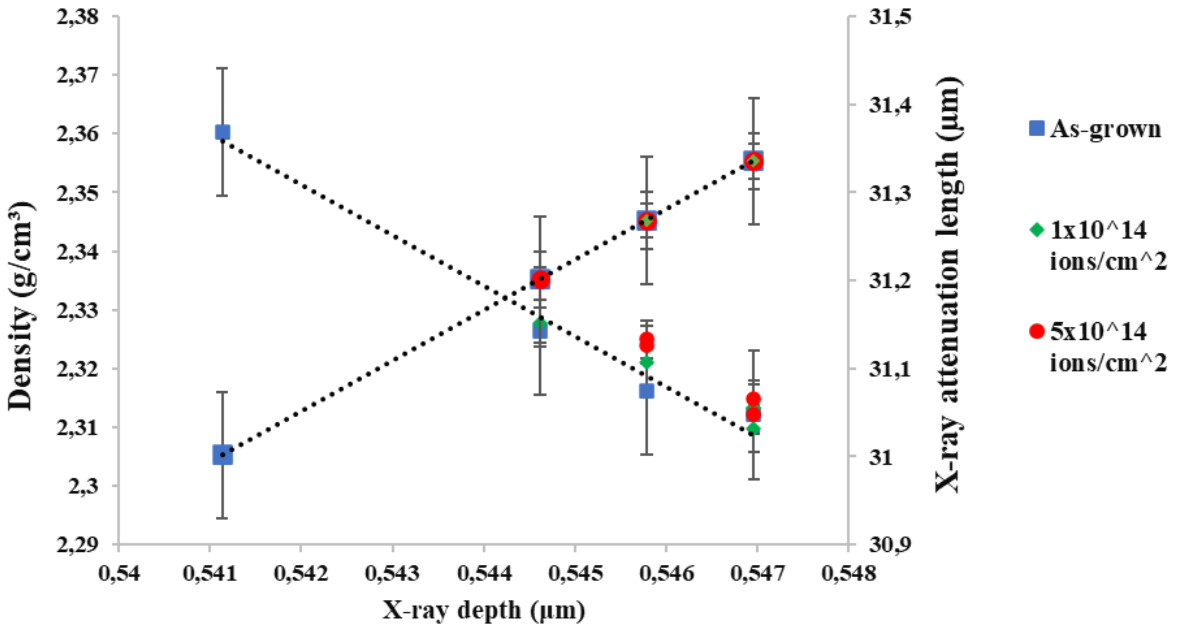

Figure 6.3: The relationship of the BN nanostructures density and attenuation length as a function of the depth of X-rays.

Due to the implanted layer's approximate thickness of~ 0.4 µm and it is the depth we would desire for our X-rays to travel, therefore Equation 6.8 yields ϑ_i= 0.67°, which is the angle needed to acquire high sensitivity from the XRD spectra. Although the GIXRD apparatus used was unable to adapt to a 0.7° angle, the 1° angle was successful because the average Xray depth determined was ~0.55 ± 0.0009 µm and it allowed us to identify h-BN characteristic peak around 51º-57º 2θ angle area.

6.4 RAMAN DERIVED CALCULATED AVERAGE CRYSTALLITE DOMAIN SIZE

The effects of ion implantation can be explored by determining the average crystallite domain size. The work done by Nemanich *et al* [84] is relevant, as they used the same excitation wavelength as in this work. They showed that the average crystallite domain size (***L***) can be determined by the following equation (Figure 7 of ref [84]):

$$\boldsymbol{FWHM = \frac{1417}{L} + 8.7} \qquad \textbf{6.9}$$

where ***L*** is the average crystallite domain size (in Å) and ***FWHM*** is the h-BN Raman peak FWHM in cm^{-1} units.

Table 6.7 below has the calculated average crystallite domain size values. The width of a Raman peak is related to phonon lifetime, and this is governed by the average crystallite domain size. The phonon will have a short lifetime for small domain size, meaning the FWHM is large, and for a large domain size the phonon will have a longer lifetime, meaning FWHM is smaller. Figure 6.4 displays the average crystallite domain size as a function of FWHM of the Raman E_{2g} mode of vibration of *h-BN*. An increase in domain size is observed after ion implantation. A narrow FWHM is associated with a more crystalline material, i.e., increased crystallinity and either the absence of inhomogeneous strain or very little such strain is present. These findings imply that ion implantation promotes or improves the growth of BN nanostructures with sp^2 hybridized planar bonding.

The key finding in this study was the significant enhancement of crystallite domain size (i.e., an increase in ***L***) in samples synthesized at 1100°C after boron ion implantation at a fluence of $5x10^{14}$ ions/cm^2. The effect can also be observed in samples grown at 1200ºC but reduced. These conditions may be optimal for promoting growth of the BN crystallites. The increase in crystallite domain size after

ion implantation with boron ions can also be attributed to the presence of boron atoms in the lattice [47].

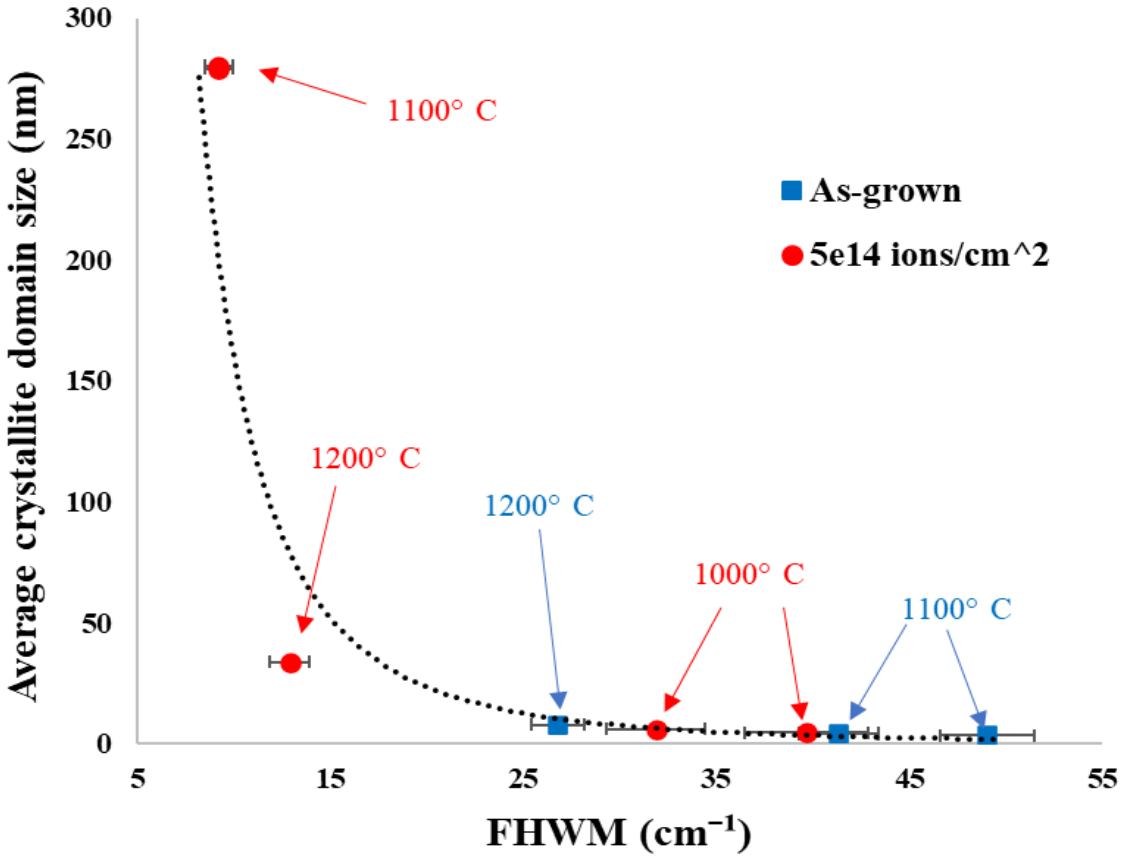

Figure 6.4: Graph of the Raman peak derived average crystallite domain size as a function of FWHM.

The key finding in this study is the significant enhancement of crystallite domain size (i.e., an increase in ***L***) in samples synthesized at 1100°C after boron ion implantation at a fluence of $5x10^{14}$ ions/cm^2. The effect can also be observed in samples grown at 1200 ºC but reduced. These conditions may be optimal for promoting growth of the BN crystallites. The increase in crystallite domain size after

ion implantation with boron ions can also be attributed to the presence of boron atoms in the lattice [47].

Table 6.7: Raman derived Calculated Average crystallite domain size.

	As-grown		**5×10^{14} ions/cm^2**	
T (°C)	FWHM (cm^{-1})	Average crystallite domain size (nm)	FWHM (cm^{-1})	Average crystallite domain size (nm)
900	-	-	-	-
1000	-	-	31.9 ± 2	6.1 ± 0.3
	-	-	39.7 ± 2	4.6 ± 0.2
1100	49 ± 1.3	3.5 ± 0.1	9.2 ± 0.3	270 ± 10
	41.4 ± 1.9	4.3 ± 0.2	9.2 ± 0.3	280 ± 9.1
1200	26.8 ± 2.2	7.8 ± 0.7	12.9 ± 0.9	34.0 ± 2.3

6.4.1 RAMAN SPECTROSCOPY MICROGRAPH IMAGES

The Si samples (Figure 5.13 to Figure 5.17) had an obvious colour difference that occurred before and after ion implantation, with dark regions. The formation of boron nitride nanostructures on Si-substrates and subsequent ion implantation with boron ions can cause significant changes in the surface composition and structure, leading to a change in colour. BN nanostructures are composed of boron and nitrogen atoms arranged in a tubular structure. When formed on a Si-substrate, the BN nanostructures can interact with the Si-surface, which can result in a change in the surface composition and structure. Ion implantation with boron ions at 150 keV energies can further modify the surface of the Si substrate and the BN

nanostructures. The boron ions can penetrate the surface layers of the Si-substrate and the BN nanostructures, causing damage and creating vacancies in the crystal lattice. As a result, the composition and structure of the material can be altered, which can affect its optical properties, including its colour. The formation of dark regions on the surface of the samples in this study is an indicative of the formation of BN nanostructures during the CVD experiment and ion implantation process. During the CVD process, precursors are introduced into a reaction chamber, where they react to form a solid thin film on the substrate. The precursors used in the CVD experiment reacted to form BN nanostructures, which then became incorporated into the thin film deposited onto the Si substrate. Additionally, the ion implantation process had caused the breakdown of the material lattice, leading to the formation of additional BN nanostructures.

6.5 SUMMARY

The work presented herein was focused on using Chemical Vapour Deposition as a method for synthesizing boron nitride nanostructures (particularly nanotubes), and to using ion implantation for selectively introducing defects into the BN nanostructures. The BN nanostructures were implanted with 150 keV boron ions at fluences of $1x10^{14}$ and $5x10^{14}$ ions/cm^2 at room temperature. The samples were analysed with scanning electron microscopy, Raman spectroscopy and Grazing incidence X-ray diffraction. Ion implantation introduced defects into the surface of the samples and these defects caused an increase in stress levels in the BN nanostructures, increasing the local density to favour more crystalized nanostructures.

BN nanostructures and BNNTs were evident in the SEM images of samples prepared at 1000°C, 1100°C and 1200°C. In contrast to the nanostructures which appeared clumped together to create cauliflower-like shapes with various sizes, BNNTs were long, thin structures with almost identical diameters.

Prior to ion implantation, samples synthesized at 1000°C showed no peak in the vicinity of 1366 cm^{-1}, whereas samples synthesized at 1100°C and 1200°C displayed a definite broad peak in the range 1350-1370 cm^{-1}. This is due to the existence of amorphous h-BN in these samples.

The Raman spectra of samples implanted with ion fluence $5x10^{14}$ ions/cm^2 at 1000°C exhibit an amorphous h-BN peak, while samples produced at 1100°C and 1200°C had more intense E_{2g} vibrational mode of h-BN about 1366 cm^{-1}. For all samples, Raman analysis revealed no E_{2g} mode of vibration of h-BN at fluence $1x\ 10^{14}$ ions/cm^2. There was no active 1366 cm^{-1} Raman signal in the samples synthesized at 900 °C.

Raman micrographs showed colour variations on the surface of the samples before and after ion implantation, with dark regions. The development of dark areas on the

samples' surfaces in this work is evidence that BN nanostructures formed during ion implantation and CVD.

The effects of ion implantation were also explored by determining the Raman derived average crystallite domain size. The most notable outcome of the experiment was the significant enhancement in the crystallite domain size of the 1100°C samples after ion implantation with boron ions at a fluence of $5x10^{14}$ ions/cm^2. The effect is also observed in the 1200ºC samples but to a lesser extent.

XRD analysis revealed a well-defined 55.4° 2θ peak consistent with a h-BN (004) peak.

When using Raman spectroscopy, we need to be mindful of where we take measurements. The laser beam used in Raman spectroscopy is very small, about 1µm wide. So, we can only measure tiny clusters of material on the silicon substrate at a time. It's not possible to measure all the groups individually. On the other hand, with grazing X-ray diffraction (GXRD), the beam is much wider, allowing us to get a better average of the structures on the surface.

CHAPTER 7

7 CONCLUSION

- Synthesis of BNNTs was successful at 1100°C and 1200°C CVD temperature.

- The BNNTs were long, thin structures with diameters around ~30-80nm range, whereas the nanostructures appeared as amorphous structures clumped together to create cauliflower-like shapes with various sizes.

- The Raman analysis detected a peak at 1367cm^{-1}, which indicates the presence of sp^2 hybridized BN planar bonding and was attributed to the high frequency E_{2g} mode for the h-BN peak. This peak was more distinctly observed at 1100 and 1200 °C, both before and after ion implantation.

- The Raman derived average crystallite domain size values confirmed that after ion implantation the phonon lifetime was longer because of the large domain size, this means that the BN nanostructures are more crystallized.

- X-ray diffraction (GIXRD) spectra revealed a prominent peak between 54 and 56 °, corresponding to the (004) h-BN reflection, which was used to determine the average lattice parameter ***c***~0.662 ± 0.001 nm representing the stacking direction of the BN layers.

- The majority of the samples had broad peaks, indicative of a nanocrystalline material. The only exception was the sample grown at 1200 °C, which was found to have a Scherrer crystallite size >100 nm. In contrast, the rest of the samples had an average size of 3.5 $\pm$ 0.3 nm.

- The average density of the BN nanostructures was determined to be 2.32 $\pm$ 0.006 g/cm^3

- The average strain and stress values were 0.52 ± 0.003 and 441 ± 3.0 GPa, respectively.

- When the density of the nanostructures rises, the attenuation length of X-rays decreases, leading to a reduction in the distance at which the majority of X-rays will stop (X-ray depth). The average attenuation length and depth of X-rays were 31.30 ± 0.05 μm and 0.55 ± 0.0009 μm , respectively.

- The increase in Raman derived crystallite domain size of BN nanostructures after ion implantation with boron ions can be attributed to a number of factors. During ion implantation, energetic ions are implanted into the material, causing damage and creating vacancies in the crystal lattice. As a result, the implanted material undergoes a process of annealing and recrystallization as the vacancies are gradually filled in by atoms diffusing through the lattice. This process can lead to an increase in the size of the crystallite domains, which are regions of the material where the atoms are in a crystal lattice.

- The significant increase in the crystallite domain size in the 1100°C and 1200°C samples after ion implantation suggested that these conditions may be optimal for promoting recrystallization and growth of the BN crystallites. However, further studies would be needed to confirm these findings and explore the mechanisms underlying the observed changes in the crystallite domain size.

In conclusion, this work shows that ion implantation can be used to introduce defects into BN nanostructures, leading to the growth of more crystallized nanostructures. The results of this study might be useful for the development of BN-based materials with enhanced mechanical and electronic properties for a wide range of applications.

8 APPENDIX A

8.1 WILLIAMSON-HALL METHOD

When determining crystallite size by Hall-Williamson method the first step is to determine pure diffraction breadth (solely due to small crystallite size). It is better to use integrated width (i.e., integrated intensity) of the diffraction peak rather than Full Width at Half Maximum (FWHM) mainly for XRD broad peaks. Most diffractometers are equipped with a software for measurements of integrated intensity diffraction peaks (is the ratio of the area under a peak above the estimated background to the maximum height of that peak)[85]. Thus, the observed peak broadening $\boldsymbol{B_o}$ is:

$$\boldsymbol{B_0 = B_i + B_r} \qquad \textbf{8.1}$$

Where $\boldsymbol{B_o}$ is the observed peak broadening in radians, $\boldsymbol{B_i}$ the broadening due instrumental factors, in radians and Br is the broadening due to crystallite size and lattice strain.

Instrumental broadening Bi maybe assumed to be for a well annealed high-purity silicon (standard) sample subjected to XRD under identical conditions as for the test sample.

Equation 8.1 holds good if the diffraction peaks are pure Gaussian. When the peaks show mixed behaviour i.e., partly Gaussian the following relationship between $\boldsymbol{Bo}$, $\boldsymbol{B_i}$ and $\boldsymbol{B_r}$ holds true:

$$\boldsymbol{B_r = ((B_o - B_i)(B_o^2 - B_i^2)^{\frac{1}{2}})^{\frac{1}{2}}} \qquad \textbf{8.2}$$

According to Scherrer the broadening due to small crystallite size is expressed as in Equation 6.5, where FWHM is $\boldsymbol{B_c}$, in this case.

Similarly, according to Wilson the broadening due to lattice strain is given by:

$$B_s = \epsilon \tan \theta \qquad 8.3$$

Where B_s is the peak broadening due to lattice strain, ϵ is the strain distribution within the material θ Bragg's angle [78][85]. Therefore, the total peak broadening B_r, can be expressed as

$$B_r \cos \theta = \frac{k\lambda}{D} + \epsilon \sin \theta \qquad 8.4$$

8.2 SIMULATED XRD PATTERNS

8.2.1 CUBIC BN F-43M COD 9008834

a = 3.61500 Å

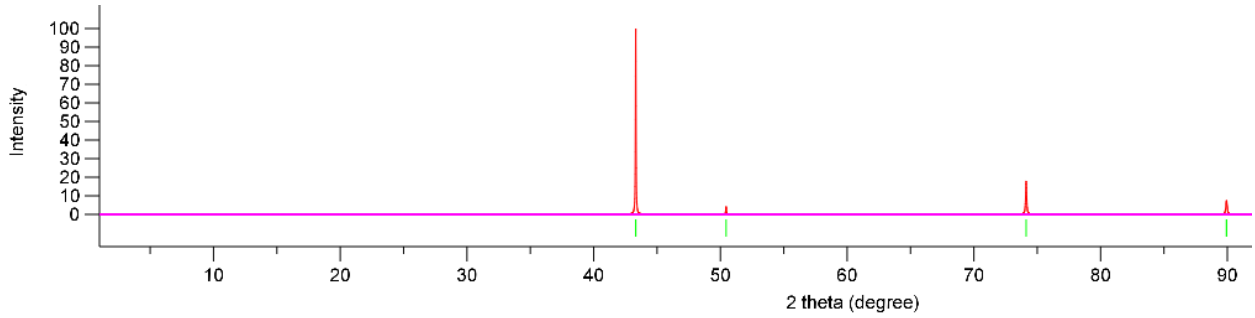

Figure 8.1: Simulated XRD pattern of Cubic BN

Table 8.1: Crystallographic Data for Cubic Boron nitride (CBN) Obtained from X-ray Diffraction (XRD) Analysis, COD 9008834.

h	k	l	d (Å)	F(real)	F(imag)	|F|	2θ	I
1	1	-1	2.08712	8.80259	15.0991	17.4777	43.3167	99.5027
1	1	1	2.08712	8.93902	-15.0695	17.5213	43.3167	100.0000
2	0	0	1.80750	-5.21762	-0.0523908	5.21789	50.4491	9.4199
2	2	0	1.27810	14.3641	0.0754537	14.3643	74.1257	61.8910
3	1	-1	1.08996	5.21645	-6.86216	8.61978	89.937	17.0091
3	1	1	1.08996	5.09938	6.88758	8.56986	89.937	16.8126

8.2.2 HEXAGONAL BN P63.MMC COD 9008997

a = 2.50399, c = 6.66120, γ = 120 °

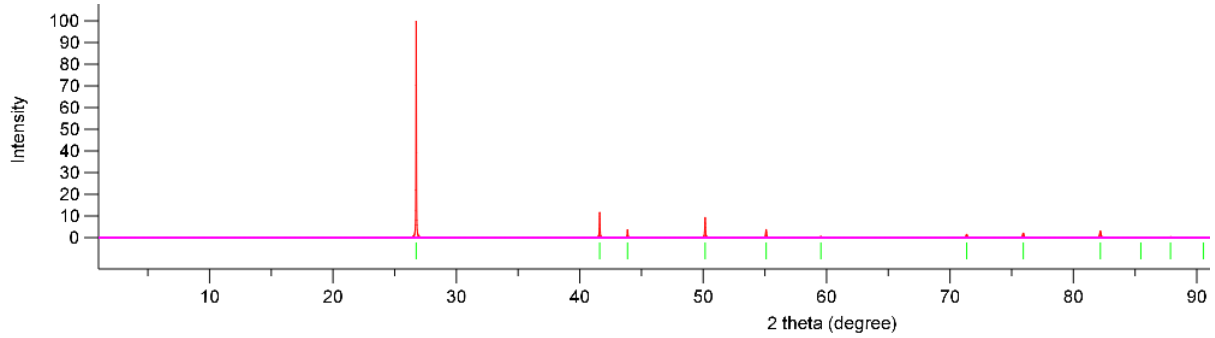

Figure 8.2: Simulated XRD pattern of h-BN

Table 8.2: Crystallographic Data for hexagonal Boron nitride (h-BN) Obtained from X-ray Diffraction (XRD) Analysis, COD 9008997.

h	k	l	d (Å)	F(real)	F(imag)	|F|	2θ	I
0	0	2	3.33060	-17.0773	-0.0429861	17.0774	26.7447	100.0000
1	0	0	2.16852	-6.20385	-0.0208448	6.20389	41.6136	15.1500
1	0	1	2.06200	2.65652	0.0230916	2.65662	43.8715	4.9351
1	0	2	1.81728	5.23154	0.0203803	5.23158	50.1589	14.1297
0	0	4	1.66530	9.56077	0.0401759	9.56085	55.1045	6.3493
1	0	3	1.55139	-1.762	-0.0220738	1.76213	59.54	1.0864
1	0	4	1.32078	-3.72311	-0.0190479	3.72316	71.3539	3.2937
2	-1	0	1.25199	7.02049	0.0374844	7.02059	75.9409	5.2093
2	-1	2	1.17193	-6.52483	-0.036649	6.52493	82.1869	7.9324
1	0	5	1.13513	0.835562	0.020171	0.835805	85.4679	0.1238
0	0	6	1.11020	-6.14213	-0.0358944	6.14223	87.869	1.0818

This structure has a (004) reflection at 55.1° 2θ

Table 8.3: TOPAS results (GIXRD 1 deg, full footprint)

Sample	csize – FWHM	Integrated intensity	c-axis
900 C AD	3,88	40,4317	6,6159
900 C 1e14	3,99	34,8107	6,6210
900 C 5e14	2,81	45,3216	6,6268
1000 C AD	3,36	79,7019	6,6255
1000 C 1e14	3,97	24,4629	6,6315
1000 C 5e14	3,44	26,0982	6,6180
1100 C AD	3,69	26,7189	6,6297
1100 C 1e14	3,53	33,7658	6,6282
1100 C 5e14	3,50	33,8667	6,6173
1200 C AD	large	poor fit	6,5890
1200 C 1e14	3,69	60,3636	6,6148
1200 C 5e14	3,70	26,5198	6,6298

Table 8.4:TOPAS results (GIXRD 1 deg, 3mm footprint)

Sample	csize – FWHM	Count	Integrated intensity	Corr. Intensity	c-axis	Rwp	GoF
900 C AD	3.75100844	20s	40.8504667		6.615720	17.7665821	1.30611006
900 C 1e14	3.86506323	20s	35.1302864		6.620829	22.4215617	1.09282729
900 C 5e14	2.75595191	20s	45.8529855		6.626758	26.2354544	1.53774722
1000 C AD	3.25959102	60s	80.639446	26.9	6.625361	9.24480615	1.40095795
1000 C 1e14	3.80889272	20s	24.9149285		6.631629	15.2915826	1.11409237
1000 C 5e14	3.34576055	20s	26.4081411		6.618008	15.6140935	1.1567132
1100 C AD	3.57027745	20s	26.9631274		6.629294	14.3799477	1.05324125
1100 C 1e14	3.43314485	20s	34.2160545		6.628084	14.0999464	1.11727785
1100 C 5e14	3.40353154	20s	34.1924802		6.617044	18.0931072	1.08026833
1200 C AD	114.760396	10s	61.2628391	122.5	6.583849	34.0670534	1.82276075
1200 C 1e14	3.58065378 *	30s	61.1844559	40.8	6.614541	18.3068466	1.15330796
1200 C 5e14	4.0115477	20s	26.9631274		6.629294	14.3799477	1.05324125

Green: The plot of sim vs raw was checked and found to be reasonable. * fit quality

8.3 POLYCRYSTALLINE HEXAGONAL BORON NITRIDE RAMAN SPECTRUM

Figure 8.3 is virgin h-BN, which displays the intense vibrational mode at 1366 cm^{-1} due to the sp^2 hybridized BN planar bonding.

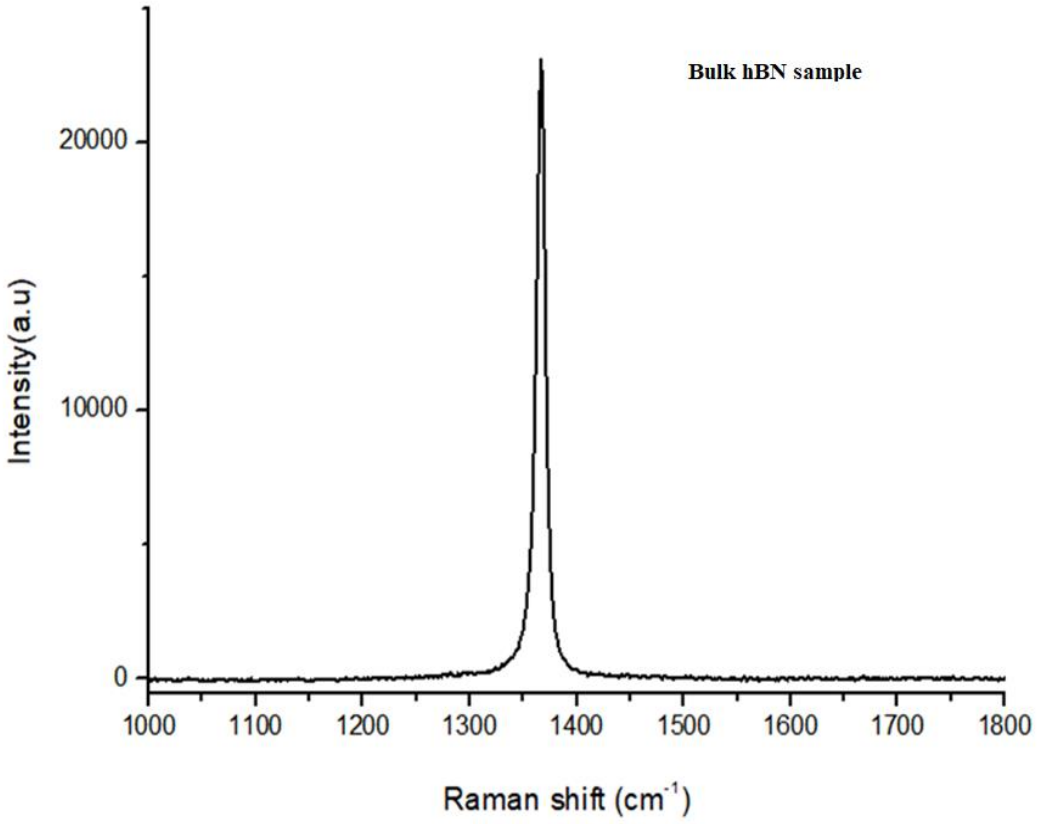

Figure 8.3: Raman Spectra of bulk h-BN.

9 APPENDIX B

9.1 CONFERENCES

- South African Institute of Physics annual conference 3-7 July 2017 at Stellenbosch University: Allotrope Conversion and Surface Hardness Increase in Ion Implanted Boron nitride.
- South African Institute of Physics annual conference 25-28 June 2018 at University of the Free State: Properties of boron nitride nanostructures formed by ion implantation.
- International Conference on Ion Beam Modification of Materials (IBMM-2018), San Antonio, Texas, USA, 24-29 June 2018: Properties of cubic Boron nitride nanostructures formed by ion implantation.
- South African Institute of Physics annual conference July 4-8, 2022, Nelson Mandela University, online event via Zoom: Synthesis and modification of Boron nitride nanotubes (BNNTs) using ion implantation.
- International Conference on Ion Beam Modification of Materials (IBMM-2022), Lisbon, Portugal, 10-15 July 2022: Synthesis and modification of Boron nitride nanotubes (BNNTs) using ion implantation.
- ARUA Centre of Excellence - Materials, Energy and Nanotechnology, online via Zoom, 19 August 2022: Synthesis and modification of Boron nitride nanotubes (BNNTs) using ion implantation.
- South African Institute of Physics annual conference 03-07 July 2023 University of Zululand: Synthesis and modification of Boron nitride nanotubes (BNNTs) using ion implantation.
- ARUA Centre of Excellence - Materials, Energy and Nanotechnology, online via Zoom, 19 July 2023: Synthesis and modification of Boron nitride nanotubes (BNNTs) using ion implantation.

9.2 PUBLICATIONS

- Derry, T. E., Lisema, L.I., Magabe, A. T., Aradi, E., Machaka, R., & Madhuku, M. (2018). Allotrope conversion and surface hardness increase in ion implanted boron nitride. *Surface and Coatings Technology* 355 (2018) 61-64.

10 REFERENCES

[1] A. U. Ubale and S. G. Ibrahim, "Structural, Electrical and Optical Properties of Nanostructured $FeCdS_3$ Thin Films Deposited by Chemical Spray Technique: Effect of Complex," *Int. J. Mater. Chem.*, vol. 2, no. 2, pp. 57–64, 2012.

[2] P. B. Mirkarimi, K. F. McCarty, and D. L. Medlin, "Review of advances in cubic boron nitride film synthesis," *Mater. Sci. Eng. R Reports*, vol. 21, no. 2, pp. 47–100, 1997.

[3] E. Aradi, R. M. Erasmus, and T. E. Derry, "Formation of c-BN nanoparticles by helium, lithium and boron ion implantation," *Nucl. Instruments Methods Phys. Res. Sect. B Beam Interact. with Mater. Atoms*, vol. 272, pp. 57–60, 2012.

[4] E. Aradi, S. R. Naidoo, R. M. Erasmus, B. Julies, and T. E. Derry, "Investigations on the characterization of ion implanted hexagonal boron nitride," *Nucl. Instruments Methods Phys. Res. Sect. B Beam Interact. with Mater. Atoms*, vol. 307, pp. 214–217, 2013.

[5] T. E. Derry, L. I. Lisema, A. T. Magabe, E. Aradi, R. Machaka, and M. Madhuku, "Allotrope conversion and surface hardness increase in ion implanted boron nitride," *Surf. Coatings Technol.*, vol. 355, pp. 61–64, 2018.

[6] Y. H. Kim, K. J. Chang, and S. G. Louie, "Electronic structure of radially deformed BN and BC3 nanotubes," *Phys. Rev. B - Condens. Matter Mater. Phys.*, vol. 63, no. 20, pp. 1–5, 2001.

[7] T. Norio, "On the basic concept of nanotechnology," *Proceeding of the ICPE.*, 1974.

[8] S. Iijima, "Helical microtubules of graphitic carbon.," *Nature*, vol. 354, no. 6348, pp. 56–58, 1991.

[9] D. Özmen, "Production and characterization of boron nitride nanotubes," MIDDLE EAST TECHNICAL UNIVERSITY, THESIS, 2008.

[10] Y. Gogotsi, *Nanotubes and Nanofibers*. 2006.

[11] M. H. Ali and I. R. Robiul, "A comparative review of Mg/CNTs and Al/CNTs composite to explore the prospect of bimetallic Mg-Al/CNTs composites,"

AIMS Mater. Sci. 7.3, pp. 217–243, 2020.

[12] X. Blase, A. Rubio, S. G. Louie, and M. L. Cohen, "Stability and band gap constancy of boron nitride nanotubes," *Epl*, vol. 28, no. 5, pp. 335–340, 1994.

[13] Y. Huang *et al.*, "Thin boron nitride nanotubes with exceptionally high strength and toughness," *Nanoscale*, vol. 5, no. 11, pp. 4840–4846, 2013.

[14] A. Maguer, E. Leroy, L. Bresson, E. Doris, A. Loiseau, and C. Mioskowski, "A versatile strategy for the functionalization of boron nitride nanotubes," *J. Mater. Chem.*, vol. 19, no. 9, pp. 1271–1275, 2009.

[15] M. Ishigami, "Properties of Boron Nitride Nanotubes," in *AIP conference proceedings*, vol. 94, no. 1, pp. 94–99.

[16] A. Zettl and N. G. Chopra, "Measurement of the elastic modulus of a multi wall boron nitride nanotube," *Solid State Commun.*, vol. 105, no. 5, pp. 297–300, 1998.

[17] Y. Chen, J. Zou, S. J. Campbell, and G. Le Caer, "Boron nitride nanotubes: Pronounced resistance to oxidation," *Appl. Phys. Lett.*, vol. 84, no. 13, pp. 2430–2432, 2004.

[18] Y. W. Yeh, Y. Raitses, B. E. Koel, and N. Yao, "Stable synthesis of few-layered boron nitride nanotubes by anodic arc discharge," *Sci. Rep.*, vol. 7, no. 1, pp. 1–7, 2017.

[19] Y. Chen, J. F. Gerald, J. S. Williams, and S. Bulcock, "Synthesis of boron nitride nanotubes at low temperatures using reactive ball milling," *Chem. Phys. Lett.*, vol. 299, no. 3–4, pp. 260–264, 1999.

[20] D. Golberg, Y. Bando, M. Eremets, K. Takemura, K. Kurashima, and H. Yusa, "Nanotubes in boron nitride laser heated at high pressure," *Appl. Phys. Lett.*, vol. 69, no. 14, pp. 2045–2047, 1996.

[21] Y. Chen, L. T. Chadderton, J. F. Gerald, and J. S. Williams, "A solid-state process for formation of boron nitride nanotubes," *Appl. Phys. Lett.*, vol. 74, no. 20, pp. 2960–2962, 1999.

[22] C. H. Lee, J. Wang, V. K. Kayatsha, J. Y. Huang, and Y. K. Yap, "Effective growth of boron nitride nanotubes by thermal chemical vapor deposition," *Nanotechnology*, vol. 19, no. 45, 2008.

[23] A. Z. Nasreen G. Chopra, R. J. Luyken, K. Cherrey, Vincent H. Crespi Marvin

L. Cohen, Steven G. Louie, “Boron nitride nanotubes,” *Mater. Sci. Eng. R Reports*, vol. 70, no. 3–6, pp. 92–111, 2010.

[24] I. Narita and T. Oku, “Synthesis of boron nitride nanotubes by using YB6 powder,” *Solid State Commun.*, vol. 122, no. 9, pp. 465–468, 2002.

[25] A. Loiseau, F. Willaime, N. Demoncy, G. Hug, and H. Pascard, “Boron nitride nanotubes with reduced numbers of layers synthesized by arc discharge,” *Phys. Rev. Lett.*, vol. 76, no. 25, pp. 4737–4740, 1996.

[26] J. Cumings and A. Zettl, “Mass-production of boron nitride double-wall nanotubes and nanococoons,” *Chem. Phys. Lett.*, vol. 316, no. 3–4, pp. 211–216, 2000.

[27] Y. Chen, M. Conway, J. S. Williams, and J. Zou, “Large-quantity production of high-yield boron nitride nanotubes,” *J. Mater. Res.*, vol. 17, no. 8, pp. 1896–1899, 2002.

[28] J. Kim, S. Lee, Y. R. Uhm, J. Jun, C. K. Rhee, and G. M. Kim, “Synthesis and growth of boron nitride nanotubes by a ball milling-annealing process,” *Acta Mater.*, vol. 59, no. 7, pp. 2807–2813, 2011.

[29] D. P. Yu *et al.*, “Synthesis of boron nitride nanotubes by means of excimer laser ablation at high temperature,” *Appl. Phys. Lett.*, vol. 72, no. 16, pp. 1966–1968, 1998.

[30] W. Han, B. Yoshio, K. Keiji, and S. Tadao, “Synthesis of boron nitride nanotubes from carbon nanotubes by a substitution reaction,” *Appl. Phys. Lett.*, vol. 73, no. 21, pp. 3085–3087, 1998.

[31] W.-Q. Han, M. W, C. John, and A. Zett, “Transformation of $B_xC_yN_z$ nanotubes to pure BN nanotubes.,” *Appl. Phys. Lett.*, vol. 81, no. 6, pp. 1110–1112, 2002.

[32] O. R. Lourie, C. R. Jones, B. M. Bartlett, P. C. Gibbons, R. S. Ruoff, and W. E. Buhro, “CVD growth of boron nitride nanotubes,” *Chem. Mater.*, vol. 12, no. 7, pp. 1808–1810, 2000.

[33] C. Tang, Y. Bando, T. Sato, and K. Kurashima, “A novel precursor for synthesis of pure boron nitride nanotubes,” *Chem. Commun.*, vol. 2, no. 12, pp. 1290–1291, 2002.

[34] C. Zhi, Y. Bando, C. Tan, and D. Golberg, “Effective precursor for high yield synthesis of pure BN nanotubes,” *Solid State Communications*, vol. 135, no. 1–2. pp. 67–70, 2005.

[35] R. S. Wagner and W. C. Ellis, “Vapor-liquid-solid mechanism of single crystal growth,” *Appl. Phys. Lett.*, vol. 4, no. 5, pp. 89–90, 1964.

[36] A. Pakdel, C. Zhi, Y. Bando, T. Nakayama, and D. Golberg, “A comprehensive analysis of the CVD growth of boron nitride nanotubes,” *Nanotechnology*, vol. 23, no. 21, p. 215601, 2012.

[37] P. Ahmad, M. U. Khandaker, and Y. M. Amin, “Synthesis of boron nitride nanotubes by Argon supported Thermal Chemical Vapor Deposition,” *Physica E: Low-Dimensional Systems and Nanostructures*, vol. 67. pp. 33–37, 2015.

[38] P. Ahmad, M. U. Khandaker, Z. R. Khan, and Y. M. Amin, “Synthesis of boron nitride nanotubes via chemical vapour deposition: A comprehensive review,” *RSC Adv.*, vol. 5, no. 44, pp. 35116–35137, 2015.

[39] H. Kragh, *Niels Bohr and the quantum atom: The Bohr model of atomic structure 1913-1925*. OUP Oxford, 2012.

[40] E. Aradi, “Investigations on the characterization of ion implanted hexagonal boron nitride,” University of the Witwatersrand, PhD Thesis, 2014.

[41] D. Fink and L. T. Chadderton, “Ion-solid interaction: Status and perspectives,” *Brazilian J. Phys.*, vol. 35, no. 3 B, pp. 735–740, 2005.

[42] J. F. Ziegler, *Ion implantation science and technology*. Elsevier, 2012.

[43] R. Machaka, “Ion Beam Modifications of Boron Nitride by Ion Implantation,” University of the Witwatersrand, MSc dissertation, 2008.

[44] G. Spitzlsperger, “Very brief Introduction to Ion Implantation for Semiconductor Manufacturing,” 2003.

[45] M. Backman, “Effect of Nuclear and Electronic Stopping Power on Ion Irradiation of Silicon-based Compounds.,” University of Helsinki Helsinki, ACADEMIC DISSERTATION, 2012.

[46] Y. N. Osetsky, D. J. Bacon, B. N. Singh, and B. Wirth, “Atomistic study of the generation, interaction, accumulation and annihilation of cascade-induced defect clusters,” *J. Nucl. Mater.*, vol. 307–311, no. 2 SUPPL., pp. 852–861, 2002.

[47] J. F. Prins and T. E. Derry, “Radiation defects and their annealing behaviour in ion-implanted diamonds,” *Nucl. Instruments Methods Phys. Res. Sect. B Beam Interact. with Mater. Atoms*, vol. 166, pp. 364–373, 2000.

[48] D. S. Gemmell, “Channeling and related effects in the motion of charged particles through crystals,” *Rev. Mod. Phys.*, vol. 46, no. 1, pp. 129–227, 1974.

[49] G. J. Phelps, “Dopant ion implantation simulations in 4H-Silicon Carbide,” *Model. Simul. Mater. Sci. Eng.*, vol. 12, no. 6, pp. 1139–1146, 2004.

[50] J. K. Hirvonen, C. A. Carosella, and G. K. Hubler, “Production of high-current metal ion beams,” vol. 189, pp. 103–106, 1981.

[51] S. Guanqing, L. Zhongyang, Z. Sioxiao, W. Beilu, L. Xiaodong, and J. Jinyun, “An Implantation Facility for Surface Modification of Metals,” *Inst. Nucl. Sci. Technol. Sichuan Univ. Chengdu, 610064, China*, pp. 9–11, 1998.

[52] M. A. Nastasi and W. M. James, “Ion Implantation and Synthesis of Materials,” *Berlin: Springer*, vol. 80, 2006.

[53] L. Rubin and J. Poate, “Ion Implantation in Silicon Technology,” *Ind. Phys.*, vol. 9, no. 3, pp. 12–15, 2003.

[54] P. H. Rose and G. Ryding, “Concepts and designs of ion implantation equipment for semiconductor processing,” *Rev. Sci. Instrum.*, vol. 77, no. 11, 2006.

[55] C. V Raman and K. S. Krishnan, “A new type of secondary radiation,” *Nature*, vol. 121, no. 3048, pp. 501–502, 1928.

[56] D. A. Long, “Raman spectroscopy,” in *The Characterization of Chemical Purity: Organic Compounds*, 1972, pp. 149–159.

[57] D. W. Ball, “Theory of Raman Spectroscopy,” *Spectroscopy*, vol. 18, no. 11, p. 21, 2001.

[58] G. Eckhardt, D. P. Bortfeld, and M. Geller, “Stimulated emission of stokes and anti-stokes raman lines from diamond, calcite, and -sulfur single crystals,” *Appl. Phys. Lett.*, vol. 3, no. 8, pp. 137–138, 1963.

[59] R. Machaka, “Ion Implantation into Boron Suboxide : Formation of Boron-Rich Structures and Related Phenomena,” University of the Witwatersrand, PHD Thesis, 2012.

[60] A. Jablonski, “Efficiency of anti-Stokes fluorescence in dyes,” *Nature*, vol. 131, no. 3319, pp. 839–840, 1993.

[61] R. Geich, C. H. Perry, and G. Rupprecht, “Normal Modes in Hexagonal Boron Nitride,” *Phys. Rev. B*, vol. 146, no. 2, pp. 543–547, 1966.

[62] R. J. Nemanich, S. A. Solin, and R. M. Martin, “Light Scattering Study of Boron Nitride Microcrystals,” *Phys. Rev. B*, vol. 23, no. 12, pp. 6843–6355, 1981.

[63] M. Ermrich and D. Opper, *X-RAY Poweder Diffraction for the analyst*. 2011.

[64] M. Birkholz, *Thin film analysis by X-ray scattering*. WILEY-VCH Verlag GmbH & Co. KGaA, 2006.

[65] J. I. Goldstein, D. E. Newbury, M. Joseph R., R. Nicholas WM, S. John Henry J, and C. J. David, *Scanning electron microscopy and X-ray microanalysis*. Springer US, 2017.

[66] W. C. Marra, P. Eisenberger, and A. Y. Cho, “X-ray total-external-reflection–Bragg diffraction: A structural study of the GaAs-Al interface,” *J. Appl. Phys.*, vol. 50, no. 11, pp. 6927–6933, 1979.

[67] A. Ul-Hamid, *A beginners’ guide to scanning electron microscopy*. Cham, Switzerland: Springer International Publishing, 2018.

[68] M. Tare, O. Roy Puli, S. M. Oros, A. Singh, and O. Roy, “Drosophila adult eye model to teach Scanning Electron Microscopy in an undergraduate cell biology laboratory.,” *Drosoph. Inf. Serv.*, vol. 92, no. January, 2009.

[69] S. Gražulis, D. Chateigner, R. T. Downs, A. F. T. Yokochi, M. Quirós, and L. Lutterotti, “Crystallography Open Database–an open-access collection of crystal structures,” *J. Appl. Crystallogr.*, vol. 42, no. 4, pp. 726–729, 2009.

[70] K. Nakamura, M. Fujitsuka, and M. Kitajima, “Disorder-Induced Line Broadening in First-Order Raman Scattering from Graphite,” *Phys. Rev. B*, vol. 41, pp. 12260–12263, 1990.

[71] D. Köken, P. Sungur, H. Cebeci, and F. Ç. Cebeci, “Revealing the Effect of Sulfur Compounds for Low-Temperature Synthesis of Boron Nitride Nanotubes from Boron Minerals,” *ACS Appl. Nano Mater.*, vol. 5, no. 2, pp. 2137–2146, 2022.

[72] S. Kalay, Z. Yilmaz, O. Sen, M. Emanet, E. Kazanc, and M. Çulha, “Synthesis of boron nitride nanotubes and their applications,” *Beilstein J. Nanotechnol.*, vol. 6, no. 1, pp. 84–102, 2015.

[73] X. Chen and C. Ke, “Structural and physical properties of boron nitride nanotubes and their applications in nanocomposites,” in *Boron Nitride Nanotubes in Nanomedicine*, William Andrew Publishing, 2016, pp. 183–199.

[74] X. Chen, C. M. Dmuchowski, C. Park, C. C. Fay, and C. Ke, "Quantitative Characterization of Structural and Mechanical Properties of Boron Nitride Nanotubes in High Temperature Environments," *Sci. Rep.*, vol. 7, no. 1, pp. 1–9, 2017.

[75] S. I. Kundalwal and V. Choyal, "Enhancing the piezoelectric properties of boron nitride nanotubes through defect engineering," *Phys. E Low-Dimensional Syst. Nanostructures*, vol. 125, no. June 2020, p. 114304, 2021.

[76] O. H. Seeck and E. Bridget Murphy, "X-ray Diffraction: Modern Experimental Techniques," *CRC Press*, 2015.

[77] K. W. Andrews, D. J. Dyson, S. R. Keown, K. W. Andrews, D. J. Dyson, and S. R. Keown, "Calculation of interplanar spacings and angles. Interpretation of Electron Diffraction Patterns," *nterpretation Electron Diffr. Patterns*, pp. 72–72, 1967.

[78] A. Chauhan, "Powder XRD Technique and its Applications in Science and Technology," *J. Anal. Bioanal. Tech.*, vol. 5, no. 6, 2014.

[79] E. Hernández, C. Goze, P. Bernier, and A. Rubio, "Elastic Properties of C and BxCyNyComposite Nanotubes," *Phys. Rev. Lett.*, vol. 80, no. 20, pp. 4502–4505, 1998.

[80] K. N. Kudin, G. E. Scuseria, and B. I. Yakobson, "(formula presented) BN, and C nanoshell elasticity from ab initio computations," *Phys. Rev. B - Condens. Matter Mater. Phys.*, vol. 64, no. 23, pp. 1–10, 2001.

[81] A. P. Suryavanshi, M. F. Yu, J. Wen, C. Tang, and Y. Bando, "Elastic modulus and resonance behavior of boron nitride nanotubes," *Appl. Phys. Lett.*, vol. 84, no. 14, pp. 2527–2529, 2004.

[82] D. F. Jackson and D. J. Hawkes, "X-ray attenuation coefficients of elements and mixtures," *Phys. Rep.*, vol. 70, no. 3, pp. 169–233, 1981.

[83] W. H. McMaster, N. K. Del Grande, J. H. Mallett, and J. H. Hubbell, "Compilation of x-ray cross sections."

[84] R. J. Nemanich, S. A. Solin, and R. M. Martin, "Light scattering study of boron nitride microcrystals," *Phys. Rev. B*, vol. 23, no. 12, pp. 6348–6356, 1981.

[85] B. R. Rehani, P. B. Joshi, K. N. Lad, and A. Pratap, "Crystallite size estimation of elemental and composite silver nano-powders using XRD principles," *Indian J. Pure Appl. Phys.*, vol. 44, no. 2, pp. 157–161, 2006.